ALMA MATER STUDIORUM
UNIVERSITÀ DI BOLOGNA

DOTTORATO DI RICERCA IN

Ingegneria Biomedica, Elettrica e dei Sistemi

Ciclo 37°

Settore Concorsuale:09/E2 - INGEGNERIA DELL'ENERGIA ELETTRICA

Settore Scientifico Disciplinare: IIND08/B

SPACE CHARGE BEHAVIOUR IN QUANTUM DOT/EPOXY RESIN NANOCOMPOSITES FOR HVDC APPLICATIONS

Presentata da: Daniele Mariani

Coordinatore Dottorato

Michele Monaci

Supervisore

Davide Fabiani

Co-supervisori

Simone Vincenzo Suraci
Paolo Seri

Esame finale anno 2025

Ho avvertito l'ingenuo sospetto del dottorando che sotto la congenita complessità delle faccende umane scorra una formula così semplice ed elegante che la redenzione dipendeva dal suo svelamento. Una volta sollevato il velo e sbirciato il disegno sottostante, non avrebbe più rinunciato al suo tentativo di recupero. Il desiderio superava quello di cibo, di favole della buonanotte, valeva la pena inseguirlo con lo zelo del neofita, con la semplicità di un monaco, di un vero habitué: l'assillo di un significato nascosto

---

Canone del desiderio, Richard Powers

Contents

Abstract

This work investigates the feasibility of semiconductive nanostructures, namely Quantum Dots (QDs), as additives in polymeric matrices to improve dielectric properties. The primary aim is to explore how QD incorporation influences space charge behavior in an epoxy resin, DER332.

The research begins with an overview of high voltage direct current (HVDC) systems and the increasing relevance of nanodielectric materials in advanced insulation technology. Given the inherent properties of QDs, particularly their ability to create discrete energy states within materials, their role as additives in altering dielectric performance is of notable interest. This study aims to bridge the gap between the fundamental theoretical properties of QDs and their practical application within polymeric insulation materials.

Two nanocomposites were fabricated with QD loadings of 0.04% and 0.1%, respectively. A comprehensive experimental campaign, comprising both chemical and electrical measurements, was conducted to assess the effectiveness of QD incorporation into the epoxy matrix. Characterization efforts were focused on analyzing space charge distribution, charge trapping behavior, and the electric field profile within the QD-enhanced samples, also focusing on the conductive and dielectric properties of the analyzed materials. Three main findings emerged from the study:

- Firstly, the addition of Carbon Quantum Dots creates charge carrier traps within the matrix, leading to modifications in space charge behavior and altering the electric field distribution
- Second, a novel method to evaluate space charge dynamics was preliminarily validated through short-term current transient analysis, providing a new potential approach for studying dielectric materials
- Finally the results suggest that QDs can potentially enhance the field grading capabilities of epoxy resins.

In conclusion, the significant impact on the dielectric properties of epoxy resin due to the incorporation of a minimal amount of Carbon Quantum Dots requires further investigation, as it has the potential to contribute to the development of innovative materials in the field of insulation engineering.

Chapter 1

HV technology

1.1 HVAC and HVDC technologies

In high-voltage transmission, two primary technologies are available: High Voltage Alternating Current (HVAC) and High Voltage Direct Current (HVDC). HVAC transmission is well-established due to extremely efficient voltage conversion using transformers, which can step up the voltage for transmission and step it down for local distribution. HVAC systems are widely deployed due to compatibility with the existing infrastructure and straightforward integration into local and regional grids.

HVDC is emerging as a compelling alternative for specific applications. For example, one significant drawback of HVAC transmission over long distances is the need to inject reactive power into the network to maintain voltage levels. Reactive power compensation becomes increasingly necessary as line length increases, leading to higher current in the conductors and, consequently, larger conductor sizes. This requirement not only raises material costs but also limits the Total Transfer Capability (TTC) of long HVAC lines.

HVDC transmission avoids reactive power issues entirely, as direct current has no reactive component. As a result, HVDC lines experience lower losses over long distances compared to HVAC lines. This efficiency advantage becomes economically favorable at what is referred to as the break-even distance. For underground cables, the break-even distance is approximately 80 kilometers, whereas for overhead lines, it is around 600 kilometers. Beyond these distances, HVDC's reduced losses and smaller conductor requirements generally outweigh the high costs of the conversion infrastructure [1].

HVDC is particularly advantageous for submarine power cables, such as those used in intercontinental links or offshore wind farm connections, where HVAC transmission would suffer high capacitance and charging current losses. HVDC's lack of reactive power requirements allows for significantly longer and more efficient underwater transmission without the same extent of voltage degradation experienced in AC cables. As such, HVDC is the preferred choice for submarine applications, as demonstrated by major HVDC submarine interconnections like those linking the UK and mainland Europe.

Another advantage of HVDC is that while HVAC systems require synchronous operation to

transfer power effectively, HVDC links can bridge grids operating at different frequencies or with asynchronous timing. This capability supports greater grid flexibility, enabling power exchanges between regions without necessitating synchronization, which is essential for linking grids with differing operational standards.

HVDC systems require converter stations at both the sending and receiving ends. While these converters are costly, they offer substantial benefits in long-distance transmission, where they can operate at higher efficiency and reduce certain losses inherent to AC systems.

In HVAC systems, proximity and skin effects contribute to additional power losses beyond typical resistive (Joule) losses. In high-frequency AC, current tends to concentrate near the conductor surface (skin effect), effectively reducing the conductor's cross-sectional area and increasing resistance. Additionally, proximity effects cause non-uniform current distribution in conductors placed close to each other, leading to further inefficiencies. HVDC transmission, however, avoids these issues because DC current flows uniformly across the conductor's entire cross-section, minimizing resistive losses and reducing heating effects.

1.1.1 LCC and VSC

HVDC transmission has evolved into two primary converter technologies: Line-Commutated Converter (LCC) and Voltage Source Converter (VSC) systems. Each has distinct characteristics, making them suitable for different applications within the power transmission landscape [2, 3]. LCC HVDC, also known as classic HVDC due to its previous implementation, uses thyristors to convert AC into DC and vice versa. This technology requires a strong connection with the AC grid to function properly since it relies on the grid's AC voltage waveform for commutation . The reliance on a strong AC system implies that LCC HVDC systems are best suited for stable, large-scale power transmission where strong, interconnected AC grids are available. LCC HVDC technology is known for its high reliability and is considered a cost-effective solution for long-distance, high-power transmission. Since it has been in use for several decades, LCC technology is consolidated, benefiting from extensive operational experience. In terms of power control, LCC systems operate with fixed current flow; to reverse power flow, the DC voltage polarity must be switched. While this polarity reversal can introduce some complexity, it is effective for the bulk transmission of power over long distances. VSC HVDC represents a more innovative approach in HVDC technology. Unlike LCC, VSC systems use Insulated Gate Bipolar Transistors (IGBTs), which enable more flexible and precise control over power flow. One of the standout features of VSC technology is its black start capability, meaning it can initiate power flow without relying on an existing AC grid. This feature is particularly valuable for applications in remote areas or offshore wind farms, where a stable AC grid might not be immediately accessible. Additionally, VSC HVDC offers excellent reactive power control, which can actively contribute to voltage stability in the connected AC grid. Unlike LCC, VSC technology does not require polarity reversal to change the direction of power flow, avoiding insulation issues related to space charge phenomena. However, VSC systems generally have lower voltage and power handling capabilities compared to LCC, making them less suited for extremely long distance transmission. Despite these limitations, VSC technology is advancing quickly, with

ongoing developments in component technology and control strategies that continue to expand its capabilities. Hybrid converters are also available, which manage to deploy the benefits arising from both technologies; an example is Skagerrak HVDC project, where multiple HVDC links with the two different technologies are available [4]. These technologies may be also characterized by different electrode configurations: a monopolar one, which abates costs, but requires an electrode return and is hampered by lower reliability, or a bipolar one, exhibiting better system availability due to its redundancy.

1.1.2 Structure of a HV cable

HVDC cables are complex, multi-layered systems, whose structure is presented in this section. At the core of each cable is the inner conductor, which performs the critical function of electrical energy transportation. Surrounding this conductor is a semiconductive sheath, which ensures a stable interface between the metal conductor and the insulating layers, reducing stress concentrations at these junctions and providing better compatibility between different material surfaces. The insulating system, a crucial component, can be realized in various forms depending on application requirements. Traditional HVDC cables often employ a paper-oil insulation, known as MIND (Mass-Impregnated Non-Draining) insulation, which combines layers of paper impregnated with a special oil to maintain dielectric strength over long operational periods. An alternative to MIND is the use of extruded polymer insulators, primarily made from cross-linked polyethylene (XLPE) or polypropylene (PP). These extruded polymers offer several advantages, such as reduced costs, simplified production processes, and less environmental impact compared to MIND cables, which can risk oil leakage. Recently, a more advanced MIND option incorporating Polypropylene Paper Laminated (PPL) insulation has emerged, promising enhanced thermal stability and electrical performance under HVDC conditions. Although extruded polymer cables are highly efficient and increasingly popular, early HVDC installations faced challenges with these materials due to reduced lifespans compared to similar HVAC cables at equivalent voltage levels. This reduced lifespan in HVDC applications is attributed to the phenomenon of space charge accumulation, where charge carriers become trapped within the insulating material, leading to localized electric field distortions and accelerating aging processes. Beyond the insulation layers, another semiconductive sheath further supports field uniformity. To achieve higher lifetimes, particularly in the demanding environment of undersea installations, HVDC cables may include additional structural reinforcements. These often consist of a layer designed to provide mechanical support for the cable internal layers, along with an external jacket layer that protects against potential hazards, including physical impacts, abrasion, and marine life interactions, thereby extending the cable's operational reliability in harsh underwater conditions.

1.1.3 Power quality improvement instrumentation and surge arresters

Other components of HVDC systems have two fundamental aims: power quality and system protection. The former is achieved by DC and AC filters and smoothing reactors, the latter by surge arresters and protective relays, which will be treated in a following section on circuit breakers.

Starting with the filters, their primary role is to mitigate harmonic currents generated during the conversion process in HVDC systems [5, 6]. These harmonics can affect the DC transmission lines, potentially causing disturbances in nearby communication systems and impacting the overall system performance. By filtering out unwanted harmonics, DC filters help reduce the stress on components on the DC side, which can prolong their operational lifespan, as excessive harmonics can lead to overheating and premature failure of equipment such as capacitors and converters. DC filters can also contribute to maintaining control stability within the HVDC system, as they can dampen resonances that may arise due to interactions between the converter and the transmission line, thereby enhancing the reliability and stability of the power transmission. Moreover, HVDC converters typically consume a substantial amount of reactive power, which can be mitigated by shunt-connected AC filters that act as capacitive sources at the fundamental frequency. Filters can also play a role in suppressing overvoltages that might occur during transient conditions, protecting sensitive equipment from voltage spikes that could damage components. As far as smoothing reactors are concerned, they considerably increase the efficiency and the reliability of the system. They act as stabilizers of current and voltage intensities; in particular, they significantly reduce the ripple in the DC current due to their inductive nature. They can also absorb impulsive currents, which could lead to significant voltage spikes due to capacitive nature of the insulating components, thus carrying out a partial protection for the electrical system. However, when higher intensity overvoltages occur, e.g. due to lightning strikes, protection is mainly performed by surge arresters [7]. These are nonlinear resistances, normally fabricated in silicon carbide (SiC) or metal oxide. In case of SiC the technology involves also several spark gaps, which render this technology likely to be replaced by metal oxide in recent future. Even though they have an extremely low fault rate (less than 0.01% every year), condition monitoring is fundamental, as negligence of maintenance leads to 26% of faults.

1.2 Use of epoxy resin in modern HV technology

1.2.1 Cable joints and terminations

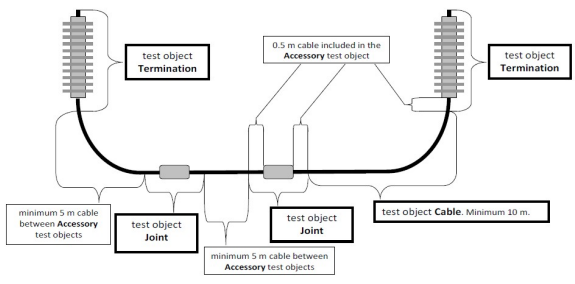

Figure 1.1: Section of a cable closed loop, after [8]

In Fig. 1.1, the complete structure of a high-voltage cable is shown, featuring two essential accessories: joints and terminations. Although epoxy resin is not the typical material used in manufacturing joints, its application is still considered in some cases [9]. Specifically, epoxy resin

finds its primary use in prefabricated composite joints, shown in Fig. 1.2, where it serves as the material for an insulation unit. This epoxy insulation unit is essential to electrically insulate the inner connector, which provides electrical continuity between the metallic conductors of the two connected cables.

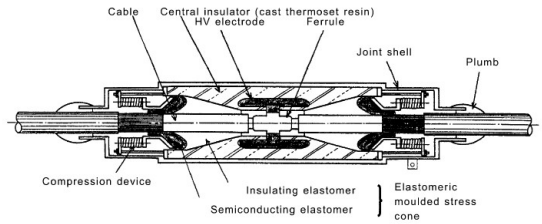

Figure 1.2: Prefabricated composite joint, after [9]

In these composite joints, the epoxy insulation unit comes into direct contact with both the high-voltage (HV) electrode and the premoulded stress cone, which is composed of elastomer rubber. This close contact between epoxy and other insulating materials can lead to specific challenges, particularly those related to space charge accumulation. One notable effect that may arise in this configuration is the Maxwell-Wagner-Sillars (MWS) polarization phenomenon, which can lead to interfacial space charge accumulation and may impact the dielectric performance of the joint over time. These issues with space charge accumulation are also relevant in transition joints, a particular type of joint used to connect different types of cable insulation, such as XLPE and oil-filled paper, in non-buried, above-ground installations. In such transition joints, epoxy resin is similarly employed, though its use is more common in alternating current (AC) applications, given the tendency for interfacial charges to redistribute more easily under AC conditions [9]. Nonetheless, these joints are also applied in high-voltage direct current (HVDC) configurations [10]. When used in HVDC systems, however, they are subjected to testing under AC voltage and partial discharge (PD) conditions to assess their chemical integrity (absence of voids), performance and reliability. Such tests are conducted in compliance with IEC standards 62067 and 60840, which outline the protocols for ensuring cable and accessory performance under operational stresses [11, 12]. Terminations in high-voltage systems consist of various individual components, including fiber-reinforced epoxy resin, which is often employed as a field-grading material due to its robust electrical and mechanical properties [13]. This material helps in managing and evenly distributing electric fields within the termination structure, thus reducing the likelihood of electric field concentrations that could lead to insulation breakdown.

In addition to HVDC cable systems, terminations are essential in other high-voltage installations, such as Gas-Insulated Switchgear (GIS). In GIS, terminations serve to effectively transition between the cable and GIS components, ensuring that the interface remains insulated and mechanically stable. For instance, epoxy resin is frequently utilized in separator cones between the external cable insulation and the GIS system, thereby providing both physical separation and enhanced insulation. This application of epoxy resin within GIS will be further elaborated upon in a subsequent section, focusing on the construction and function of GIS spacers [14]. Terminations in these systems are also susceptible to environmental factors, such as dust accumulation, particularly under non-

sinusoidal current conditions. Accumulated dust can degrade surface insulation and impact the overall performance of the termination, making regular maintenance a necessary practice. In some cases, additional protective coatings may be required to enhance durability and protect against contaminants. To monitor the internal condition of terminations, partial discharge (PD) measurements have also to be conducted. These measurements are critical in detecting voids, chemical degradation, or any early signs of insulation compromise within the epoxy or other materials used. Such assessments allow for the early detection of potential issues, ensuring the continued reliability and safety of the system over its operational lifespan.

1.2.2 Gas insulated switchgears and substations

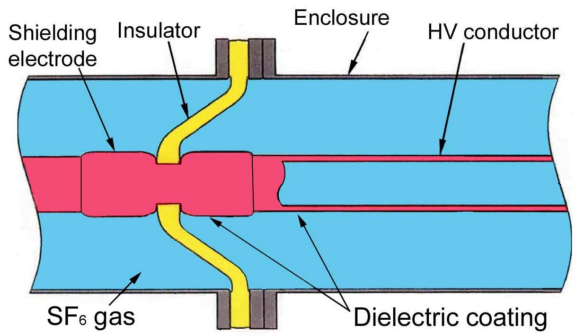

Figure 1.3: SF_6 spacer, after [15]

Gas-Insulated Systems (GIS) are essential components of modern high-voltage networks, widely used for their reliability, compactness, and robust insulation capabilities. At their core, GIS installations consist of a central conductor that carries the electrical current, surrounded by a metallic enclosure that acts as a grounded shield. Within this setup, the central conductor must remain electrically isolated from the grounded enclosure to prevent flashovers and potential short circuits [16]. The unique design of GIS enables compact, safe, and efficient operation, provided that the insulation components, particularly epoxy resins and sulfur hexafluoride (SF_6), are carefully selected and maintained.

Epoxy resins, often enhanced with fillers like aluminum oxide (Al_2O_3), play a critical role as both insulation and mechanical support. These resins form the basis of structural spacers within GIS, ensuring a secure separation between the conductor and the enclosure. By reinforcing epoxy with Al_2O_3, the dielectric and thermal properties are optimized, making these composites resilient under high voltage and variable temperature conditions. Such spacers provide a dual benefit: not only do they maintain mechanical stability in the presence of vibrations or thermal expansion, but they also act as highly reliable insulators, thus preserving the integrity of the dielectric barrier. Their function extends to providing thermal management, helping dissipate heat generated by the conductor, which can reach up to 105°C, whereas the enclosure generally remains around 60°C due to external cooling [17]. This thermal differential requires epoxy composites with high thermal conductivity to avoid dimensional changes that could compromise the GIS structure and insulation.

In addition to solid insulation, GIS systems also utilize SF_6 gas as the primary gaseous insulator.

SF_6 is renowned for its high dielectric strength and chemical stability, qualities that support compact GIS designs and contribute to the low maintenance demands of these installations. The gas exceptional insulation capabilities make it ideal for sustaining high voltage without requiring large air gaps, allowing GIS systems to achieve their compact form. However, the environmental impact of SF_6, particularly its high Global Warming Potential (GWP), has motivated the industry to explore alternative gases, such as C4-perfluoronitrile and C5-perfluoroketone [18], which offer lower GWP while preserving strong dielectric properties. These new gases are being developed to balance insulation performance with environmental sustainability, paving the way for more eco-friendly GIS options.

The gas-solid interface, particularly where the conductor, epoxy insulation, and SF_6 meet, presents unique challenges within GIS design. Known as the triple junction, this region experiences intense electric fields due to the meeting of conductive, insulating, and gaseous materials. Properly designed epoxy spacers help manage these field intensities, often utilizing rounded or contoured surfaces that distribute electric fields more uniformly. Such careful shaping reduces the risk of partial discharges and interfacial flashovers. Additionally, to further balance field stresses, grading rings are employed around critical points such as terminations and interface boundaries, which are susceptible to localized field concentration [19]. These rings effectively smooth the electric field along component surfaces, enhancing the stability of the insulation and reducing the risk of partial discharge. Accurate modelling during the design phase is essential to ensure optimal grading ring placement and shape, as even minor deviations can affect field distribution, potentially compromising insulation reliability.

One of the notable considerations in GIS is metal particle contamination. During assembly or due to operational wear, metallic particles may find their way into the GIS environment. Under the influence of strong electric fields, these particles become mobile, particularly in high-stress regions near the gas-solid interface, posing a risk of localized field enhancement and partial discharges. Particle traps are incorporated to mitigate this risk, capturing mobile contaminants and maintaining a stable dielectric environment [20]. These traps are strategically positioned within the enclosure to prevent particles from migrating to critical areas, thus helping to preserve the system's reliability over extended periods.

For HVDC applications, GIS faces even greater challenges, particularly due to space charge and the need to prevent long-term dielectric degradation. Unlike AC systems, where periodic current reversal helps relax electric fields, HVDC GIS installations experience static electric fields, which can lead to gradual space charge buildup and uneven field distributions over time. This accumulation can alter the anticipated electric field patterns within the system, making meticulous spacer and grading ring design crucial to reducing the risk of insulation failure. Although prototypes of HVDC Gas-Insulated Lines (GIL) exist, the technology has not yet reached full commercial viability due to these complex operational challenges.

Environmental exposure introduces further considerations for GIS systems, particularly in outdoor installations where external contaminants and atmospheric conditions can impact SF_6 and solid insulators alike. Dust accumulation and exposure to humidity may degrade the SF_6 and epoxy spacers, reducing dielectric performance. In these scenarios, protective coatings and regular maintenance

become essential to ensure consistent insulation properties. Additionally, GIS systems benefit from periodic partial discharge (PD) testing to detect early signs of insulation breakdown, such as voids or material degradation, which could indicate an impending dielectric failure. PD measurements provide a non-destructive way to monitor GIS health, allowing operators to maintain system reliability and plan for proactive maintenance where needed.

1.2.3 Bushings

Bushings are essential components in high-voltage systems, designed to safely pass high-voltage conductors through openings in grounded planes, thereby enabling the conductor to connect to devices such as transformers and switchgear without compromising electrical insulation (see Fig. 1.4). The fundamental purpose of bushings is to maintain electrical continuity while providing effective insulation to withstand the full rated voltage, thus preventing electrical breakdown and maintaining system integrity. Proper bushing design must carefully account for the dielectric stress imposed by high-voltage operation, along with the thermal and mechanical stresses inherent in their operating environment. The selection of insulation materials and the specific configuration of the bushing are, therefore, critical factors in ensuring both performance reliability and longevity.

Three primary materials are traditionally used in bushing insulation and all utilize paper impregnated with an insulating fluid to enhance dielectric properties. These configurations include resin-bonded paper (RBP), resin-impregnated paper (RIP), and oil-impregnated paper (OIP). Among these, RBP, once widely used, is now largely considered an outdated technology due to advancements in other bushing designs that provide superior performance and reliability. RBP bushings are predominantly utilized only in specific cases where older bushings require direct replacement with the same type to maintain compatibility with legacy systems. In contrast, RIP and OIP are the preferred configurations for modern bushing applications. Each offers unique properties suited to various operational requirements.

In OIP bushings, paper is impregnated with mineral oil, which provides excellent dielectric strength and cooling capabilities. However, OIP bushings also present potential challenges related to the flammability of mineral oil and environmental concerns, which can complicate maintenance and operational safety. RIP bushings, on the other hand, employ epoxy resin to impregnate the paper insulation, creating a rigid and highly durable insulation structure that is less prone to oil leakage and associated maintenance issues. Additionally, RIP bushings are known for their greater resistance to environmental conditions, including moisture contamination, making them advantageous for outdoor installations or applications where prolonged exposure to the elements is a concern.

They represent a substantial portion of the overall failure rate within high-voltage equipment due to their exposure to persistent electrical, thermal, and mechanical stresses. These stresses result from the continuous passage of high voltage, which subjects the insulation material to significant dielectric stress, as well as the thermal cycling that occurs during regular operation. Mechanical stress is also a concern, as bushings must remain structurally stable despite any vibrations or mechanical forces exerted by connected equipment. Consequently, bushing failures are critical events with potentially widespread consequences, as they can lead to insulation breakdown, faults, or even catastrophic

equipment failure. Due to this vulnerability, bushings are often a focal point in condition-based maintenance diagnostics, where operators monitor their performance and insulation integrity to identify early signs of deterioration. Diagnostic techniques, which may include partial discharge measurements, thermography, and dissolved gas analysis (in OIP configurations), provide essential data to predict bushing performance and address potential failures.

When epoxy resins are used in RIP bushing designs, specific operational constraints are crucial to maintaining the integrity of the insulation system. One of the critical parameters for epoxy-based RIP bushings is the glass transition temperature (T_g), which is typically around 398 K (125°C).

In addition to thermal limitations, RIP bushings containing epoxy resin are also susceptible to electrical discharge events, particularly when an electrical arc or other high-energy discharge occurs. In such instances, a localized temperature spike can induce rapid chemical changes within the epoxy, leading to the formation of deep traps within the material. These deep traps capture free charge carriers and promote the accumulation of surface charge, which creates a feedback loop that exacerbates local electric field intensities. As surface charge increases, so does the likelihood of partial discharges, which further deteriorate the insulation. This feedback mechanism underlines the critical importance of maintaining operational parameters that avoid discharge events and excessive heating in RIP bushings to ensure consistent insulation performance and prevent premature failure [21]. Traditional bushings are for HVAC applications, particularly in high voltage transformers. For rated voltages higher than 60 kV, they are manufactured with a geometry achieving capacitive field levelling performed by employing intermediate electrodes between the high voltage and the ground. This leads to a broadening of the field lines, thus to a lower magnitude of both the radial and the tangential electric field. In fact, the former could induce the total discharge in the sample, while the latter to a surface discharge. As the former requires is an extreme occurance, which requires significantly higher electrical stresses, the greatest care is taken in the reduction of the tangential electric field. In the classical configuration, two main tests are to be performed periodically to assess the bushing overall performance, namely the measurement of the capacitance between the central conductor and the last electrode of the configuration, and the measurement of the capacitance and of the tanδ between the last electrode and the flange.

1.2.3.1 DC bushings

According to the IEC 65700 standard, an HVDC bushing is defined as a "bushing subject to DC voltage stress, which includes bushings used on the valve winding side of a converter transformer, DC smoothing reactor bushings, wall bushings, and those used in converter valves" [22]. The specific requirements of DC bushings distinguish them from AC bushings, as they must endure prolonged, stable voltage stress and are therefore subject to unique design and material challenges. With the advancement of ultra-high voltage direct current (UHVDC) technology, especially in regions like China where new infrastructure projects continue to push the voltage limits, DC bushing technologies have been a focus of rapid innovation and development [23].

HVDC bushings, particularly those designed for UHVDC applications, face specific challenges that must be addressed to ensure safety, performance, and reliability under extreme operating

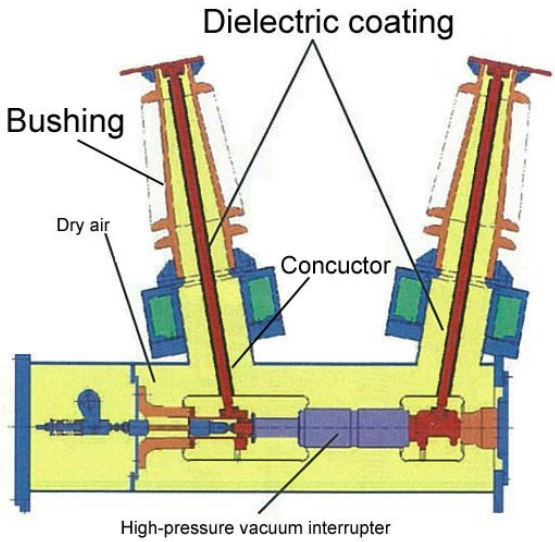

Figure 1.4: Bushings, after [15]

conditions. Testing HVDC bushings, as detailed in studies such as [24], is particularly challenging due to the exceptionally high voltages involved. Unlike AC systems, DC voltages introduce particular stress factors, including issues related to long-term insulation stability and the steady-state stress that affects material properties. Practical difficulties during HVDC testing can stem from a variety of factors, beginning with the physical setup and mechanical installation of the measurement equipment. Additionally, external environmental factors such as wildlife interference, contaminants on the bushing surface, and humidity can significantly influence test results, potentially distorting partial discharge (PD) measurement data.

A major area of focus in HVDC bushing design are the converter transformer valve-side bushing and the wall bushing. These specific types are subject to a unique set of combined AC and DC stresses, resulting from the converter operations, which introduce complex electrical field interactions that differ significantly from those in standard AC or DC bushing applications. The simultaneous exposure to high AC and DC electrical fields is a substantial factor influencing the lifespan of HVDC bushings, as these combined stresses can accelerate material degradation. As a result, the design and material selection for these bushings must account for this multi-stress environment, often necessitating the use of advanced insulating materials that are both electrically and mechanically robust.

Beyond electrical stresses, additional considerations in HVDC bushing design include mechanical pressure [25] and thermal management. High operating pressures can impose structural demands on the insulating materials, which must remain dimensionally stable and resistant to cracking under compressive and tensile stresses. Furthermore, thermal dynamics play a critical role, as the continuous operation at high voltage generates heat that must be efficiently managed to avoid thermal breakdown of the insulation. Moreover, overtemperatures can lead to anomalous electric field and space charge distributions, which can significantly distort the electrical behaviour of the bushing, leading to likely reduction of the performances and premature failure [26].

1.3 Impact of properties on lifetime

1.3.1 Effects of combined AC and DC voltages

In HVDC systems, critical components such as the converter transformer valve-side bushing frequently encounter simultaneous AC and DC voltage stresses. This combined-stress environment presents a uniquely challenging operational condition, where the coexistence of AC and DC voltages places complex demands on the durability and reliability of the involved components [27]. Unlike pure AC or DC stresses, the interaction between these voltages induces specific aging mechanisms in HVDC insulation, which must be accounted for in both design and material selection. In particular, the AC component tends to activate partial discharge (PD) activity within any microvoids or imperfections that may exist in the insulation, a phenomenon that can gradually lead to localized erosion, mechanical weakening, and chemical degradation of the material. Over time, this PD activity accelerates material degradation and reduces insulation efficacy.

On the other hand, DC stress is known to prompt space charge accumulation within the insulation material. The synergy between PD induced by AC stress and space charge buildup due to DC stress amplifies the likelihood of insulation breakdown, forming a feedback loop that intensifies stress on the material and leads to accelerated aging. This process ultimately reduces the operational lifespan of HVDC components, demanding highly resistant materials and precise engineering to delay such breakdown phenomena.

An additional critical consideration in HVDC insulation performance is its ability to withstand both steady-state DC breakdown and transient voltage conditions, both of which are prevalent in HVDC applications. During steady-state operation, a continuous DC voltage is applied, creating a stable electric field that must be reliably sustained over long operational periods without significant degradation in insulation performance. However, HVDC systems are also subject to transient stresses, such as those introduced by impulse voltages during switching operations, lightning strikes, or system faults. These impulse voltages produce sudden, intense electric fields that challenge the insulation's capacity to resist momentary high-stress events without compromising its long-term integrity. The short-duration but high-intensity stresses caused by impulse events create localized heating and stress concentrations, which, if not effectively managed through design and material engineering, can lead to thermal and mechanical deterioration of the insulation material. Over time, repeated exposure to such stresses increases the risk of insulation failure, potentially leading to catastrophic outcomes if adequate preventive measures are not incorporated.

Despite limited literature focused on HVDC insulation materials beyond standard cable insulators like XLPE, studies have highlighted the accelerated degradation effects that arise when AC and DC stresses are combined. Notably, superimposed AC and DC fields have been shown to enhance mechanisms such as electrical treeing, which is a key pathway to insulation breakdown [28]. Electrical treeing involves the formation of microscopic channels within the insulation due to high-stress fields, which over time grow and connect, compromising the material's ability to act as an insulator. For instance, research shows that the time to breakdown can decrease by around 38% when a 5 kV/mm DC field is superimposed on a 4 kV/mm AC field applied to epoxy resin, highlighting the substantially

accelerated wear rate under combined-stress conditions. This accelerated degradation underscores the need for resilient material designs, as even incremental increases in stress can dramatically affect insulation lifespan.

Furthermore, experimental studies have demonstrated that even in nanocomposite materials, which are generally designed for enhanced durability, combined AC and DC stress can lower breakdown strength. In scenarios where DC stress at higher frequencies is superimposed on a lower-intensity AC field, the breakdown strength in materials such as TiO_2 nanocomposites is reduced significantly. Although they exhibit marked improvements in breakdown resistance compared to neat materials, this combined-stress condition underscores that even advanced nanocomposites are susceptible to accelerated aging under dual-stress conditions [29].

1.3.2 Space charge

Space charge accumulation is a significant phenomenon affecting the performance and reliability of HVDC insulation systems, especially in polymer-based materials. In an HVDC environment, space charge refers to the accumulation of surplus electric charges within the dielectric material, which can originate from various sources, such as charge injection from electrodes, impurity-driven traps, and field-dependent ionization. Unlike AC systems, where electric fields oscillate, HVDC systems apply a constant electric field, allowing charges to accumulate and reach equilibrium over time. This section discusses the mechanisms of space charge formation, its effects on electric field distortion, and its implications under typical HVDC operating conditions, including polarity reversal. Space charge formation in polymeric materials, involves a complex interaction between transport mechanisms and trapping phenomena within the dielectric. When a polymer is in contact with a conductive electrode, charge carriers, typically electrons or ions, can be injected into the polymer. The properties of the polymer itself, such as its chemical structure and purity, strongly influence the transport of these charges across the material. Charge mobility in polymeric insulators is limited, as the carriers encounter various trapping sites, including impurities, voids, and defects that are part of the polymer's chemical structure. In an ideal dielectric, charges would distribute uniformly under an electric field, but in HVDC systems, they tend to accumulate near interfaces or within microstructural imperfections, leading to localized space charge regions [30]. Other key features are trap volumetric density and depth. The latter is the amount of energy required in order to release a carrier from a trap. It can go from very low values such as lower than 0.4 eV, typical of physical traps arousing, for example, from the borders between amorphous and crystalline regions, to values higher than 0.8 eV, usually related to chemical bonds or functional groups that tend to retain charge carriers, even though also interfaces between different phases arising e.g. in nanocomposites can reach these high values [31, 32]. One of the primary impacts of space charge on HVDC insulation is the distortion of the electric field. Ideally, an HVDC system would maintain a constant, uniform electric field (Laplacian field) across the dielectric. However, the presence of space charge creates non-uniformities, leading to local field enhancements or reductions. This distortion can exacerbate material stress, especially in regions where the electric field intensifies near imperfections or material interfaces.

A key factor that can dictate the electric field distribution of a material is the distinction between

homocharge and heterocharge. The former refers to charge accumulation within the polymer that has the same polarity as the electrode. For example, if a positive voltage is applied, positive charges may be injected from the electrode into the polymeric material, creating a homocharge layer near it. Homocharge layers tend to reduce the local electric field near the electrode , as the field generated by the homocharge partially opposes the applied electric field. This reduction in field stress near the electrode interface can decrease the risk of field-related insulation degradation at the electrode-polymer boundary. However, excessive homocharge accumulation can distort the electric field within the insulation bulk, potentially causing uneven stress distribution. Heterocharge consists of charges that are of opposite polarity to the electrode. For instance, if a positive voltage is applied to an electrode, negative charges may migrate or become trapped near it, forming a heterocharge layer. Heterocharge layers increase the local electric field near the electrode. This increase in field intensity amplifies stress on the insulation material, particularly near the electrode-polymer interface, which can accelerate material agin and increase the risk of dielectric breakdown. The presence of heterocharge is especially critical in HVDC applications, where a constant high field may enable persistent accumulation, posing challenges under prolonged operation.

Polarity reversal is another critical consideration in HVDC systems. In HVDC power transmission, polarity reversal occurs when the direction of power flow changes, reversing the applied voltage polarity. Polarity reversal is especially challenging for polymeric insulation systems as the accumulated space charge from one polarity does not immediately dissipate or redistribute when the polarity switches. This leftover charge can amplify the newly applied electric field, leading to further field distortion and potential breakdown if the electric field exceeds the material's dielectric strength. This occurs also in case of previously injected homocharge, as due to change of polarity it now becomes heterocharge.

The impact of polarity reversal is a significant concern for materials with deeper trapping sites because trapped charges persist longer [33]. Polarity reversal can thus amplify field distortion effects and accelerate aging processes.

While most experimental and research studies have focused on XLPE and PP— the predominant insulation materials for HVDC cables—providing valuable insights into space charge behavior, including charge injection, transport, trapping, and its effects on electric field distribution, one of the main aims of this work is to further study and experimentally characterize space charge behavior in epoxy resins and their nanocomposites. This focus on epoxy is crucial given its widespread use in other HVDC components, as discussed in previous sections, even though it is not treated extensively in related literature, apart from some valuable exceptions [34].

1.3.3 Field grading

In high-voltage applications, where intense electric fields are generated near electrodes, various methods have been developed to redistribute the spatial distribution of field lines to mitigate the risk of excessive electric field intensities that could lead to material breakdown or other operational failures. Two primary field grading techniques are widely implemented, depending on the type of voltage application. For AC systems, particularly in components like AC bushings [35], capacitive

field grading is commonly employed, as in Fig. 1.5. This approach introduces multiple conductive layers within the insulating material to enable better control over the field line distribution, creating a smoother field gradient and reducing localized stress that could otherwise compromise component longevity. In contrast, DC systems primarily use resistive field grading, which involves materials that adjust their conductivity based on local field intensities, providing a dynamic method to mitigate electric field concentrations.

The effect of electric field intensity and temperature on the conductivity of polymeric insulating materials is substantial, presenting a challenge to the performance of HVDC system components. In extreme operational conditions, variations in electric field and temperature can lead to increased bulk and leakage currents, elevating the risk of flashovers and other damaging effects. To counteract these risks, extensive research has been dedicated to enhancing the thermal and electrical stability of insulating materials. One effective solution is the incorporation of fillers, which improves the thermal resilience of the insulating material and allows it to dynamically adjust its conductivity in response to localized electric fields. This adjustment effectively distributes the field more evenly, reducing the potential for highly stressed points that may lead to premature failure in high-voltage equipment. The steady-state conductivity of these materials, however, exhibits a highly nonlinear relationship with applied electrical and thermal stress, often described through complex conductivity models.

An innovative development in this field is the creation of nonlinear field grading materials that incorporate specific additives to establish a strong nonlinear dependence of permittivity and conductivity on electric field and temperature. These materials are generally composites of polymers like epoxy or silicon rubber, doped with materials such as zinc oxide (ZnO) or silicon carbide (SiC), which introduce a field-dependent conductivity characteristic essential for efficient field grading [36]. In practical applications, these materials demonstrate significant benefits, as they have been shown to lower maximum electric field intensities and increase discharge inception voltages when applied to components with complex geometries, such as funnel-shaped epoxy spacers used in Gas Insulated Substations (GIS). These benefits have been especially evident in studies on epoxy spacers, where field grading additives contribute to a more uniform field distribution and an increased threshold for electrical discharge, enhancing overall component resilience under operational stress [37].

Despite these advantages, long-term studies on field grading materials have revealed some critical challenges. Specifically, prolonged exposure to high electric fields can intensify the power dissipation factor of the material, indicating an increase in energy loss and a potential degradation of performance over time. For example, in accelerated aging tests lasting up to 1080 hours, which approximate the effective lifetime of GIS components, a significant rise in the power dissipation factor was observed, suggesting a limitation in the long-term stability of field grading materials under extended operational conditions [38]. Notably, discrepancies in performance outcomes, such as those observed in different studies, may be attributed to variations in additive concentrations and filler size within the polymer matrix. Higher additive concentrations, for example, tend to exhibit more pronounced degradation effects over time. Moreover, the particle size of fillers, typically micrometric in these studies, also plays a crucial role in determining the material's long-term performance, with smaller particles generally offering better dispersion and field grading capabilities.

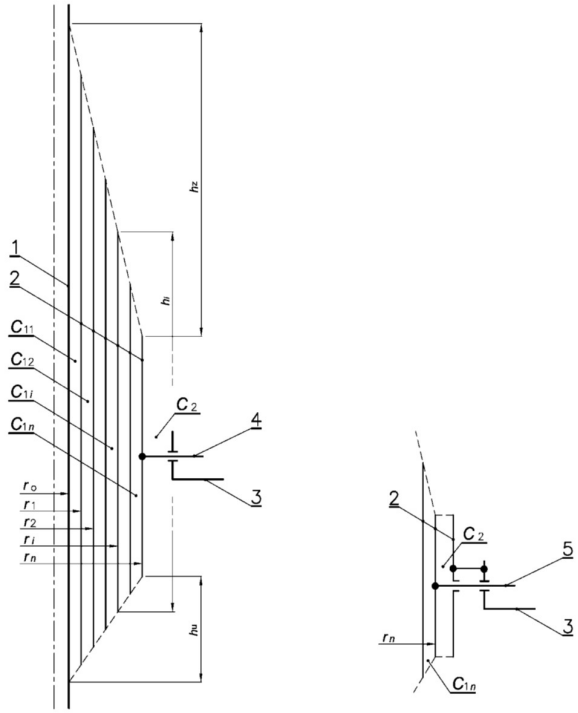

Figure 1.5: Capacitive field grading, as in [35]

1.4 Main aims of this work

The purpose of this work is an extensive characterization of epoxy resin composites additivated with semiconductive nanofillers. This study aims to comprehensively investigate how these nanofillers influence the material's space charge and conductive properties by means of PEA, TSDC and DC conductivity tests, with a particular focus on determining their practical applicability in HVDC insulation systems. Epoxy resins, commonly used in high-voltage applications, are prone to certain limitations in dielectric strength and thermal stability, which can hinder their effectiveness in prolonged high-stress environments. Adding semiconductive nanofillers might mitigate some of these limitations through mechanisms like the Quantum Confinement Effect, exposed in Section 2.2.2, according to which charge carrier traps may be introduced, thereby influencing space charge dynamics in these composites. These measurements are complemented by thermal and spectroscopy techniques, such as DSC, TGA and FTIR, in order to assess whether structural modifications occurred in the morphology of the materials, and to link this change in the chemical framework to the variations in the intrinsic properties of the materials.

A primary goal of this research is the experimental validation that these nanofillers, through Quantum Confinement, effectively act as traps for charge carriers within the epoxy matrix. The introduction of traps could influence charge accumulation and dissipation rates, potentially modulating the space charge characteristics of the composite. Establishing this correlation would provide insight into the fundamental interactions between the nanofillers and the polymer matrix, supporting

theoretical assumptions with empirical data. Furthermore, by characterizing space charge properties, the study aims to elucidate how charge distribution varies across different compositions and whether the trap characteristics introduced by the nanofillers can be controlled or tuned to optimize dielectric properties.

In addition to space charge properties, this thesis seeks to explore the conductivity of these composites under varying temperatures and electric fields. Since HVDC applications involve prolonged exposure to high electric fields and elevated temperatures, it is essential to understand how these conditions influence the conductivity of nanofiller-doped epoxy composites. This research will, therefore, investigate the temperature dependence of electrical conductivity and the material's behavior under electric field stress. By exploring these parameters, the study aims to assess the stability and robustness of the composite material, determining if it can sustain HVDC applications over extended periods without degradation, and the potential field of application.

Chapter 2

Nanocomposite properties and fabrication methods

2.1 State of the art of nanocomposites in electrical engineering

Nanocomposites can be used in several applications concerning electrical engineering [39]. One of the most prominent are those who use dielectrics as base materials, also called nanodielectrics. This application of nanotechnologies involves a significant modification of the properties, as the chemical structure of the composite is strongly different from the neat material. In particular, the interface between the matrix and the filler is the key part, yielding different characteristics from the neat material. Moreover, the dimension of the incorporated particles is in the order of nanometers, thus improving the surface-volume ratio as opposed to microcomposites, and thus both reducing the amount of additives which has to be used and obtaining a more significant impact on the resulting blend. Consequently, this feature of imparting a new specific property to the matrix contributes to the achievement of multifunctional materials. In the following subsections, both nanodielectrics and other nanocomposites are treated, putting more emphasis on the former ones.

2.1.1 Additivation methods

2.1.1.1 In Situ polymerization

In Situ polymerization, whose schematic process is reported in Fig. 2.1, is a simple process that involves the incorporation of additives in a matrix. This method had a great success with clays filled into polymeric hosting materials. The pioneering work was the one performed by Toyota in 1993 [40]. It is a universal method, which can thus be used both for thermoplastic and thermoset polymers. The initial results for caprolactam were confirmed for a wide gamut of thermoplastics, ranging from classical polyolefins to other materials such as PolyEthyleneTerephtalate (PET), PolyMethylMethAcrylate (PMMA) and Polystyrene (PS). Nevertheless, this method is extremely time consuming in its initial phases, and as a consequence other methods are preferred in the development of thermoplastic materials (the ones described in the following chapters). It is still used for thermoset materials as this

method is the unique one which can be used for this kind of hosting matrix. A typical step-by-step process of this method for application with an epoxy matrix can be enumerated as follows: the epoxy prepolymer and the filling material are vigorously mixed, e.g. by ultrasonication, in order to achieve a good dispersion of the additive particles inside the epoxy; another mixing is performed between the resulting mixture and the hardener of the matrix. This allows the reticulating process to begin. Before the compounding results too viscous, it is cast onto a mould in order to undergo the curing process, which usually takes place in an oven to provide the thermal energy required. In the initial steps, a shear mechanical stress can help achieve a better dispersion, thus obtaining exfoliated rather than intercalated or flocculated nanocomposites.

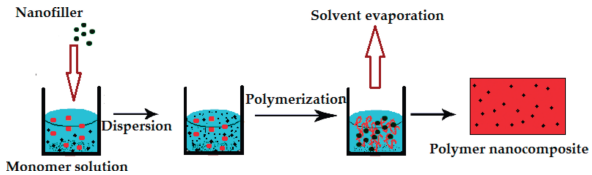

Figure 2.1: In situ polymerization, after [41]

2.1.1.2 Solvent blending

Solvent blending is a common technique in the fabrication of nanocomposites, particularly suited for thermoplastics that are soluble in nonpolar solvents. This method is advantageous because it enables a fine dispersion of nanoparticles within a polymer matrix, which is crucial for enhancing the material properties of the resulting composite. As illustrated in Fig. 2.2, solvent blending begins by dissolving both the filler particles and the polymer (or prepolymer) in separate solutions, using a solvent that is compatible with both components. This compatibility is a critical factor, as it ensures that the solvent can adequately interact with both the polymer chains and the nanofillers, promoting uniform distribution during the blending process.

Once both solutions are prepared, they are combined into a single mixture. At this stage, mechanical, thermal or acoustic agitation, such as stirring or ultrasonication, is applied to enhance the interaction between the polymer and the nanoadditives [42]. This agitation is key to breaking up any potential agglomerates of nanoparticles and encourages the polymer chains to interpenetrate and fully incorporate the filler particles. With effective mixing, the nanoparticles become well-dispersed throughout the polymer matrix, resulting in improved bonding at the molecular level.

After sufficient blending, the next step is to remove the solvent, typically through processes such as thermal evaporation or chemical precipitation. By carefully eliminating the solvent, a uniform nanocomposite structure is achieved, with the filler particles well intercalated within the polymer network.

However, despite its advantages, solvent blending also has some limitations. The requirement for nonpolar solvents, which can dissolve both the polymer and the fillers, presents challenges. These solvents are often both expensive and potentially hazardous, posing health and environmental risks. Additionally, careful handling and disposal of these solvents are essential to mitigate their impact, adding complexity to the process.

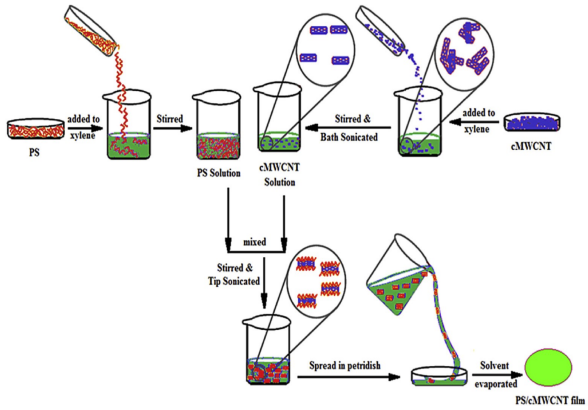

Figure 2.2: Solvent Blending, after [42]

2.1.1.3 Melt blending

The Melt Blending technique, applicable to thermoplastic materials, involves an extrusion process, as illustrated in Fig. 2.3. This method is particularly advantageous in commercial applications due to its cost-effectiveness, scalability, and adaptability to various polymer types [43]. During extrusion, the polymer is melted and combined with nanofillers under controlled conditions. However, to achieve optimal results, several critical processing parameters must be carefully managed, as they directly influence the quality of the nanocomposite [39], such as:

- Melt Temperature: Maintaining the correct melt temperature is essential to ensure proper mixing and flow properties of the thermoplastic polymer, as well as to avoid thermal degradation.
- Screw Design: The design of the screw used in the extruder, including its length, pitch, and configuration, affects the flow of the material within the extruder [44]
- Shear Stress: Shear forces generated within the extruder help to distribute and separate nanoparticles, but excessive shear may lead to particle breakage or degradation of the polymer matrix.

These parameters play a crucial role in achieving the two primary quality characteristics: dispersion and distribution. Dispersion refers to the degree to which nanoparticles are separated from each other, minimizing the formation of aggregates or clusters. Achieving uniform dispersion is essential to enhance the composite's performance, as clusters can lead to weak points in the material. Distribution, on the other hand, focuses on the even spread of nanoparticles throughout the entire polymer matrix, ensuring that the desired properties are consistent across the sample.

The challenge of maintaining effective dispersion is addressed by carefully selecting materials and controlling their cohesive properties, along with applying appropriate mechanical forces within the extruder. By focusing on elongational forces, which pull particles apart in different directions, the extruder can more effectively counteract the natural tendency of nanoparticles to cluster, enhancing the final properties of the nanocomposite.

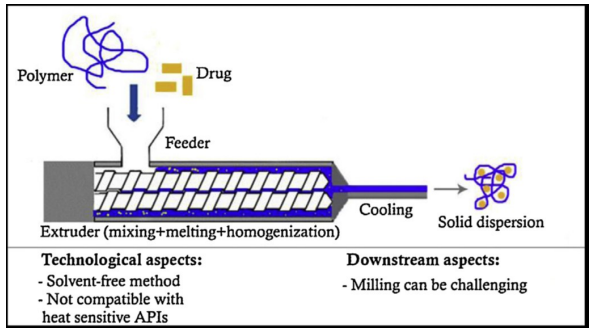

Figure 2.3: Melt blending process for nanocomposites, after [45]

2.1.1.4 Sol-gel methods

Sol-gel methods offer notable advantages in terms of environmental and safety impact, especially when compared to traditional techniques like solvent blending, which often involve the use of nonpolar solvents that can be toxic, flammable, and require special handling and disposal. Sol-gel processing, by contrast, is a versatile technique that typically operates at or near room temperature, reducing energy requirements and mitigating thermal risks associated with high-temperature processes. In the initial phase, a carefully selected precursor undergoes hydrolysis, as depicted in Fig. 2.4, a reaction that transforms it into an active form ready for further chemical processing. Following hydrolysis, the material progresses through a condensation phase, ultimately forming a stable, glass-like network.

One commonly used precursor in this process is a metal or silica alkoxide, which reacts to yield a metal hydroxide and an alcohol as byproducts. This stepwise reaction pathway not only minimizes the introduction of additional reagents but also allows for a controlled synthesis environment, enhancing the uniformity of the final material. Notably, by using alkoxides as precursors, it becomes possible to develop intricate three-dimensional networks within the material, opening avenues for fabricating nanofillers with enhanced dispersibility. These nanofillers can further be functionalized directly within the sol-gel matrix, tailoring their properties to specific applications such as improved adhesion, reactivity, or compatibility with other phases in the composite [46].

Compared to nanocomposites produced by methods like melt blending or solvent casting, sol-gel-derived materials generally contain fewer impurities. This heightened purity results from the controlled synthesis environment and the limited need for solvents or additional reagents, leading to fewer residual contaminants in the final product.

2.1.2 Clays

The employment of clays, is widely present in literature. This is due to their economic feasibility and to their ability of creating exfoliated and well-dispersed nanocomposites. This is particularly true for those clays characterised by higher Cationic Exchange Capability (CEC), such as montmorillonite, saponite and hectorite. Several papers show that, while maintaining the same thermal properties, epoxy/clay nanocomposites showed a significant improvement in dielectric properties. These range from reduced space charge accumulation in PolyPropylene [48] to PD resistance in epoxy [49]

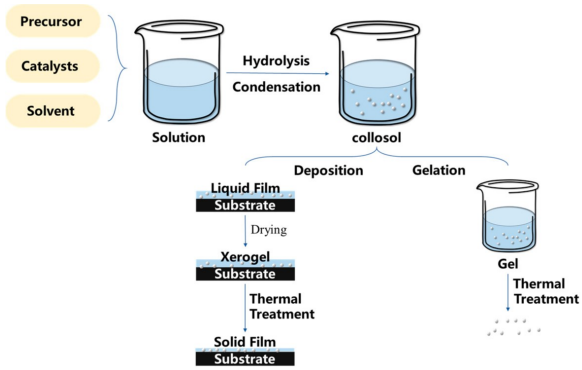

Figure 2.4: Sol-gel methods, from [47]

and electrical breakdown in XLPE [50]. In order to be soluble in water (e.g. for sol-gel method application), clays need to be functionalized; as a matter of fact, they are hydrophilic, thus requiring that a long molecule with both hydrophilic and organophilic extremities. The former is necessary to create a chemical bond with the clay, the other to have a better dissolution in polymers, which are usually hydrophobic (with the exception of PVA and PEO). Some examples of these molecules include: octadecilamine, alkylamonium and alkylphosphonium.

2.1.3 Inorganic oxides

Inorganic oxide additives are frequently incorporated into polyethylene matrices to tailor and improve various material properties, particularly for applications where enhanced electrical, mechanical, and thermal characteristics are required. These inorganic fillers have shown promising results in modifying the polymer's intrinsic properties, with specific oxides demonstrating significant improvements in terms of charge behavior, conductivity, and mechanical robustness.

A primary example is magnesium oxide (MgO), which has been investigated for its role in reducing the amount of space charge injected into polymer samples. A study demonstrated that MgO, when incorporated into polyethylene, effectively decreases space charge accumulation within the material, contrasting with the neat (unfilled) polymer, which displayed notable heterocharge at high electric fields, such as at 60 kV/mm [51]. The reduction in space charge with MgO can contribute to enhancing the electrical reliability of the polymer, particularly under high-voltage conditions, making it a valuable additive for insulating applications.

Silica (SiO_2), one of the most prevalent inorganic fillers, is extensively employed both in research and industrial applications. This widespread use is attributed to its effective blending capabilities, particularly through the sol-gel process, which allows for a homogeneous distribution of silica within the polymer matrix. According to research by [52], incorporating silica particles into polyethylene led to an observable increase in the material's voltage endurance, thereby extending its useful life under electrical stress. This enhancement in dielectric strength is particularly valuable in applications demanding prolonged stability and reliability under high electric fields.

Titanium dioxide (TiO_2) is another versatile additive that exists in two crystalline forms: anatase and rutile. The anatase phase of TiO_2, when used in epoxy resin, has demonstrated favorable outcomes in terms of improving the electrical resistivity of the composite material. Studies, such

as the one conducted by [53], have shown that anatase TiO_2 slightly increases both components of complex permittivity in the polymer matrix. Additionally, TiO_2 has been associated with improvements in mechanical properties, including enhancements in tensile modulus, tensile strength, and fracture toughness. The work by [54] highlighted these mechanical benefits, alongside gains in thermal conductivity, making TiO_2 an advantageous additive for applications requiring both electrical and structural reliability.

Alumina Al_2O_3 is widely used as a filler material in epoxy resins, particularly in GIS spacers, where it is applied in high concentrations, sometimes reaching up to 60-70% by weight. An article reported that incorporating alumina into epoxy significantly increased thermal conductivity, shear storage modulus, and fracture toughness when compared to the unfilled resin [55]. This filler not only improves thermal management within the polymer but also enhances mechanical resilience, making it an ideal additive for structural applications. Furthermore, alumina has been shown to positively influence the dielectric strength of epoxy-based materials, as demonstrated by [56], with improvements in electrical insulation properties achieved without compromising the material's dissipation factor. Recent work [57] also observed modifications in the trap distribution with varying alumina content, suggesting potential alterations in charge transport properties within the material.

2.1.4 Carbon-based nanomaterials

Carbon-based nanomaterials are characterized by unique properties which render them extremely promising candidates if employed as fillers. More specifically, they manage to modify electrical, thermal and mechanical properties of the matrix in which they are incorporated. Fullerene (see Fig.2.5) is one of the possible allotropic structures of carbon. In particular, they create a complex geometric structure resembling a football, composed of 12 pentagons and 20 hexagons. Their diameter is in the order of 10 nm. One of the primary advantages of incorporating fullerenes into materials is their ability to improve electrical conductivity. When added to polymers or composites, fullerenes can create conductive pathways, enhancing the overall electrical performance. This is particularly beneficial in the development of conductive coatings, sensors, and electronic devices. For example, studies have shown that the addition of fullerene-based gel to poly(3,4-ethylenedioxythiophene) (PEDOT) [58] can significantly improve the material's conductivity and stability, making it suitable for applications in organic photovoltaics and flexible electronics.

Carbon nanotubes, illustrated in Fig. 2.5, are unique nanostructures that arise from the repetition of the chemical framework characteristic of fullerenes. These remarkable materials possess a high degree of electrical conductivity, which can be finely tuned to adjust their properties, enabling them to function either as conductive or semiconductive components. This versatility opens up a wide range of potential applications in the electronics sector, where such materials are increasingly sought after for their ability to enhance device performance. In addition to their electrical properties, carbon nanotubes exhibit excellent stress-strain relationships, which contribute to their effectiveness in the development of mechanically reinforced nanocomposites. Their ability to withstand significant mechanical stress while maintaining structural integrity makes them an ideal filler material for enhancing the mechanical properties of various base materials [59]. As a result, incorporating carbon

nanotubes into composite matrices can lead to substantial improvements in strength, toughness, and overall durability.

Graphene is a remarkable material composed of a single layer of carbon atoms arranged in a two-dimensional honeycomb lattice. This unique layered structure bestows graphene with an extraordinarily high electrical conductivity, with values that can reach up to 600,000 S/m, which is significantly higher than that of many conventional conductive materials. In addition to its impressive electrical properties, graphene also demonstrates outstanding mechanical strength, with tensile strength values on the order of 1 TPa. This remarkable strength makes graphene one of the strongest materials known, surpassing that of steel and many other traditional materials. [60] Consequently, graphene is considered an extremely promising candidate for use as a nanofiller in a variety of research applications, where its incorporation can significantly improve the performance characteristics of polymer matrices and other composite materials. Despite its tremendous potential, the widespread industrial application of graphene has been hindered by challenges associated with its mass production. The current methods for fabricating graphene at scale are often not cost-effective, which limits its accessibility for commercial use. All carbon nanostructures are reported in Fig. 2.5

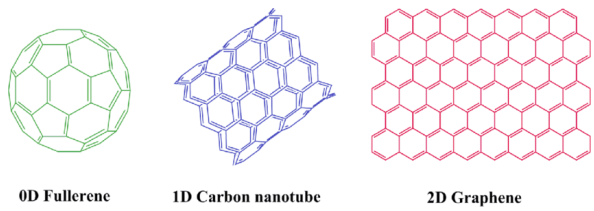

Figure 2.5: Carbon nanostructures, from [61]

2.2 Materials and fabrication method

2.2.1 Epoxy resin chemical characteristics

The epoxy resin utilized in this study was DER332, which is a resin based on bisphenol-A diglycidyl ether. For the hardening agent, polypropylene-glycol-2-bisaminopropylether was selected; this compound is commercially known under the name Jeffamine D230. The molecular structures of both DER332 and the hardener, polypropylene-glycol-2-bisaminopropylether, are provided in Figures 2.6a and 2.6b, respectively. Additionally, Figure 2.7 illustrates the chemical reactions involved in the curing process. In reaction 1, a primary amine (RNH_2) reacts with an epoxide group, resulting in the formation of a secondary amine. This reaction opens the epoxide ring, forming a hydroxyl (OH) group adjacent to the newly created secondary amine. This process initiates the cross-linking process and contributes to the formation of a branched polymer network. This primary addition is key in creating sites for further reactions, as the generated secondary amine retains one reactive nitrogen-hydrogen bond, which can further participate in subsequent reactions with additional epoxide groups. The secondary amine generated in the previous step can further react with another epoxide group, as in reaction 2. In this reaction, the secondary amine (R'RNH) opens an additional epoxide ring, producing a tertiary amine along with another hydroxyl group. This secondary

amine addition is critical for building the network's density and creating additional branching within the polymer structure. By converting secondary amines to tertiary amines, this reaction step contributes to the robustness and rigidity of the final polymer network, which enhances the material's mechanical properties. Once primary and secondary amine additions have occurred, the hydroxyl groups generated during these processes can also react with epoxide groups in a reaction known as etherification. Here, the hydroxyl group reacts with the epoxide, opening the ring and forming an ether linkage, with an additional hydroxyl group in the structure. Etherification is significant because it introduces ether bonds into the polymer chain, which helps enhance flexibility while also contributing to the cross-linked network. The curing process is typical of epoxy resins utilizing an amine-based curing agent, wherein the reaction sequence involves a complex reticulation mechanism.

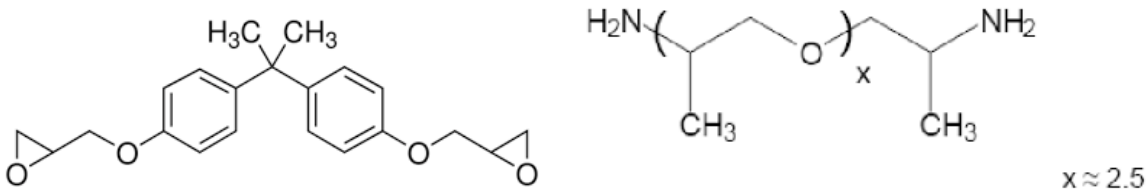

(a) DER332 (b) Jeffamine D230

Figure 2.6: DER332 and its curing agent Jeffamine D230

This process initiates with the opening of the epoxy ring, leading to the formation of hydroxyl groups. Subsequently, a structured network of covalent bonds is established, which interconnects the resin molecules and forms a stable, cross-linked polymer matrix. This network formation is fundamental to achieving the final mechanical properties of the cured resin, as the covalent bonding confers enhanced rigidity, strength, and durability to the epoxy polymer.

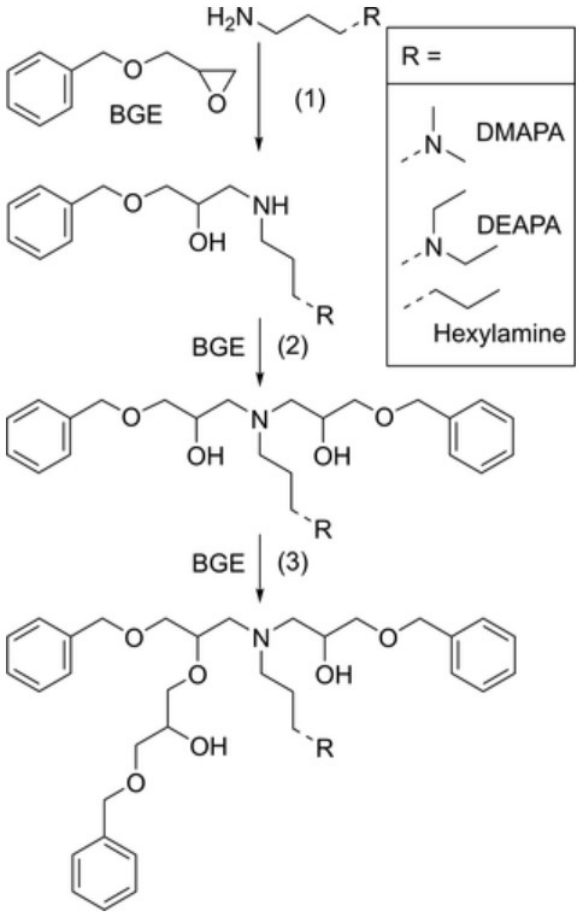

Figure 2.7: Chemical curing reactions, as in [62]

2.2.2 Quantum Dots and Quantum Confinement Effect

Quantum Dots are nanoscale semiconductor particles with dimensions typically ranging from 2 to 10 nanometers in all directions (Fig. 2.8), giving them unique optoelectronic properties. Due to their size, QDs exhibit distinctive behaviors that are not present in bulk materials, making them highly versatile for advanced applications. The most commonly used QDs are semiconductor-based, enabling them to absorb and emit light at specific wavelengths with high precision and efficiency. This property is particularly useful in optoelectronic devices, where QDs are applied to enhance color purity and efficiency in LEDs, improve sensitivity in photodetectors, and increase the power conversion efficiency in photovoltaic cells.

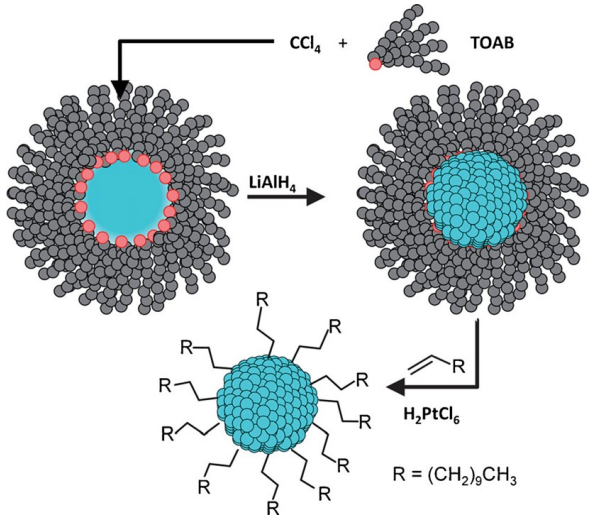

Figure 2.8: Quantum Dot, from [63]

Quantum Dots are typically categorized into two main structural configurations: core-only and core-shell. In the core configuration, a single semiconductor material forms the nanoparticle's core. The core-shell structure, on the other hand, includes an additional outer shell layer surrounding the core. This design improves stability, minimizes defects, and can enhance the quantum yield and brightness of the dots. Several types of QDs are now commercially available, including novel variants such as graphene quantum dots, which offer additional benefits due to their high conductivity, stability, and environmental compatibility.

The unique optoelectronic properties of QDs make them valuable in a wide range of applications. In bioimaging, for example, QDs are used as fluorescent markers due to their stability and tunable emission spectra, allowing for precise imaging at the cellular and molecular levels. In photovoltaic cells, QDs contribute to enhanced light absorption and flexible design options, which can increase solar energy capture and efficiency. Their application in light-emitting diodes (LEDs) has also revolutionized display technology, as QDs enable vibrant, high-purity colors and improved energy efficiency. The adaptability and multifunctionality of QDs continue to make them a focal point for innovation in materials science, with ongoing research dedicated to expanding their application potential across various high-performance technologies.

Quantum Dots, due to their nanoscale structure, inherently confine charge carriers within a localized region (Fig. 2.9). This occurs because QDs function as three-dimensional potential wells for electrons and holes, altering the wave functions of close charge carriers. As a result, the mobility of carriers within a spherical region centered on the Quantum Dot and defined by a radius equal to the Bohr radius is significantly reduced in all spatial directions. This characteristic makes QDs particularly interesting for applications in electrical insulation, as they can serve as effective traps for charge carriers, potentially enhancing the insulation properties of materials by limiting undesired charge transport through the material matrix [64].

Recent studies have explored the incorporation of Quantum Dots into insulating materials, aiming to exploit their ability to localize charge [65]. Although this trapping effect might initially seem undesirable, as it suggests a potential for increased charge retention, research indicates that a carefully

engineered high-trap-density nanocomposite layer can offer significant advantages in managing space charge injection. By inserting a nanocomposite layer with a high density of Quantum Dots or similar trapping sites between the insulating material and the electrodes, it is possible to control space charge injection mechanisms more effectively [66]. This approach allows for modulation of charge carrier dynamics at the material interfaces, improving overall insulation performance by reducing electric field distortions and stabilizing the material's dielectric properties over time.

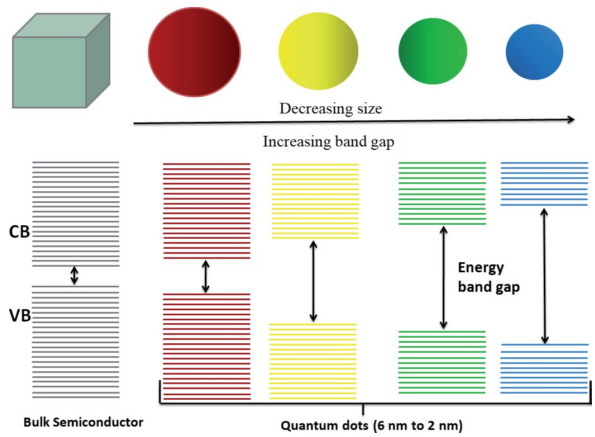

Figure 2.9: Quantum Confinement Effect, after [67]

2.2.3 Sample fabrication process

The sample fabrication is extremely similar to in situ polymerization and involved several steps which are here reported. Firstly, release agent was applied to the whole of a steel mould surface of dimensions 12 cm x 18 cm so as to impede the attachment of cured resin. A spacer was cut from a PET sheet of thickness in the range 200-250 μm with dimensions compatible with the mould and with holes in correspondance of the screw positions. Then, epoxy pre-polymer was heated at 50°C for 1 hour to reduce viscosity and was casted, commingled with the correponding amount of curing agent and of additives in case of nanocomposites, through the input profiles of the upper face of the mould. It then underwent vacuum conditions to remove the air in the prepolymer and was put in an oven to perform the curing process at 80 °C for 2 hours. Subsequently, a postcuring process was started, which lasted 3 hours at 125°C. This procedure was followed as suggested by [68].

To fabricate the nanocomposite, two additional steps supplement the standard procedures used for preparing a neat sample. First, the epoxy prepolymer undergoes an ultrasonication psrocess with a solution containing Quantum Dots to ensure uniform distribution and effective interaction between the Quantum Dots and the polymer matrix. This process enhances the dispersion of the nanofillers, mitigating the risk of aggregation and promoting optimal integration. Following ultrasonication, the mixture undergoes a controlled vacuum thermal process designed to remove the solvent entirely from the composite. This step is essential to avoid residual solvent presence, which could interfere with the material's structural and electrical properties.

The specific Carbon Quantum Dots used in this process were supplied in a polyvinylpyrrolidone (PVP) solution, at a concentration of 1 mg/mL. These Quantum Dots were pre-functionalized with carboxylic acid groups (–COOH), which facilitate bonding and improve compatibility with the epoxy

matrix. To remove the solvent, the nanocomposite was subjected to a thermal treatment at 70°C for an extended period, typically overnight. Under these conditions, effective solvent evaporation is achieved without compromising the Quantum Dots' functional integrity, thereby ensuring their stable incorporation within the epoxy matrix. The whole process is shown in Fig. 2.10, and the weights of the components of each sample are reported in Table 2.1.

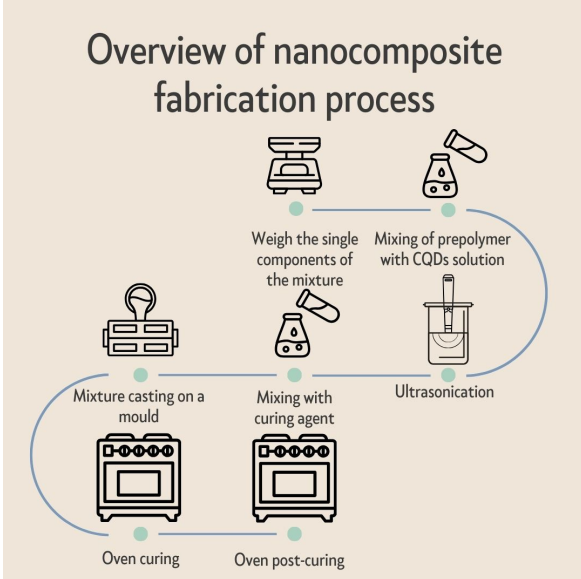

Figure 2.10: Nanocomposite fabrication process

Sample	Pre-polymer mass (g)	Curing agent mass (g)	Solution mass (g)
Neat epoxy	5.2	1.8	-
0.04% nanocomposite (or EP NC 0.04% wt.)	5.2	1.8	8.4
0.1% nanocomposite (or EP NC 0.1% wt.)	5.2	1.8	16.8

Table 2.1: Chemical composition of samples

Chapter 3

Experimental methods

3.1 Chemical characterization methods

3.1.1 DSC

Differential Scanning Calorimetry (DSC) is a powerful thermal analysis technique widely used for the characterization of polymeric materials. It allows for the precise measurement of heat flow associated with transitions in a material as a function of temperature, typically over repeated heating and cooling cycles. In DSC experiments, the sample and a reference material are subjected to identical thermal conditions, and the instrument records the heat flow required to maintain the same temperature in both, whose typical behaviour is shown in Fig. 3.1. This differential heat flow is indicative of thermal events occurring within the sample, providing valuable insights into its thermochemical properties.

One of the primary applications of DSC in polymer analysis is the determination of the glass transition temperature (T_g), a crucial thermal property for amorphous and semi-crystalline polymers. The glass transition temperature marks the boundary between the glassy, rigid state of a polymer and its rubbery, more flexible state. As the polymer is heated and approaches T_g, there is a marked increase in heat capacity, which is observed as a subtle step change in the thermogram (the graphical output of a DSC experiment). This transition is particularly important because it is linked to the mechanical and thermal stability of the polymer in various applications. Several methods are available to find the value of T_g; in this work, it is identified as the maximum of the derivative of the heat flow with respect to temperature, which corresponds to the inflection point in the thermogram.

In addition to identifying the glass transition, DSC is instrumental in studying crystallization and melting behaviors in semi-crystalline polymers. Crystallization refers to the process where polymer chains organize into a more ordered, crystalline structure as the temperature decreases. During DSC cooling scans, exothermic peaks in the thermogram indicate the release of heat as the material crystallizes. On subsequent heating, the melting process is observed as an endothermic peak, representing the energy absorbed by the polymer to overcome the ordered crystalline structure and transition to an amorphous, disordered state. The temperatures associated with these exothermic and endothermic events are key for understanding the thermal history of a polymer, its crystallinity, and its melting point (T_m).

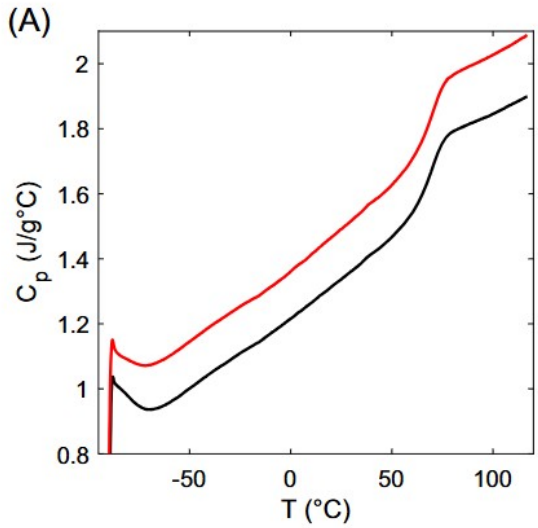

Figure 3.1: DSC typical heat flow, as in [69]

DSC analyses were carried out using a TA Instruments Q2000 DSC apparatus, represented in Fig. 3.2, calibrated with Indium standard, and equipped with a refrigerated cooling system (RCS90). Samples were loaded into standard aluminum pans and underwent the following thermal treatments: i) First heating ramp from –88 to 200 °C; ii) cooling ramp to –88 °C; iii) 2nd heating ramp to 200 °C. Heating/cooling rate was 20 °C/min.

(a) External appearance (b) Internal appearance

Figure 3.2: DSC Setup

3.1.2 TGA

Thermogravimetric Analysis (TGA) is a technique used to assess the thermal stability and composition of polymeric materials by monitoring weight changes as a function of temperature. In a typical TGA experiment, a sample is heated at a controlled rate in an inert or reactive atmosphere, and the corresponding weight loss is recorded on a thermogram. This weight loss, also representable in percentage as in the black curve of Fig.3.3, provides insight into the presence of volatile compounds,

such as absorbed moisture, residual solvents, or plasticizers, that evaporate from the polymer as it is heated. Additionally, TGA is essential for detecting mobile components within the material, which may vaporize or decompose at lower temperatures.

One of the key applications of TGA is the identification and quantification of organic content in polymeric materials. In an oxidative atmosphere, such as oxygen, TGA captures the decomposition of organic constituents as they undergo combustion, with the thermogram typically showing significant weight loss corresponding to these degradation processes. This makes TGA particularly effective in assessing polymer purity or identifying additives, fillers, and residual by-products from manufacturing processes.

In an inert atmosphere, such as nitrogen, TGA provides critical information on the thermal stability of the material itself. By observing the onset temperature of weight loss, researchers can determine the material's decomposition temperature, which is an important indicator of its thermal resistance. This data is essential for applications where polymers are subjected to high temperatures, as it helps define the maximum service temperature and predict the long-term thermal performance of the material.

TGA is a critical tool not only for determining thermal stability but also for supporting the design and optimization of polymer materials in various industrial applications. Through its ability to monitor mass changes across a wide temperature range, TGA delivers precise data on the degradation mechanisms, decomposition kinetics, and overall thermal behavior of polymers, allowing for better material selection and process control.

The thermal analysis of a material using TGA thermograms can be performed by calculating key parameters such as the temperatures corresponding to 3% and 50% mass loss. Additionally, the derivative of mass loss with respect to temperature, as the blue curve in Fig. 3.3 offers a more detailed examination of decomposition events, highlighting specific degradation steps. Comparing these thermogravimetric features across different samples provides valuable insights into their thermal stability and decomposition mechanisms, allowing for the identification of underlying physical and chemical processes responsible for the observed behavior.

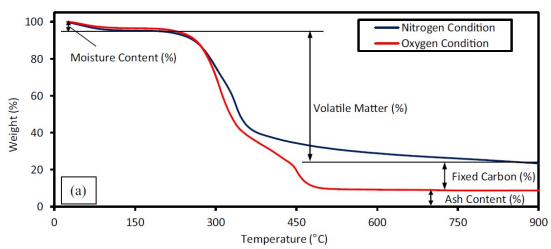

Figure 3.3: Typical thermogram coming from a TGA measurement, after [70]

TGA setup was a TG 209 F1 Libra, Netzsch. Samples were placed into alumina crucibles and heated at a 20 °C/min rate, from room temperature (20°C) to 800 °C. The samples underwent the same thermal treatment both under oxygen (thermoxidative degradation) atmosphere.

3.1.3 FTIR

Figure 3.4: FTIR Setup

Fourier Transform Infrared Spectroscopy (FTIR), whose setup is represented in Fig. 3.4 is an analytical technique widely used in the characterization of polymeric materials. By exposing a sample to an incident infrared (IR) wave, FTIR measures how the material absorbs or transmits specific wavelengths of IR radiation. The resulting spectrum, which consists of absorbance or transmittance peaks, as in Fig. 3.5is directly related to the vibrational modes of the molecular bonds within the polymer, such as bending, stretching, and scissoring motions. These vibrational modes are characteristic of specific functional groups, allowing FTIR to provide qualitative information by identifying chemical bonds and molecular structures within the material.

In addition to identifying chemical components, FTIR can also deliver quantitative data. The intensity of specific absorption peaks can be correlated with the concentration of certain chemical groups, enabling the quantification of components in complex mixtures or determining the degree of polymerization or crosslinking in a material.

3.2 Electrical characterization methods

All analysed samples underwent a vacuum procedure at 50°C in an oven, see Fig. 3.6a, before performing any test. This was a compulsory step, as it removed any residual volatile substance.

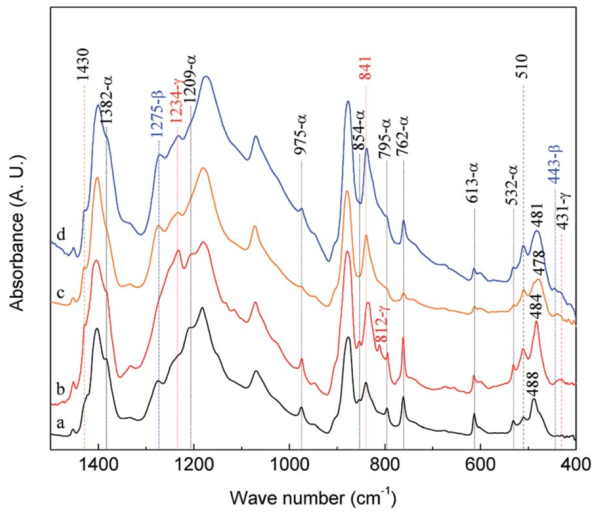

Figure 3.5: FTIR typical spectrum, after [71]

3.2.1 TSDC

The samples were metallized according to the Standard ASTM D-257 [72] for resistivity measurements, using the cold sputtering instrumentation in Fig. 3.6b. This requires a double-sided metallization, in particular a circular one on one side and a guard ring on the other one to avoid leakage currents interference on the measurement. Furthermore, the samples were grounded right after any measurement involving high voltage, in order to release any trapped space charge.

(a) Vacuum oven

(b) Cold sputtering setup

Figure 3.6: Pre-test experimental setup

During a TSDC test, the sample undergoes a sequence of different thermal and electrical conditions. In the initial step, there is an isothermal polarization phase, which, when applied to a an insulating sample, injects a large number of charge carriers by means of Schottky injection. Due to the structure of a polymer, the vast majority of electrons and holes will persist in the specimen in localised energetic levels, commonly called traps (Phase A). After this phenomenon has taken place, the sample is cooled down to -50°C, thus reducing dramatically the mobility inside the material and inhibiting the charge transport phenomena (Phase B). A depolarization phase follows under the same thermal conditions (Phase C). Eventually, the temperature is gradually increased with a constant heating rate, usually in the range 3-5°C/min. As a consequence, a variable current flow can be measured (Phase D). For the measurements the following setup was used: a Keithley 2290E-5 DC generator which goes up to 5 kV, a B2981A picoamperometer, a NOVOCONTROL system which uses liquid nitrogen as refrigerant fluid, and which comprises also the sample cell, a protection which consists in a resistance of 1 MΩ in series to an antiparallel configuration of two diodes. The measurements were performed on the neat sample and on the 0.1% nanocomposite. The trends of thermal and electrical parameters are exhibited in Fig. 3.7, while their values are reported in Table 3.1.

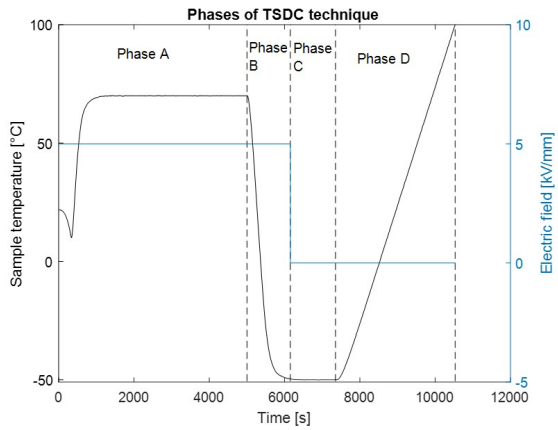

Figure 3.7: Phases of TSDC, as in [73]

Parameter	Value
T_p (°C) (Phase A)	70
T_l(°C) (Phases B and C)	-50
T_h (°C) (Max of phase D)	100
β (Heating rate in °C/min)	3
E (kV/mm) (Phases A and B)	10

Table 3.1: Thermal and electrical parameters during the different phases of TSDC

3.2.1.1 Phase A analysis

Characteristic relaxation time can be found from current flowing during Phase A. As a matter of fact, the current in this phase follows an exponential behaviour:

$$I = I_0 e^{-\alpha(T)t} \tag{3.1}$$

where α is the relaxation frequency of the material [74].

3.2.1.2 Phase D - Data analysis with Mizutani method

The resulting depolarization current trend with respect to temperature can be analysed by means of Arrhenius plots, in resemblance with several thermal processes. The parameters describing the relaxation process connected to the peak can be obtained by using initial rise method [75]. With this model, the low temperature tail of the Arrhenius plot can be approximated with the following expression:

$$J = J_0 e^{-\frac{E_a}{kT}} \tag{3.2}$$

Thus, from a linear fitting of the plot, it is possible to extract the value of the activation energy connected to each relaxation process, as in Fig. 3.8.

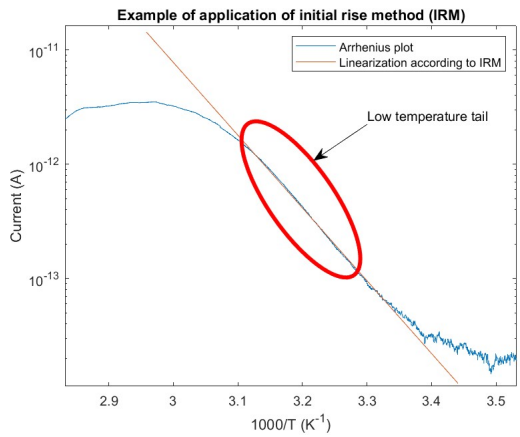

Figure 3.8: Example of application of Mizutani Method

From the value of activation energy, the temperature position of the peak T_M and from other thermal parameters in Table 3.1, it is possible to obtain an estimation of the attempt to escape frequency ν:

$$\nu = \frac{\beta E_a}{kT_M^2} e^{\frac{E_a}{kT_M}} \tag{3.3}$$

3.2.1.3 Phase D - Tian model

Further data processing leads to the knowledge of other information, such as the trap distribution [76]. This data processing requires the optimization of a function which depends upon trap depth and temperature:

$$G(E_a, T) = \nu e^{\frac{-E_a}{kT}} e^{-\frac{\int_{T_0}^{T} \nu e^{-\frac{E_a}{kT}}}{\beta}} \tag{3.4}$$

for each value of temperature, the specific activation energy that maximizes the function G(E_a,T) is then related to a value of trap density that can be extracted from the value of current density in correspondance of the temperature:

$$N_t(E_a) = -\frac{2dJ(T)}{el^2G(E_a,T)} \tag{3.5}$$

thus creating the trap distribution, as shown in Fig. 3.9. In the formula, d is the sample thickness, l is the localized energy level distance, usually put at 500 nm, and J(T) is the current density.

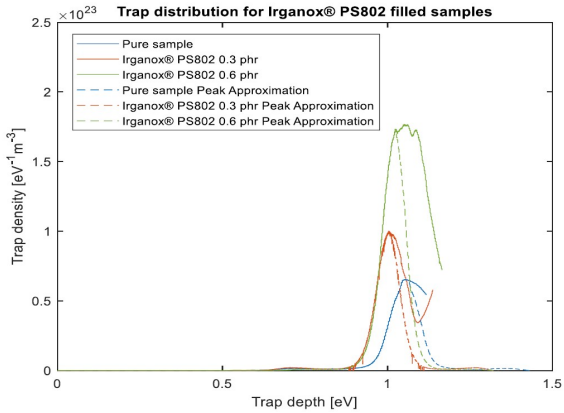

Figure 3.9: TSDC - Example of a trap distribution, from [77]

Each peak usually assumes a Gaussian-like shape around an energy value which thus corresponds to a local maximum. Thus, it corresponds to the energetic value in eV of the dominant trap depth. The area under each separate peak conveys other relevant information, i.e. the trap volumetric density introduced by the presence of a specific trapping process. A whole schematic of the analysis of TSDC in Phase D is shown in Fig. 3.10.

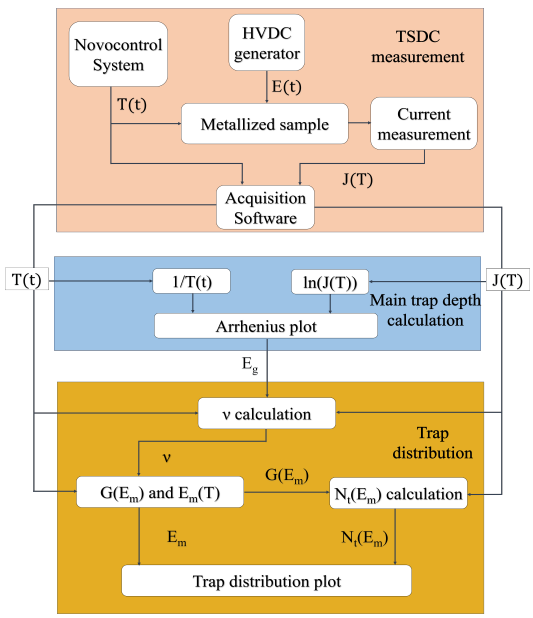

Figure 3.10: TSDC - Phase D analysis by means of Mizutani and Tian theory

3.2.1.4 Phase D - Data analysis with Bucci Fieschi Guidi

In the first 1960s, TSDC was still a developing technique; it was significantly improved in its theoretical implications by three Italian scientists, namely Bucci, Fieschi and Guidi [78]. What they achieved was the acknowledgment that several phenomena occurring during the TSDC process could be better understood if the relaxation time was considered. In particular, the expression of the relaxation time is the following:

$$\tau = \frac{P_s(T)}{J(T)} \tag{3.6}$$

with P_s the residual polarization defined as:

$$P_s(T) = \int_t^{+\infty} J(T)dt \tag{3.7}$$

and with J(T) current density at the specific temperature T occurring at time t. One of the main achievements is that relaxation times tend to have an Arrhenius behaviour, dictated by an activation energy E_a:

$$\tau = \tau_0 e^{\frac{E_a}{kT}} \tag{3.8}$$

Thus, it is possible from any logaritmic plot of the calculated relaxation time with respect to the temperature inverse, to extract data concerning the polarization phenomena occurring in phase D. The parameters describing the experimental procedure of TSDC are reported in Table 3.1.

3.2.2 Pulsed ElectroAcoustic Method

There are numerous space charge measurement techniques, involving among the others Pressure Wave Propagation (PWP), Laser Intensity Modulation Method (LIMM) and Pulsed ElectroAcoustic method (PEA). The latter has seen a growing interest in last years, up to its inclusion in IEEE recommended practice for Space Charge measurements for HV systems up to 550 kV [79]. It consists in the conjoint application of electrical DC voltage and electrical AC pulse voltage to an insulating sample in order to measure space charge distribution. The setup, schematized in Fig. 3.11a includes a resistor interlarded between the DC generator and the sample and a capacitor in series to the pulse generator to avoid DC high currents to disrupt the pulse generator working, respectively. The interaction of these 2 voltages with the trapped carriers induces an acoustic wave travelling all across the sample. The charge carrier density is considered uniform along a 2D section of the sample and it is proportional to the intensity of the acoustic wave. Furthermore, a piezoelectric transducer for the part of the acoustic wave which is transmitted through both the specimen and the lower electrode. Eventually, the amplitude of the output signal of this sensor is magnified by a 40 dB operational amplifier and sent to an oscilloscope for waveshape visualization. After a calibration procedure which relates the measured voltage with the effective charge density inside the sample has been carried out, it is also possible to compute the electric field distribution.

All PEA experiments were performed under predefined electrical and thermal conditions, namely under an electric field of 20 and 30 kV/mm and temperatures of 25, 40 and 60°C. The tests underwent

an initial polarization phase lasting 3 hours and a final depolarization phase for 1 hour. The setup is represented in Fig. 3.11b

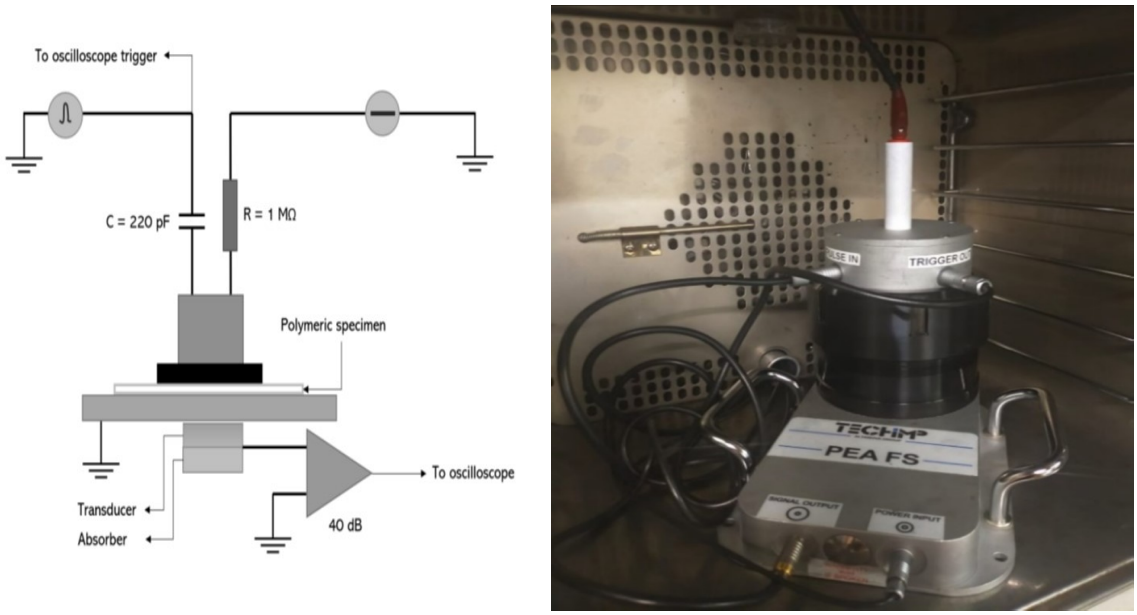

(a) PEA schematics

(b) PEA setup

Figure 3.11: PEA setup

3.2.2.1 PEA data analysis

The signal measured by the oscilloscope connected to the PEA system output is a voltage proportional to the amount of space charge in the sample. The used software is able to perform a reconstruction, managing to convert the voltage signal into space charge localized at certain positions inside the samples. To achieve this goal, first the software asks the instant at which no space charge injection occurred (usually, one of the initial signals, but not the first, as the DC generator required some seconds before giving the whole electrical stress). In this way, all the following signals will be modified by subtracting the initial signal. Then, the software needs to know the inner and outer limits of the electrodes. Once these operations have been performed, the software computes the electric field and space charge distributions. These are obtained by first finding a calibration constant which makes the peaks of the electrodes match the surface charge accumulated at the electrodes due to the action of electric field. Then, the corresponding space charge distribution time evolution can be computed by multiplying the PEA voltage signal by this calibration constant. This can be used both to plot the space charge distribution along the sample right after polarization has begun and some instants before the volt-off, as in Fig. 3.12a, and the space charge pattern time evolution with a color map, as in Fig. 3.12b. Moreover, it is possible to obtain the average absolute value, as in Eq. 3.9 [80].

$$Q(t) = \frac{1}{L}\int_0^L |\rho(x,t)|dx \tag{3.9}$$

and plot its evolution with time as in the light blue curve of Fig. 3.12c. Then, remembering

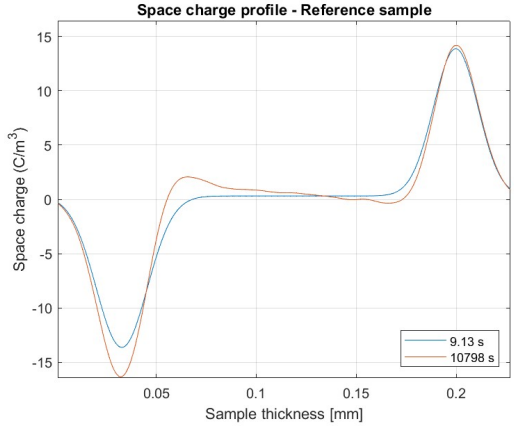

(a) Space charge profile

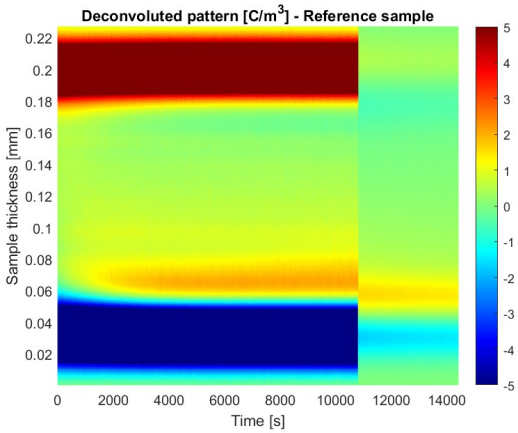

(b) Space charge pattern

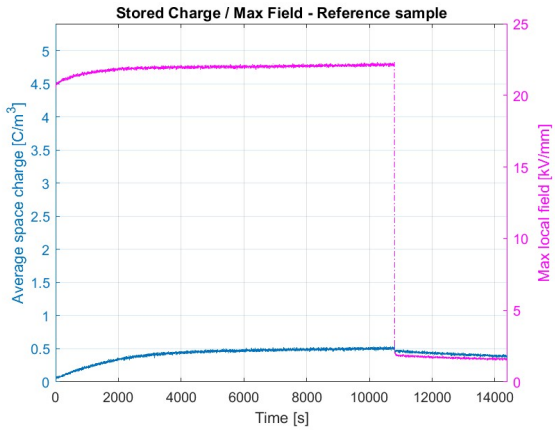

(c) Electric field and average space charge time evolution

Figure 3.12: PEA plots

Gauss' equation:

$$\nabla \cdot E = \frac{\rho}{\epsilon} \tag{3.10}$$

and considering that we are considering a 1D model, the divergence can be considered a derivative. Thus, it is possible to obtain the electric field distribution by integrating the space charge distribution with respect to spatial coordinate, and multiplying by the permittivity. From this distribution, it is possible to obtain the maximum value for each time instant. There is also the possibility of getting a time evolution of the maximum electric field inside the sample and an estimation of the trap depth and density (even though the latter are limited in a range above 0.7 eV, thus not being able to detect more shallow traps).

3.2.3 Dielectric spectroscopy

All the described measurements were performed under 3 V AC, with frequency varying in the range $10^{-2} - 10^{6}$ Hz; the analysed temperatures were respectively: -20, 0, 20, 40, 50, 60, 70, 80, 90, 100°C. This specific set of values was selected as it was preferred to give more resolution in the higher values of temperature, without completely losing information regarding the low temperature processes. The

used setup is represented in Fig. 3.13.

Figure 3.13: Dielectric spectroscopy setup

Broadband Dielectric Spectroscopy technique is deployed in several fields of application. The most common samples are polymeric insulating samples, but countless alternatives are possible, including analysis of properties of biological systems [81] and of grocery [82]. More specifically, it is a measurement which, by applying a variable frequency AC voltage, can assess a sample dielectric properties. When a sinusoidal voltage is applied, the specimen response is represented by a sinusoidal current, shifted with respect to the reference phasor of the voltage in Steinmetz plane. If the current is measured by an amperometer, the impedance

$$Z(\omega) = \frac{V(\omega)}{I(\omega)} \tag{3.11}$$

can be calculated. For this reason, the interpretation of this experimental outcome is also known under the name of Impedance Spectroscopy [83], even though this term is usually related to an investigation of the electrochemical processes, thus with reference to batteries, fuel cells, etc... [84, 85]. In real measurements, the argument of the impedance slightly deviates from the ideal angle of -90° characteristic of a capacitor, thus showing a small resistive behaviour. From this calculation and from Debye equivalent circuit, it is possible to extract the value of the complex permittivity.

$$\epsilon^* = \epsilon' - j\epsilon'' \tag{3.12}$$

knowing the geometrical factors given by the active area (the one in intimate contact with the electrodes) and the diameter of the sample. It is widely known that the imaginary part and dissipative factor plots usually exhibit several peaks. Each of them is connected to a different polarization mechanism, whose corresponding frequency is strongly dependent upon the inertia of the entity undergoing the polarization process, as shown more in detail in Fig. 3.14. In particular, more

massive bodies correspond to lower frequencies and viceversa. High frequency peaks in the range $10^{17} - 10^{12}$ Hz correspond to electronic and atomic polarization, also called deformation polarization. This kind of polarization is extremely difficult to detect with traditional techniques, and resonant cavities or optical methods are required. The NOVOCONTROL used in experimental measurements can achieve good results in the range $10^{-2} - 10^{6}$ Hz. In this range the most common polarization process is the dipolar one, correlated to the orientation of dipoles in the material as a response to the applied electrical alternating stress. Finally, other peaks can be found in the range $10^{-6} - 10^{-2}$, usually linked to interfacial polarization or to electrode polarization. This last range is usually particularly difficult to analyse, due to conductive quasi-DC behaviour, which is underscored by the corresponding appearance of a plateau in conductivity and a straight line of slope almost -1 in the imaginary permittivity. Nonetheless, a method might be able to reconstruct the real trend of ϵ" in the low frequency region, namely Kramers-Kronig. It performs a numerical calculation of the derivative of the real part of permittivity, which is approximately equal to the imaginary part. The approximation comes from the limited measurement range, as to obtain the exact value, all the spectrum from f=0 to infinity should be known.

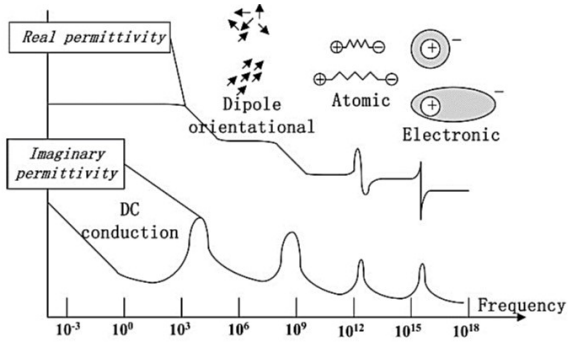

Figure 3.14: Typical BDS spectrum

3.2.3.1 Cole-Cole plot

Complex permittivity can be represented without the explicit dependence on frequency by plotting its imaginary part as a function of real part. This is called the Cole-Cole plot. In the hypothesis of a single Debye relaxation process, a perfect single semicircumference should be the corresponding plot. It goes without saying that there might be more than one of these figures each corresponding to a single relaxation process. This is a consequence of the conjoint resistive and capacitive natures of an insulating sample. The corresponding radius lying on the real axis has as extremes the values ϵ_S and ϵ_{inf}, which are the real permittivity values at very low and very high frequency, respectively. In reality, there are numerous possible departures from this ideal behaviour, which generate different geometric figures and which are usually taken into account with three different theoretical models: Cole-Cole [86], Cole-Davidson [87] and Havriliak-Negami [88]. The difference in these models stands in their ability to correctly describe experimental data and in their explanation of the undergoing physical mechanisms. For example, Cole-Cole and Cole-Davidson models have an underlying theory based upon the distribution times of the polarization mechanisms. Havriliak Negami instead manages to describe a wider class of relaxation spectra, but research on the physical mechanisms leading to the

frequency dependence of real and imaginary permittivity it is still ongoing. An example of a typical behaviour in a Cole-Cole plot is shown in Fig. 3.15.

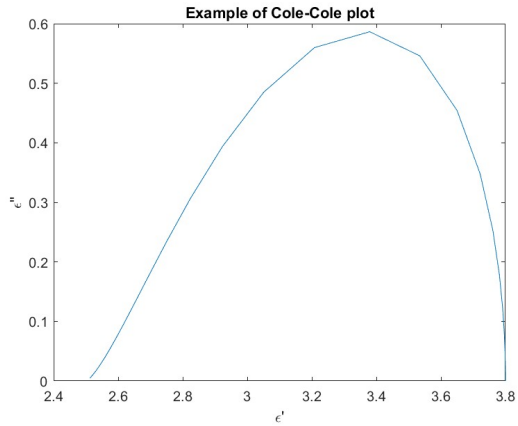

Figure 3.15: Typical Cole-Cole plot

3.2.4 Temperature dependence of Dielectric spectrum

Another fundamental feature of dielectric relaxation trend is its dynamics owing to the effect of temperature. The peaks of imaginary permittivity and modulus, in fact, tend to shift towards higher frequencies with rising temperature with polymer insulating samples. This can be reconduced to two main processes, namely α and β relaxations. The first are linked to segmental motion of the backbone, whereas the second can be ascribed to the side functional groups of the considered polymer [89]. The mathematical modelling for alpha relaxation is represented by Eq. 3.13

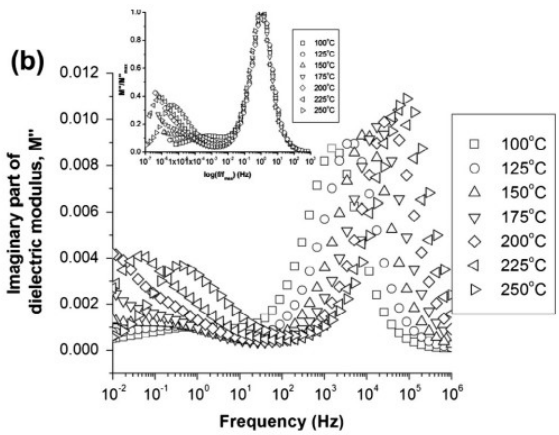

Figure 3.16: Typical behaviour of Arrhenius shifting, as in [90]

$$f = f_0 e^{\frac{C}{T - T_\alpha}} \tag{3.13}$$

where T is usually 30-40°C less than the glass transition temperature, whereas the β relaxation can be described by Eq. 3.14

$$f = f_0 e^{\frac{-E_a}{kT}} \tag{3.14}$$

thus resembling an Arrhenius process with activation energy E_a.

3.2.4.1 Further analysis

Imaginary part of the electrical modulus, defined as the inverse of complex permittivity, has a different time constant as opposed to the imaginary permittivity, in particular towards higher frequencies [91]. This lets it convey valuable information whenever a relaxation process is significantly shifted towards lower frequencies in imaginary part of permittivity, as it can be used to compute Arrhenius analysis real part of AC conductivity, defined by the following equation:

$$\sigma' = \omega\epsilon'' \tag{3.15}$$

It can provide further information on the conduction mechanisms inside the sample. In fact, an ideal insulating material is characterized by an oblique line with slope around -1 in this plot. Nevertheless, at low frequencies, a material can start experiencing the phenomenon of Quasi-DC conduction, induced by the presence of free charges which are characterised by high mobility, especially at higher temperatures. On the plot, this corresponds to a plateau reached in the low frequency region. Finally, in order to dismantle the effect of quasi-DC conduction which distorts the trend of the imaginary part of permittivity, an expression implemented by Kramers and Kronig can be used [92]:

$$\epsilon'' = \frac{-\pi}{2}\frac{\partial(log\sigma)}{\partial(log\omega)} \tag{3.16}$$

3.2.5 Bulk conductivity

The used setup is represented in Fig. 3.17a and 3.17b. It is made up of a Keithley 2290E-5 DC generator which goes up to 5 kV, and a B2981A picoamperometer, connected by means of a cable to the cell containing the insulating sample.

3.2.5.1 Polarization phase

When a DC high voltage is applied to a polymeric sample, it responds to the application of the input stress there are two main effects: an orientation of the dipoles, which results in a displacement current, and a conduction current due to free carriers. Their copresence implies an abrupt change in the current transient plot from an increasing almost linear function to a decreasing one. In usual measurements, the current density steady state value, which reflects the conduction process after the reorientation of the dipoles has occurred, is taken into consideration. From this value, by applying local Ohm's law, is possible to obtain the conductivity value:

$$\sigma = \frac{J}{E} \tag{3.17}$$

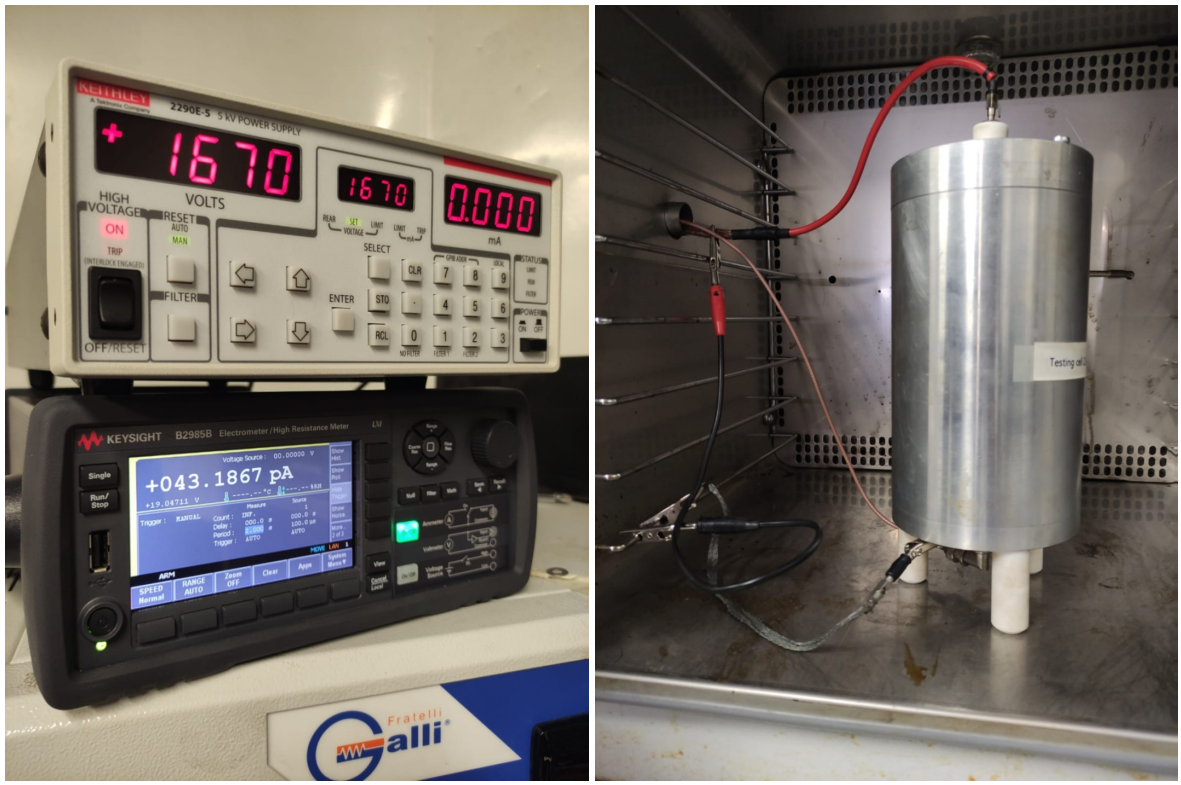

(a) Generator and picoamperometer

(b) Sample cell

Figure 3.17: DC conductivity setup

3.2.5.1.1 Transient analysis

The decreasing initial transient was first discovered by Curie [93] and von Schweidler [94]. It was modelled with the following decreasing power equation:

$$I = Ct^{-n} \tag{3.18}$$

with C and n constant coefficients. It has been recently studied from a theoretical point of view to create a mathematical model taking into account this behaviour [95], usually disregarded in conductivity studies in favour of a thorough analysis of steady state conduction current value in function of the applied voltage. In particular, it has been shown that it is possible to treat the insulator as a parallel between a constant phase capacitor and a resistance in series to another resistance, see Fig. 3.18.

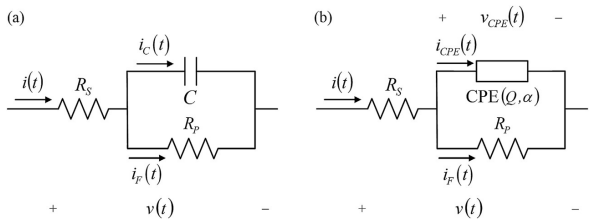

Figure 3.18: (a) Simplified RC model and (b) CPE element model [95]

where R_S and R_P are resistive parameters describing respectively the transient and the steady-

state trends, whereas Q and α are characteristic parameters of the material. In particular, the former is a generalization of the concept of capacitance, while the latter embodies the deviation of the real dielectric from the ideal capacitive behaviour (it depends on how much this parameter is distant from 1). The exact equation describing this circuit is extremely complicated, but thanks to some limit approximation, a final expression can be obtained which perfectly resembles the behaviour described by equation 3.18:

$$I = \frac{VQ}{\Gamma(1+\alpha)} t^{-\alpha} + V/R_P \tag{3.19}$$

where V is the applied voltage and Γ is the gamma function. The final expression is slightly simplified from the original expression in [95], as the parallel resistance is usually extremely higher than the series one in an insulating material, leading to some modifications in the original expression.

3.2.5.2 Charge emission from the electrodes

Another consideration regarding DC conductivity for polymers is its strong dependence upon both temperature T and applied electric field E, especially for extreme conditions. This behaviour has its foundations in the emitting current of an electrode in vacuum, which follows Richardson equation:

$$J = AT^2 e^{\frac{W}{kT}} \tag{3.20}$$

where A is the Richardson-Dushman constant, W is the barrier potential of the electrode and J the current density. When considering a single trap in a material, it is possible to show that, under a mechanism called Poole-Frenkel, there would be a drop in the potential given by

$$\Delta W = \beta_S \sqrt{E} = \sqrt{\frac{e^3 E}{4\pi\epsilon}} \tag{3.21}$$

where e is the elementary charge and ϵ the permittivity of the material. By including this result in Eq. 3.20, we obtain the Richardson-Dushman-Schottky equation

$$J = AT^2 e^{\frac{W-\beta_S\sqrt{E}}{kT}} \tag{3.22}$$

which shows that the process is contemporarily electrically and thermally activated. Other 2 possible emission processes are possible, namely Fowler Nordheim and photoemission, here cited for sake of completion. The former is based upon Wentzel-Kramers-Brillouin approximation to quantum mechanical calculations. It is a phenomenon occurring in the case of very small distances between the electrodes, in the order of some nanometers, corresponding to fields in the order of some MVs/mm. This mainly occurs in semiconductors. The corresponding current density is explicitly dependent only upon the electric field, and not on temperature anymore:

$$J = \frac{C}{\phi} E^2 e^{-\frac{4}{3}\frac{\sqrt{2}m^*(e\phi)^{\frac{3}{2}}}{ehE}} \tag{3.23}$$

where C is a constant, ϕ the potential barrier, m^* the efficient mass of the charge carrier and h the Planck constant. FInally, photoemission is based upon the incidence of light radiation on the emitting electrode. In this case, the energy given by the photons can be expressed using the relation

E=hv, where h is the Planck constant and v the frequency of light wave. In this interaction, electrons may be released with excess kinetic energy equal to

$$\Delta K = hv - e\phi \tag{3.24}$$

3.2.5.3 Space charge limited current

It is also important to remember the existence of a threshold value for electric field E_{th} which dictates the transition between Ohmic behaviour and space charge limited current behaviour of insulating materials. For this reason, from E_{th} onwards, the current density changes to:

$$J = \frac{9}{8}\frac{\epsilon\mu V^2}{L^3} \tag{3.25}$$

where V is the applied voltage and L the sample thickness. This is also known as Child's Law for insulators or Mott-Gurney law [96], and exhibits a square-law dependence of the current density with the electric field.

3.2.5.4 Depolarization phase

After the application of the DC voltage has lasted enough to reach steady state, conduction current can be calculated. Standard ASTM D-257 [72] evaluates this required time in the order of at least 8 hours, but 2 or 3 days may be necessary in general. At this point, it is possible to proceed with the measurement under depolarization conditions, by switching off the DC generator and continuing to measure the current. In this way, information regarding the very low frequency behaviour of dielectric relaxation can be extracted. In particular, it is possible to show that depolarization current J(t) can be linked to the response function of the dielectric g(t):

$$g(t) = -\frac{J_d}{\epsilon E} \tag{3.26}$$

with E the previously applied electric field. It is worth noting the presence of a negative sign in order to take into account the inversion of current flow due to depolarization. After this time-domain operation has been performed, it is convenient to move into frequency domain by applying Fourier transform to g(t):

$$\chi(\omega) = \mathcal{L}(g(t)) \tag{3.27}$$

obtaining complex susceptivity $\chi(\omega)$. This is strictly connected with complex permittivity.

$$\epsilon(\omega) = 1 + \chi(\omega) \tag{3.28}$$

This connection lets to obtain a trend of the permittivity for extremely low frequencies, such as below 1 mHz, a region not covered by Dielectric Spectroscopy setup.

Chapter 4

Results

4.1 Chemical characterization methods

4.1.1 DSC

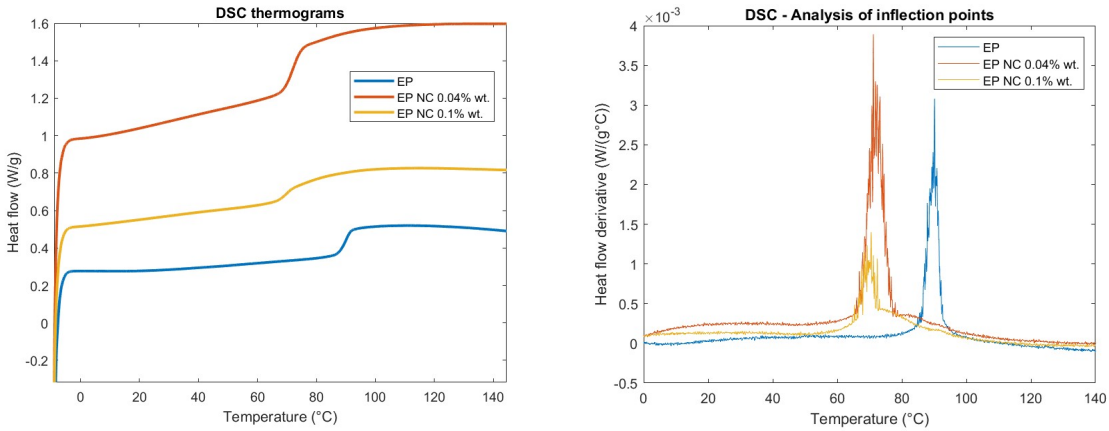

(a) Heat flow thermogram

(b) Heat flow derivative

Figure 4.1: DSC thermograms

The DSC thermogram of heat flow in Fig. 4.1a shows a clear behavior: the nanocomposites require higher heat flow than the neat sample; however, with increasing nanofiller content, the heat flow displays a decrease. The step in heat flow shifts from the neat sample to the nanocomposites, suggesting T_g is significantly different between them. In the DSC thermogram, the neat sample exhibits an almost flat heat flow curve at low temperatures. This behavior indicates minimal thermal activity in the neat sample during the initial heating phase. The heat flow remains steady with no significant fluctuations until the transition occurs, signaling a stable thermal profile in the absence of any filler materials. In contrast, the nanocomposites display a different behavior at low temperatures. Instead of a flat curve, the nanocomposites show an almost linear increase in heat flow with time or temperature. This gradual increase in heat flow continues until the point of the step transition is reached, marking a clear distinction from the neat sample's thermal behavior. The linear time evolution of heat flow in the nanocomposites indicates that thermal processes, possibly related to

the nanofiller interaction with the matrix, are already underway before the transition point.

Upon reaching the step transition, the neat sample again displays a relatively simple behavior. After the transition, the heat flow in the neat sample stabilizes and remains nearly unaltered, indicating that the material reaches a thermal equilibrium quickly and maintains this state with no further significant changes. The heat flow curve flattens out after the transition, suggesting that the neat sample quickly reaches a steady-state condition without any additional thermal events taking place beyond the step.

The nanocomposites, however, exhibit a more complex post-transition behavior compared to the neat sample. After the step transition, instead of immediately reaching a steady state, the nanocomposites display a more gradual progression towards thermal equilibrium. This represents a distinct deviation from the neat sample's behavior, as the heat flow does not immediately level off after the transition. Instead, the heat flow in the nanocomposites undergoes a more gradual reduction, taking longer to reach a steady state. The presence of the nanofiller appears to influence the heat flow profile, causing a more extended approach to thermal equilibrium compared to the neat sample.

The gradual reaching of a steady state after the transition is consistent across both nanocomposite samples, regardless of nanofiller content. This delayed stabilization of heat flow highlights a key distinction between the neat sample and the nanocomposites, as the latter demonstrate a more intricate response to the thermal environment after the step transition.

The analysis of the derivative in Fig. 4.1b provides further insights. The presence of shifted peaks is evident. Deriving T_g as the position of the peak of the derivative in Fig. 4.1b gives the results presented in Table 4.1, confirming the variation in T_g between the neat sample and the nanocomposites. In particular, a drop of around 20°C of glass transition temperature is found for both kinds of QDs.

Sample	T_g (°C)
Neat sample	90.0
0.04% nanocomposite	72.3
0.1% nanocomposite	70.0

Table 4.1: Glass transition temperature

4.1.2 TGA

Sample	T_3 (°C)	T_{50} (°C)
Neat sample	334	397
0.04% nanocomposite	220	397
0.1% nanocomposite	160	393

Table 4.2: T_3 and T_{50} parameters

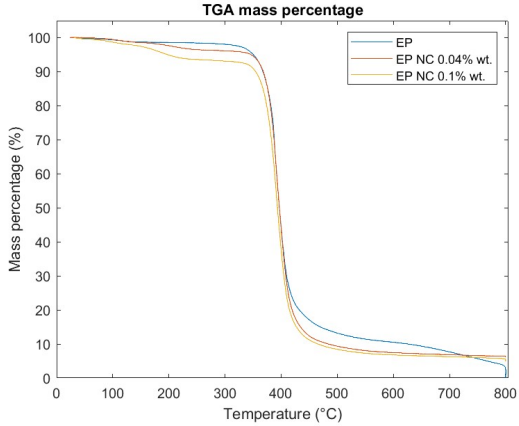

Figure 4.2: TGA mass percentage

The TGA thermogram in Fig. 4.2 presents some interesting trends. In particular, at lower temperatures, a small but not negligible discrepancy arises between the neat sample and the nanocomposites. This behavior is captured by the parameter T_3 in Table 4.2, which denotes the temperature at which 3% mass loss occurs. The T_3 values indicate a significant reduction from the neat sample to the nanocomposites, with this trend becoming more pronounced as the nanofiller content increases. This lowering of T_3 suggests an earlier onset of degradation in the nanocomposites compared to the neat sample, particularly as filler content rises.

At around 400°C, the most substantial mass loss occurs across all samples, a point represented by the T_{50} parameter reported in Table 4.3a, which marks the temperature where 50% mass loss is observed. Interestingly, T_{50} remains nearly identical for all materials, suggesting that while the onset of degradation shifts with increasing filler content, the major thermal degradation event occurs at a similar temperature for both the neat sample and the nanocomposites. This observation, based solely on mass percentage behavior, can be further refined and clarified through an analysis of the DTG curve, which reveals more detailed patterns in the thermal degradation process.

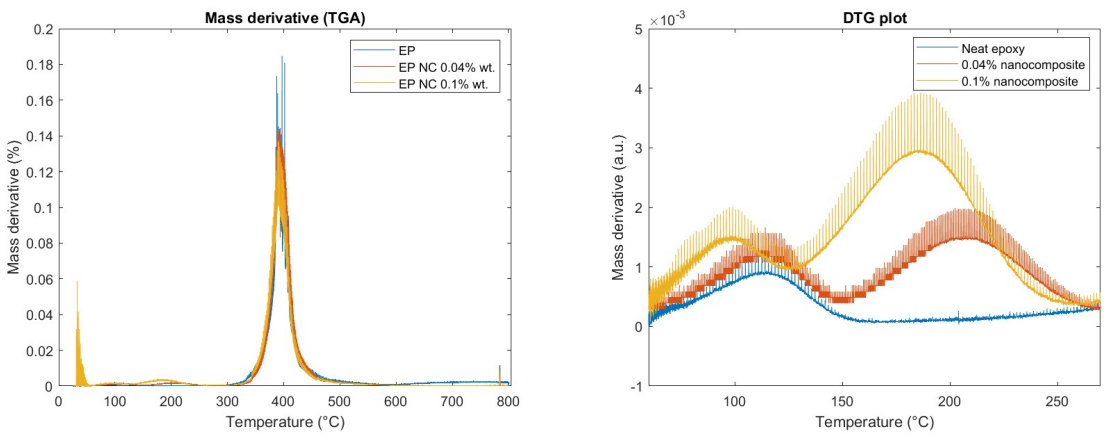

(a) TGA mass derivative

(b) Insight in 100-350°C region

Figure 4.3: DTG experimental results

In the DTG analysis, a prominent peak corresponding to the mass loss at around 400°C is

observed for all samples. The similarity in the peak shapes and positions indicates that the main degradation process occurs in a similar fashion, regardless of the presence or amount of nanofiller. However, focusing on the region between 100°C and 350°C provides valuable insights into how the nanocomposites differ from the neat sample in terms of their degradation behavior at lower temperatures.

More importantly, a distinct peak emerges in the nanocomposites that is not present in the neat sample. This new peak, which appears within the 100°C to 350°C region, grows in intensity as the nanofiller content increases. Additionally, the peak's position shifts progressively toward lower temperatures with higher nanofiller concentrations, as shown in Table 4.3.

Sample	T_p (°C)
Neat sample	-
0.04% nanocomposite	211
0.1% nanocomposite	187

Table 4.3: TGA Mass Derivative NC Peak position

4.1.3 FTIR

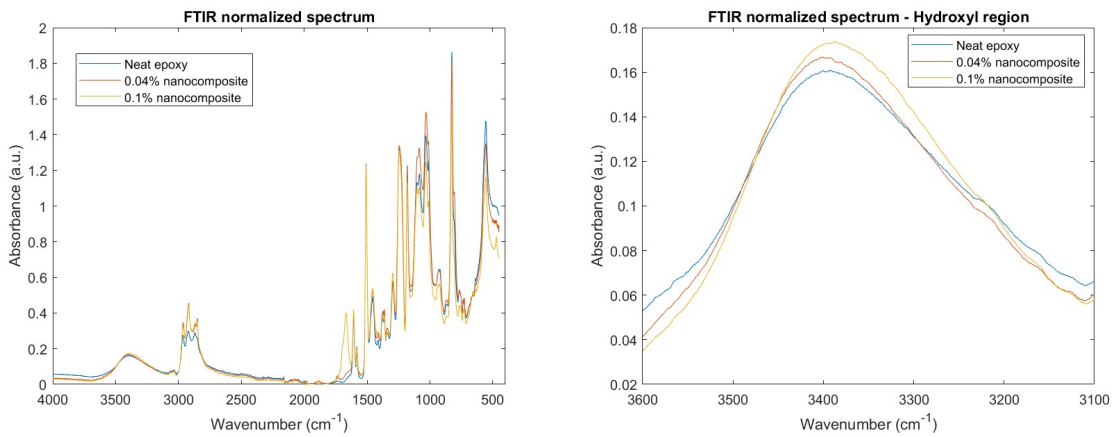

(a) Whole spectrum

(b) Hydroxyl region

Figure 4.4: FTIR whole spectrum and insight in high wavenumber region

The analysis of FTIR experimental results will proceed from higher to lower wavenumbers. The whole spectrum in Fig. 4.4a in general shows resemblance between each sample, but some key differences can be highlighted by giving insight to some specific regions of the spectrum. Starting from the high wavenumber region in Fig. 4.4b, it can be seen that the peak, typical for hydroxyl groups, is almost unvaried between the neat sample and the nanocomposites., with just a slight increase with nanofiller content.

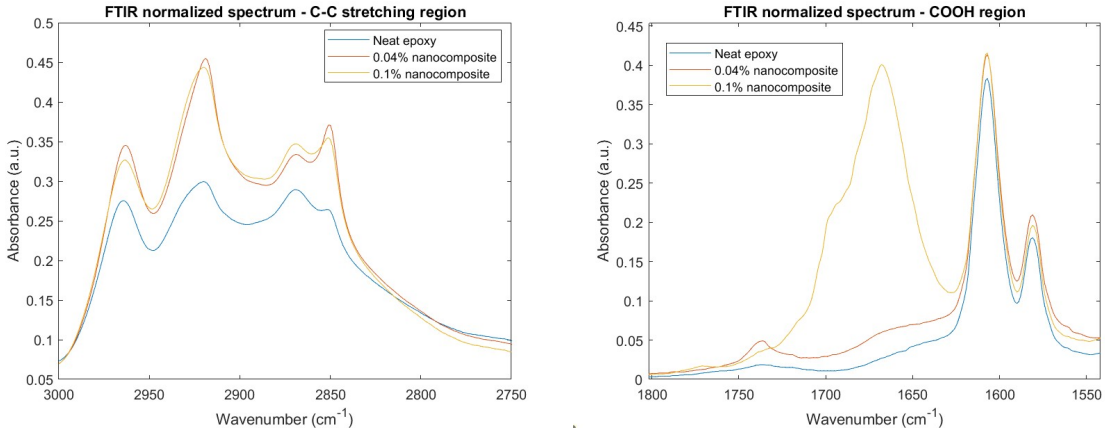

(a) C-C stretching region

(b) Carboxyl group region

Figure 4.5: Intermediate wavenumber regions

From 3000 to 2750 cm^{-1}, typical of the C-C stretching, the spectrum in Fig. 4.5a is characterized by a generalized strong intensifiction among the several peaks in this region when nanocomposites are tested, as shown in Fig. 4.5a. Nevertheless, no significant variation can be found between the two nanocomposites. The same can be said about the other region from 1800 to 1600 cm^{-1} in Fig.4.5b where some peaks appear showing variations with nanofiller content;

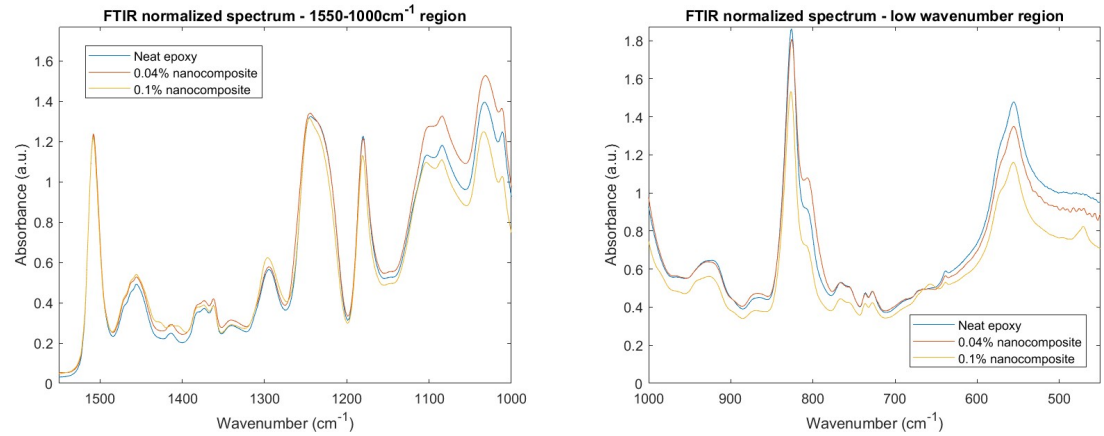

(a) 1550-1000 cm^{-1} region

(b) 1000-450 cm^{-1} region

Figure 4.6: Low wavenumber regions

in particular, the one on the left (around 1740 cm^{-1}) is extremely small and is more prominent for the 0.04% nanocomposite; the one at 1667 cm^{-1} has a slight variation between the neat sample and the 0.04% nanocomposite, in which the peak appears as a mild shoulder, and a tremendous increase when 0.1% nanocomposite is taken into account.

The peak around 1610 cm^{-1} shows a significant similar rise for both nanocomposites as opposed to the neat sample, which is almost unperturbed with higher nanofiller content. Finally, the peak on the right is characterized by an increase in absorbance in the nanocomposites if compared to the neat sample, but the 0.04% is higher.

The spectrum in Fig. 4.6a is generally characterized by an increase in absorbance for nanocomposites, with only a relevant exception for the peak around 1200 cm^{-1} which has the opposite trend, and the two peaks positioned at wavenumbers lower than 1100 cm^{-1} with anomalous behaviour. Finally, analyzing the spectrum in Fig. 4.6b between 1000 and 700 cm^{-1}, it is characterized by a general similarity between the absorbances of the peaks of neat sample and 0.04% nanocomposite, whereas the 0.1% nanocomposite has lower intensities.

4.2 Electrical characterization methods

4.2.1 TSDC

4.2.1.1 Phase A analysis

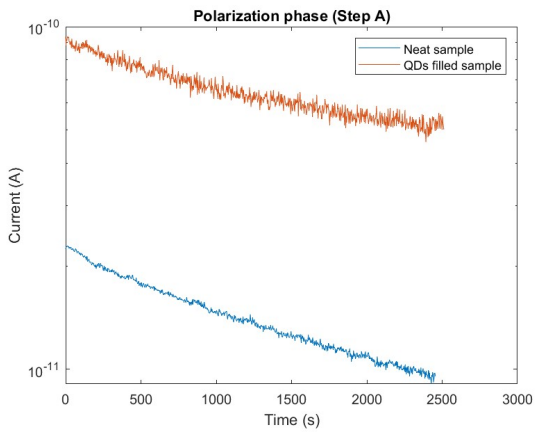

Figure 4.7: Phase A of TSDC

The first phase of TSDC is characterized by an initial thermal transient in order to control the environmental conditions under which the test is performed. After that, the temperature is kept stable. The initial transient is removed from the exposition in Fig. 4.7, which reports the time evolution in semilogarithmic plot of the current during Phase A. The information that can be extracted from the plot is the presence of an exponential behaviour, as suggested by the linear trend. The parameters extracted from the linear regression of the plot lead to a corresponding value of the frequency constant $\alpha(T)$ of around 300 μHz for the neat sample, as opposed to a value of 150 μHz for the nanocomposite.

4.2.1.2 Phases B and C

These phases do not give a significant contribution to the understanding of any physical phenomenon, but their trends are reported in Fig. 4.8a and 4.8b for sake of completeness.

4.2.1.3 Phase D analysis - Arrhenius plot

A simple consideration that can be drawn from the plot in Fig. 4.9, which reports the current as a function of temperature during Phase D, is that the nanocomposite is clearly characterized

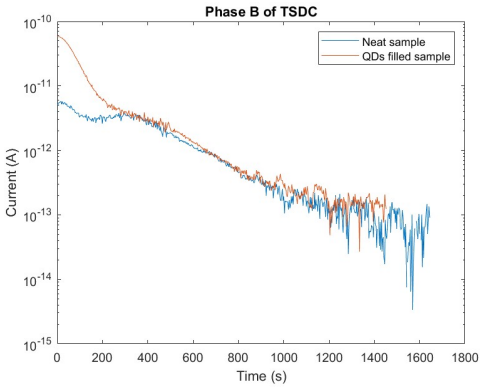

(a) Phase B

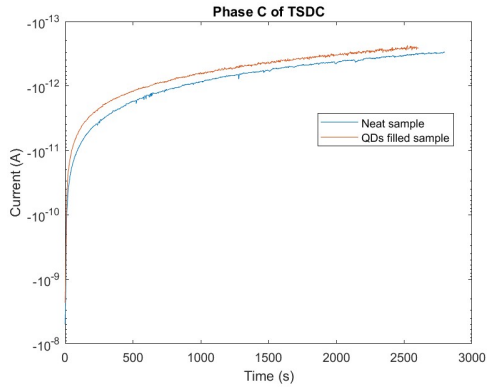

(b) Phase C

Figure 4.8: TSDC, phases B and C

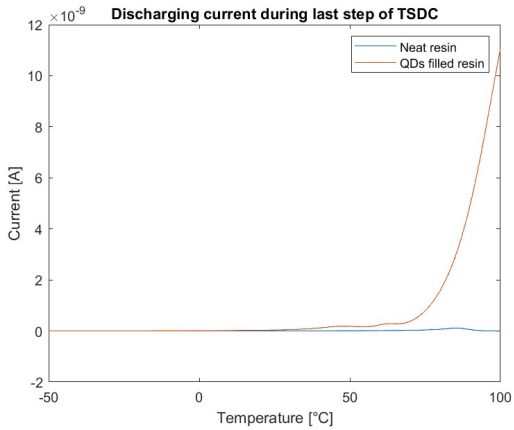

Figure 4.9: Plot of current versus temperature during Phase D of TSDC

by significantly higher current than the neat sample, their respective maxima being 0.11 and 10 nA respectively. Due to the large discrepancy in orders of magnitude, analyzing the respective dynamics solely from the absolute current plot is significantly more challenging. For this reason, and for the typical behaviour of the current during Phase D, it is better to analyze the corresponding Arrhenius plot, reported in Fig. 4.10.

Using Mizutani's theory, exposed in Section 3.2.1.2 it is possible to extract a value for the activation energy of each relaxation process taking place during Phase D. The temperature peak positions and the relaxation energies are reported in Tables 4.4 and 4.5 .

Activation Energy (eV)	γ relaxation	β relaxation	α relaxation	ρ relaxation
Neat sample	0.55	-	0.65	-
0.1% nanocomposite	0.53	-	0.7	1.02

Table 4.4: Relaxation processes activation energies

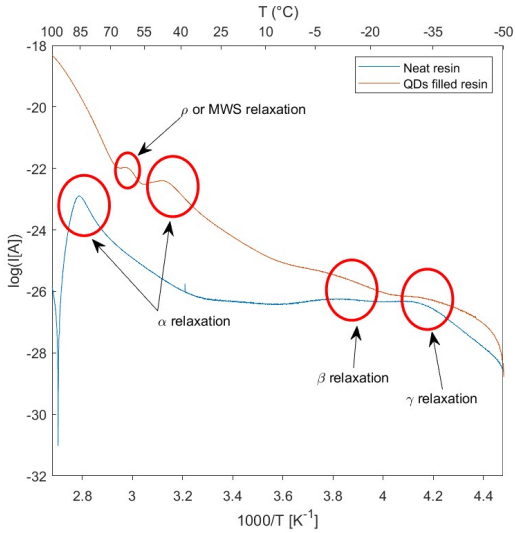

Figure 4.10: Arrhenius plot for Phase D

Temperature (°C)	γ relaxation	β relaxation	α relaxation	ρ relaxation
Neat sample	-30.43	-9.3	86.56	-
0.1% nanocomposite	-30.43	-9.3	48.39	63.55

Table 4.5: Temperature peak positions

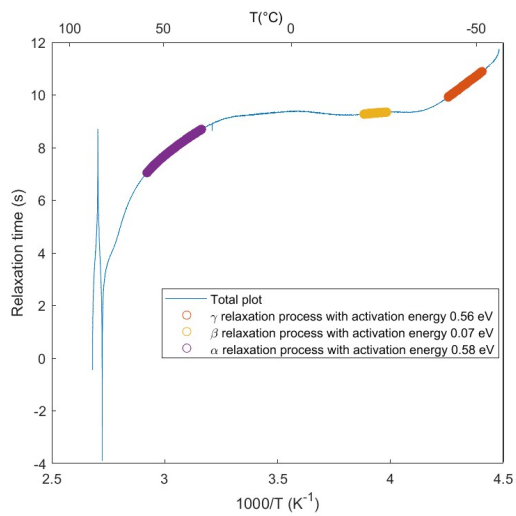

Figure 4.11: BFG plot for neat sample

4.2.2 Analysis with Bucci-Fieschi-Guidi

The results using BFG analysis exposed in Section 3.2.1.4 are here reported. As it can be seen in Figs. 4.11 and 4.12, a similar number of relaxation processes was found. However, some key differences emerge when compared to the results obtained using Mizutani's theory. In particular, different values of activation energies are found, especially for lower temperature relaxation processes. Even though this is a contradiction, it is still an opportunity to evaluate the suitability of these methods. In particular, BFG analysis leads to a more consistent result, at least for the nanocomposite. In fact, if in Mizutani's theory application, β peak could be barely distinguished from other peaks, appearing

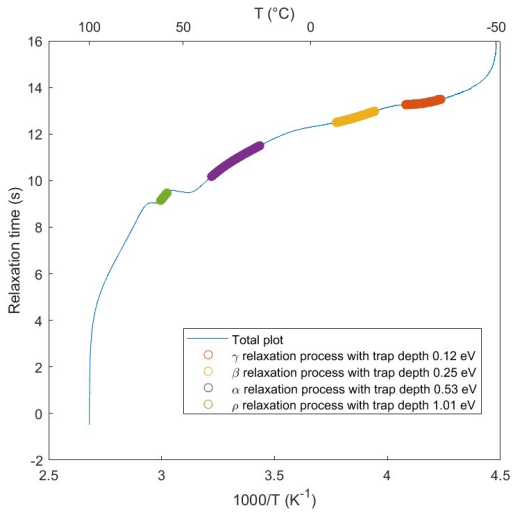

Figure 4.12: BFG plot for nanocomposite

as a shoulder to γ one and thus corresponding to a negligible activation energy, using BFG leads to the presence of 2 lines, one for β, the other for γ relaxation process. Furthermore, as it would be expected, with ascending temperature at which the relaxation process takes place, the corresponding activation energy is higher in a significant way, as shown in Table 4.6. In all the other values, the analyses give similar results.

Activation Energy (eV)	γ relaxation	β relaxation	α relaxation	ρ relaxation
Neat sample	0.58	-	0.59	-
Nanocomposite	0.12	0.25	0.53	1.01

Table 4.6: Relaxation processes activation energies

4.2.3 PEA

4.2.3.1 Neat epoxy

4.2.3.1.1 25°C 20 kV/mm

Under these milder testing conditions, the space charge pattern in Fig. 4.13a reveals the presence of very low heterocharge accumulation, specifically located near the negative electrode. This accumulated heterocharge remains stable throughout the polarization phase, indicating a limited perturbation in the overall charge distribution within the material. The stability of this heterocharge during the polarization phase suggests that the system maintains a low and controlled level of charge accumulation without significant fluctuations. This results in the establishment of a uniform electric field across the material, closely aligning with the average electric field value, as confirmed by the pink curve in Fig. 4.13b. As the material enters the depolarization phase, the accumulated heterocharge is observed to dissipate quickly. The absence of significant space charge retention after the depolarization phase points to a relatively straightforward mechanism of charge storage and dissipation. Fig. 4.13c illustrates this behavior, showing an initial phase characterized by a very

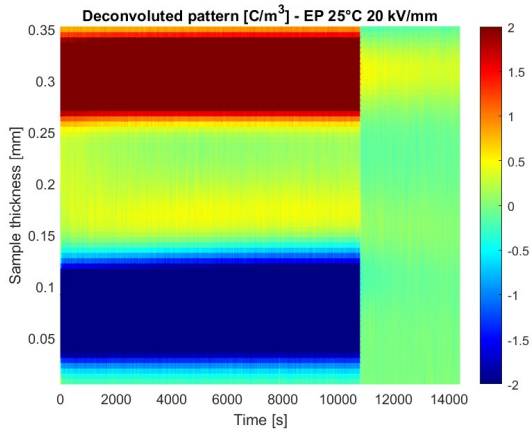

(a) PEA pattern

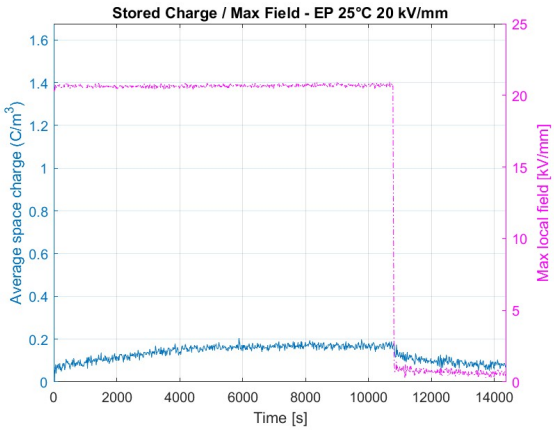

(b) Time evolution of space charge and field

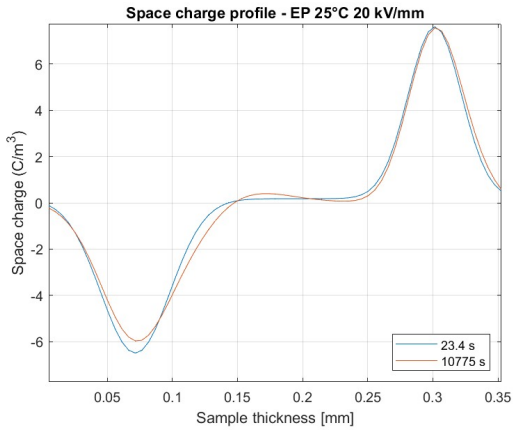

(c) PEA charge profile

Figure 4.13: PEA patterns for neat epoxy at 25°C, 20 kV/mm

weak, linear time evolution of the average space charge. Following this initial phase, the space charge stabilizes at an extremely low value, approximately 0.2 C/m^3. Throughout the voltage-on phase, up until the moment just before voltage-off, the space charge profile remains nearly unchanged. The only notable feature in the profile is the small peak near the negative electrode, confirming the minimal heterocharge accumulation under these conditions.

4.2.3.1.2 25°C 30 kV/mm

At 25°C and an electric field strength of 30 kV/mm, the space charge pattern in Fig. 4.14a indicating a greater sensitivity in heterocharge accumulation compared to the behavior observed at 20 kV/mm, suggesting a heightened sensitivity to the applied electric field. During the polarization phase, the concentration of heterocharge near the negative electrode increases over time. As depolarization phase begins, a rapid decrease in space charge is observed, similar to the behavior seen under the lower field strength. This rapid dissipation of space charge upon removal of the external field suggests a consistent and repeatable charge release mechanism at 25°C. The space charge evolution during the polarization phase is characterized by a linear time evolution of average space charge, as shown in Figure4.14b . For the first two hours, the space charge increases steadily before stabilizing at approximately 0.6 C/m^3. Due to this increased space charge accumulation, the electric field within

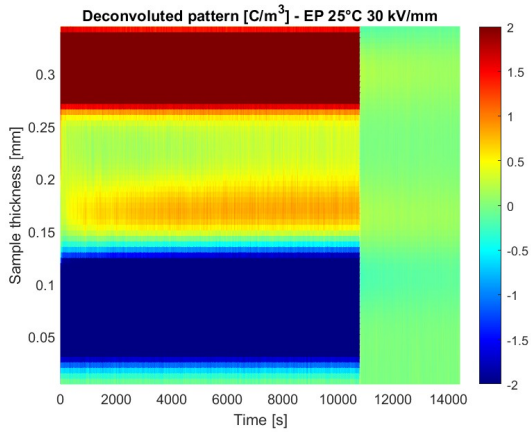

(a) PEA pattern

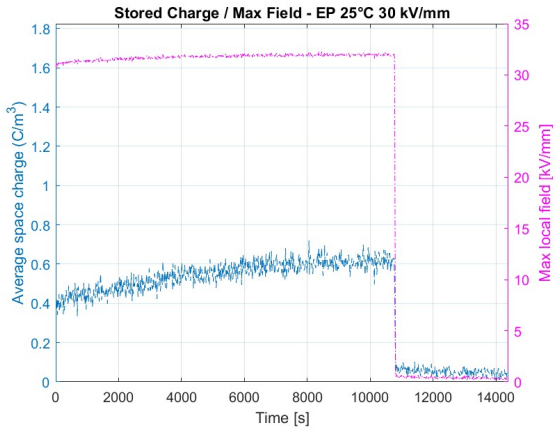

(b) Time evolution of space charge and field

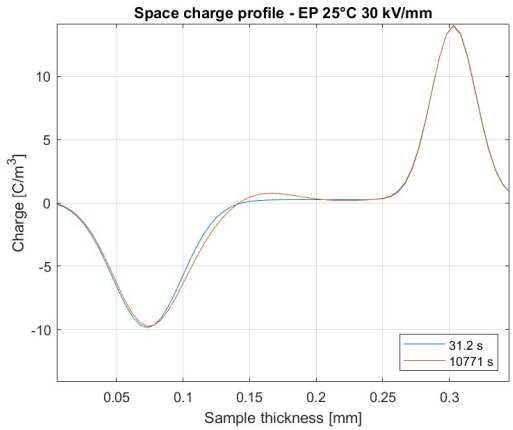

(c) PEA charge profile

Figure 4.14: PEA patterns for neat epoxy at 25°C, 30 kV/mm

the material experiences a non-negligible rise compared to the previous case. The space charge profile in Fig. 4.14c from the beginning of polarization to some seconds before depolarization does not show significant alterations, except for a noticeable peak near the negative electrode.

4.2.3.1.3 40°C 20 kV/mm

The space charge pattern observed at 40°C and 20 kV/mm in Fig. 4.15a exhibits characteristics that align closely with the behavior noted at 25°C and 20 kV/mm. During the polarization phase, heterocharge accumulation near the negative electrode remains low and stable, similar to the observations made in the previous conditions. Only a small intensification is registered in Fig. 4.15b, as the average space charge is slightly higher than 0.2 C/m^3. As the system transitions into the depolarization phase, the heterocharge dissipates rapidly. This rapid dissipation reflects the effective charge release mechanisms that are evident across varying temperatures and electric field strengths. Despite the overall consistency in behavior, a small variation is observed in the time required for space charge to stabilize during the polarization phase. At 40°C, the stabilization of space charge occurs more quickly, requiring only a few hundred seconds to reach a steady state. The space charge profile in Fig. 4.15c is essentially equivalent to the case of 25°C and 20 kV/mm, indicating minimal changes in the overall charge distribution.

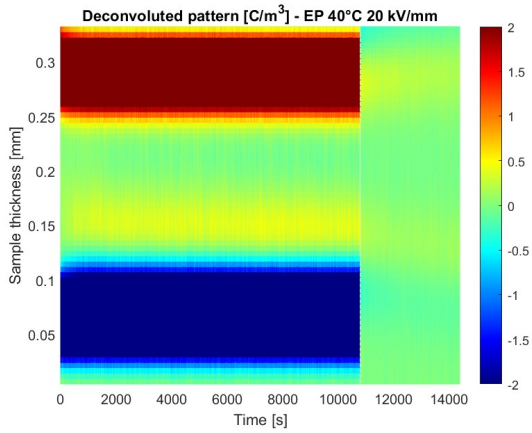

(a) PEA pattern

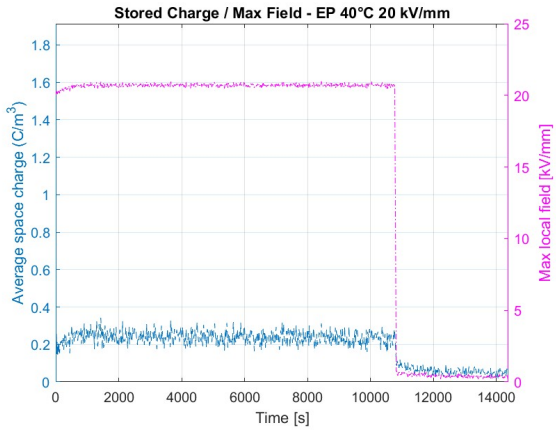

(b) Time evolution of space charge and field

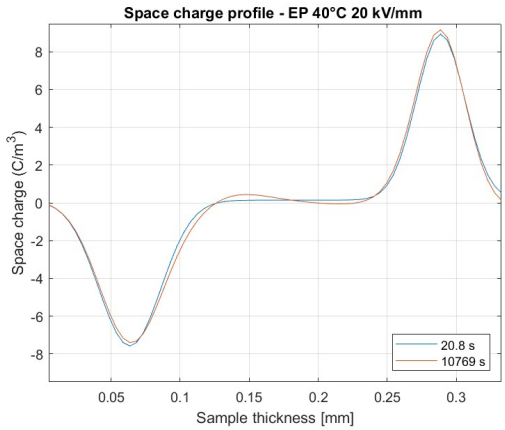

(c) PEA charge profile

Figure 4.15: PEA patterns for neat epoxy at 40°C, 20 kV/mm

4.2.3.1.4 40°C 30 kV/mm

At 40°C and an electric field strength of 30 kV/mm, a notable variation in the space charge pattern in Fig. 4.16a is observed compared to previous conditions. In this scenario, positive charge begins to accumulate along the entire length of the sample, with accumulation occurring near both electrodes. This accumulation of positive charge is characterized by an extremely short time frame, indicating a rapid response to the applied electric field. Once the positive charge begins to accumulate, the average space charge stabilizes at a constant value. Despite this stabilization, the intensity of the average space charge remains extremely limited, suggesting that the accumulation does not significantly influence the maximum electric field within the material. The maximum field in Fig. 4.16b remains close to the applied value of 30 kV/mm, indicating that the charge accumulation is insufficient to cause substantial deviations in the electric field distribution. Additionally, the dissipation of the accumulated charge occurs at a very rapid rate once the external field is removed, mirroring behaviors seen in previous testing conditions. The space charge profile in Fig. 4.16c, from the voltage-on phase to the pre-volt-off phase, remains largely unaltered, reinforcing the notion that while positive charge accumulation does occur, it does not lead to significant changes in the overall charge distribution within the sample.

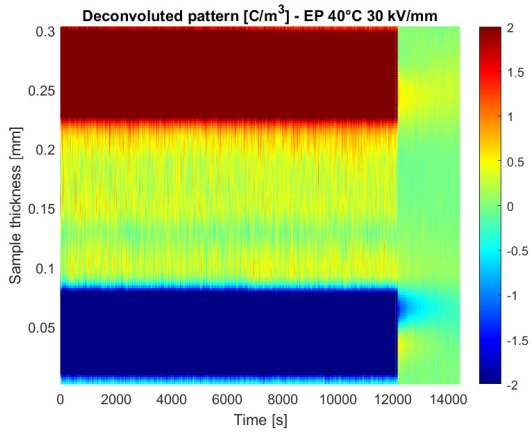

(a) PEA pattern

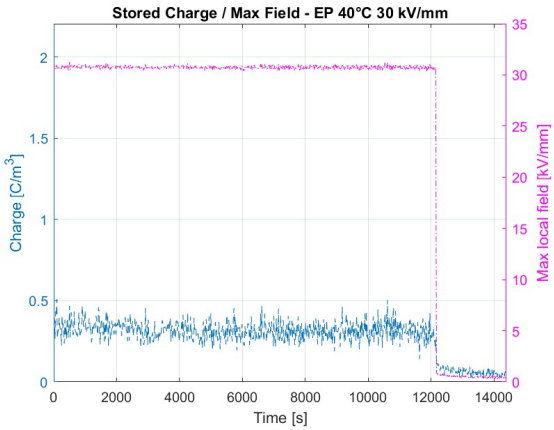

(b) Time evolution of space charge and field

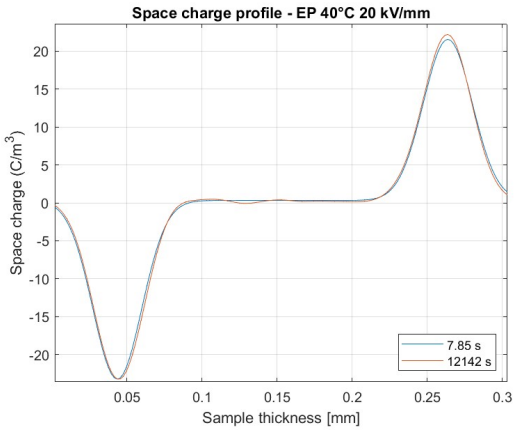

(c) PEA charge profile

Figure 4.16: PEA patterns for neat epoxy at 40°C, 30 kV/mm

4.2.3.1.5 60°C 20 kV/mm

At a temperature of 60°C and an electric field strength of 20 kV/mm, the space charge behavior exhibits the pattern in Fig. 4.17a that is somewhat analogous to that observed at 25°C and 30 kV/mm. Notably, there is a slight increase in heterocharge accumulation near the negative electrode during the polarization phase. The accumulation of charge shown in Fig. 4.17b follows a linear time evolution, indicating a steady increase over time. Unlike previous conditions where a clear stabilization of space charge was observed, no real stabilization occurs in this scenario. The linear time evolution persists throughout the entire three-hour polarization process, suggesting that charge accumulation continues to increase without reaching an equilibrium state. This behavior is also reflected in the dynamics of the maximum electric field, which continues to evolve over time as charge accumulates. In contrast to the behaviors noted in previous conditions, the charge appears to be retained during the depolarization phase at this higher temperature, although it maintains a very low average intensity. The space charge profile in Fig. 4.17c during this phase is characterized by a positive peak located near the negative electrode, further highlighting the increased heterocharge accumulation.

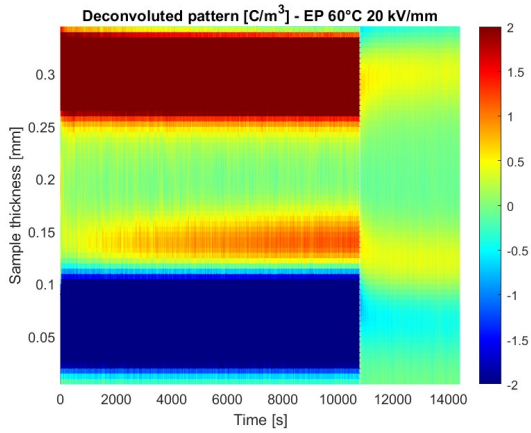

(a) PEA pattern

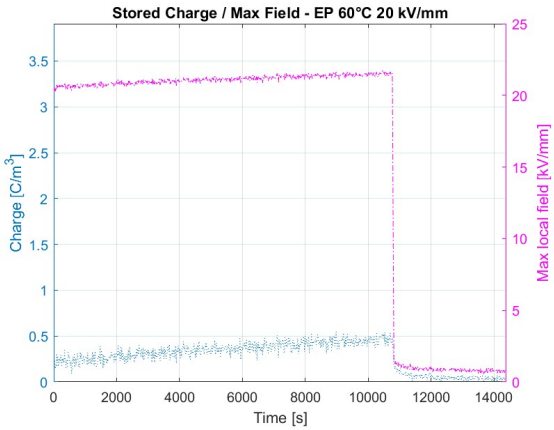

(b) Time evolution of space charge and field

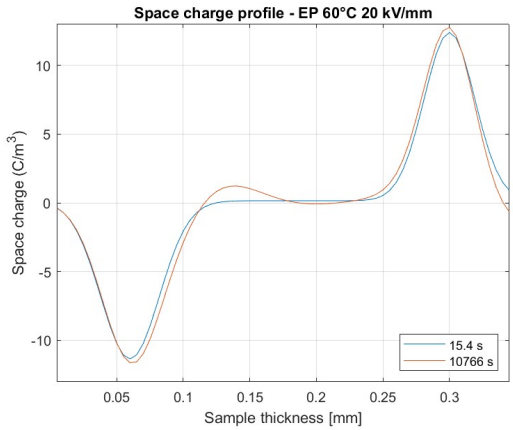

(c) PEA charge profile

Figure 4.17: PEA patterns for neat epoxy at 60°C, 20 kV/mm

4.2.3.1.6 60°C 30 kV/mm

Under the testing conditions of 60°C and an electric field strength of 30 kV/mm, as shown in Fig. 4.18a a more significant accumulation of space charge is observed during the polarization phase compared to all previous cases. During this phase, the predominant charge type is heterocharge, which accumulates near the negative electrode. In addition to the heterocharge, a small amount of homocharge is also present near the positive electrode. The linear time evolution of space charge is particularly prominent under these conditions, as shown in Fig. 4.18b. The accumulation of charge steadily increases over time, reaching a value of approximately 0.8 C/m^3 at equilibrium just a few hundred seconds before the voltage is removed. Persistence of space charge is registered during the subsequent depolarization phase. Despite the increased accumulation in polarization phase, the average space charge intensity remains extremely low. The heterocharge peak is clearly visible in the space charge profile in Fig, 4.18c.

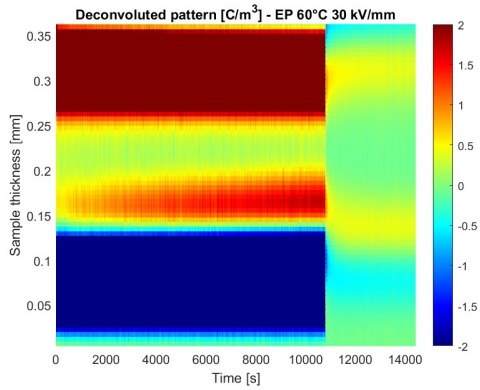

(a) PEA pattern

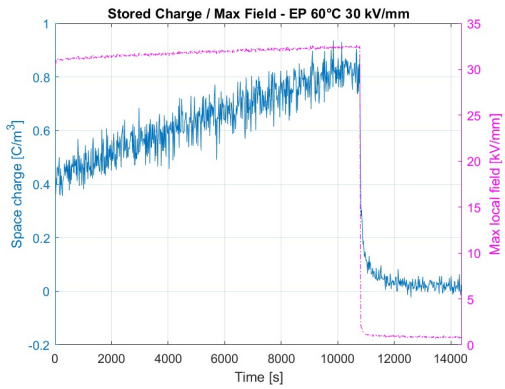

(b) Time evolution of space charge and field

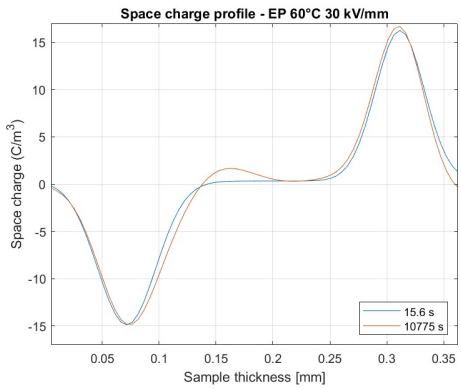

(c) PEA charge profile

Figure 4.18: PEA patterns for neat epoxy at 60°C, 30 kV/mm

4.2.3.2 0.04 % QDs filled nanocomposite

4.2.3.2.1 25°C 20 kV/mm

As shown in Fig. 4.19a, under the testing condition of 25°C and an electric field strength of 20 kV/mm, the 0.04% nanocomposite exhibits strong heterocharge accumulation near both the positive and negative electrodes during the polarization phase. This accumulation is characterized by significant increases in charge density, resulting in a pronounced alteration in the charge distribution within the material. The behavior of the space charge during this phase is particularly interesting, as the positive heterocharge initially increases rapidly in a linear fashion. After reaching a certain point, there is a slight reduction in this accumulation over time, ultimately leading to stabilization before the voltage is removed, as shown in Fig.4.19b. In a similar manner, it is likely that the negative heterocharge also experiences a comparable accumulation pattern; however, this is observed to be less pronounced than that of the positive heterocharge. The space charge profile in Fig. 4.19c during this phase is characterized by the co-presence of two distinct peaks of opposite sign near the electrodes, visually representing the dual nature of the accumulated space charge within the polymeric matrix.

4.2.3.2.2 25°C 30 kV/mm

The behavior of the 0.04% nanocomposite at 25°C and an electric field strength of 30 kV/mm exhibited in Fig. 4.20a is extremely similar to that observed under the conditions of 25°C and 20 kV/mm;

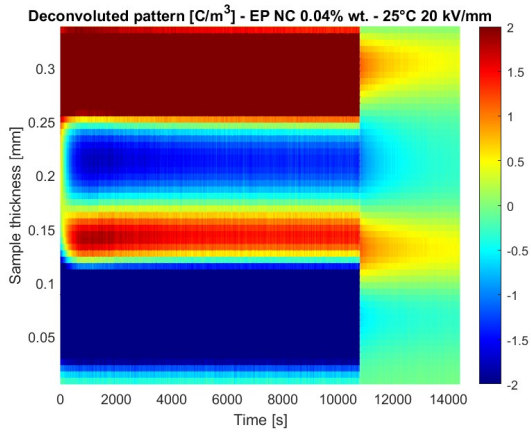

(a) PEA pattern

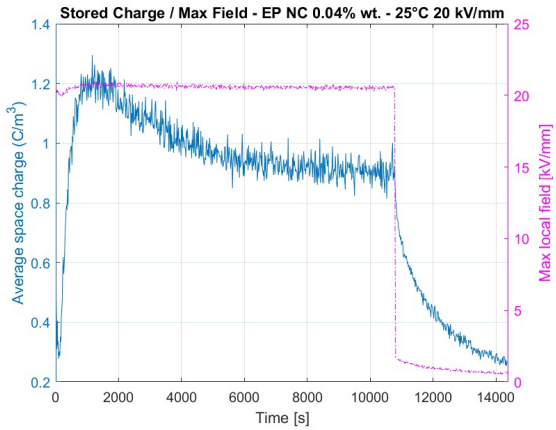

(b) Time evolution of space charge and field

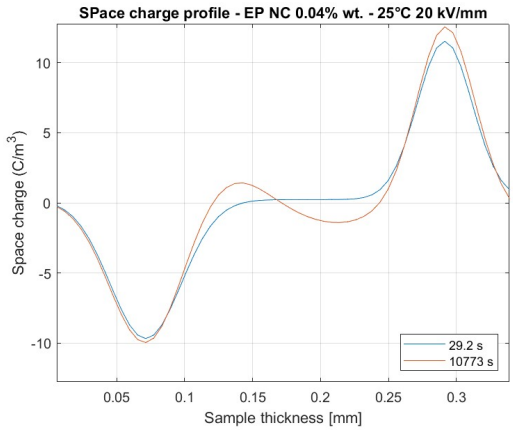

(c) PEA charge profile

Figure 4.19: PEA patterns for 0.04% nanocomposite at 25°C, 20 kV/mm

however, several noteworthy differences can be highlighted. The intensity of the space charge just before volt-off reaches approximately 1.2 C/m^3 in Fig. 4.20b, an increase from the previously recorded value of 0.8 C/m^3. This indicates a greater accumulation of charge under the higher electric field strength.

During the depolarization phase, the dissipation of the accumulated charges reveals slight differences between the positive and negative components. Specifically, the positive charges tend to persist for a slightly longer duration compared to the negative charges, suggesting a subtle variation in the charge release dynamics. This behavior indicates that while both types of charge are subject to dissipation, they do not behave identically throughout the depolarization process. After one hour of depolarization, the retained space charge is noted to be less than that observed in the previous case, with values of 0.2 C/m^3 compared to 0.3 C/m^3.

4.2.3.2.3 40°C 20 kV/mm

Under 40°C and 20 kV/mm, there is a very slight accumulation of heterocharge near the positive electrode, while a much more pronounced accumulation of heterocharge is observed near the negative electrode, as in Fig. 4.21a. The total average space charge during this phase is approximately 0.6 C/m^3 as shown in Fig. 4.21b, indicating a limited overall charge accumulation within the material.

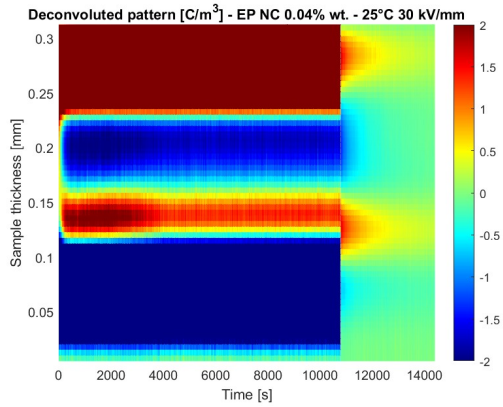

(a) PEA pattern

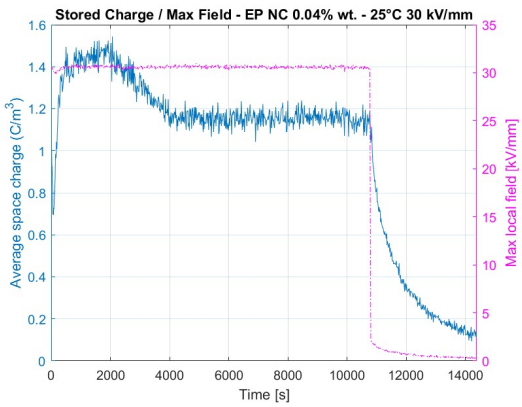

(b) Time evolution of space charge and field

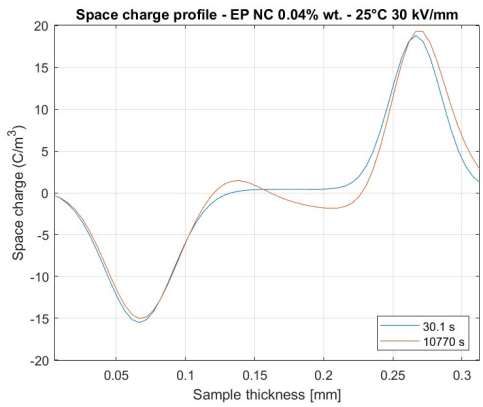

(c) PEA charge profile

Figure 4.20: PEA patterns for 0.04% nanocomposite at 25°C, 30 kV/mm

During the polarization phase, two distinct linear time evolutions of space charge are recorded, each characterized by different slopes; the first evolution exhibits a steeper slope, while the second shows a flatter slope. Notably, this linear evolution persists until just before the voltage is removed. Following the polarization phase, the dissipation of charges occurs at a very rapid rate. The charge profile in Fig. 4.21c reinforces the dual nature of the charge dynamics, with clear demarcation of the regions of heterocharge accumulation near the electrodes.

4.2.3.2.4 40°C 30 kV/mm

Under the conditions of 40°C and an electric field strength of 30 kV/mm, a notable accumulation of heterocharge is observed in Fig. 4.22a near both electrodes from the onset of the polarization phase. This accumulation is characterized by a significant and stable average space charge, maintaining a value around 1 C/m^3 throughout the polarization process as in Fig. 4.22b. The depolarization phase presents a distinctive behavior: immediately following the removal of the voltage, the negative space charge is rapidly dissipated, exhibiting a swift response to the cessation of the applied electric field. In contrast, the positive space charge demonstrates a marked retention, persisting for the entire duration of the one-hour depolarization phase. The space charge profile in Fig. 4.22c further confirms these dynamics, clearly confirming the presence of the two distinct heterocharge layers near the electrodes.

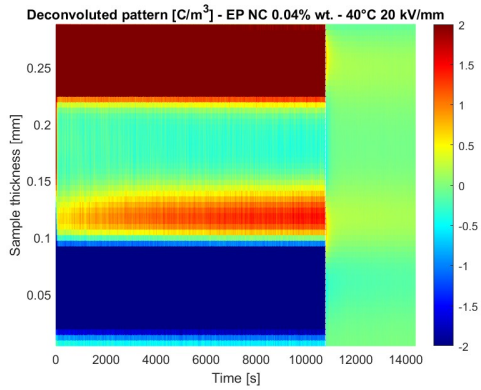

(a) PEA pattern

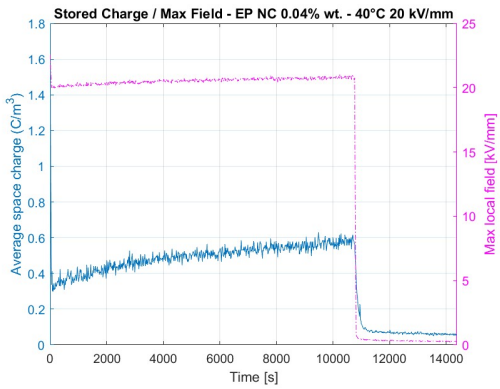

(b) Time evolution of space charge and field

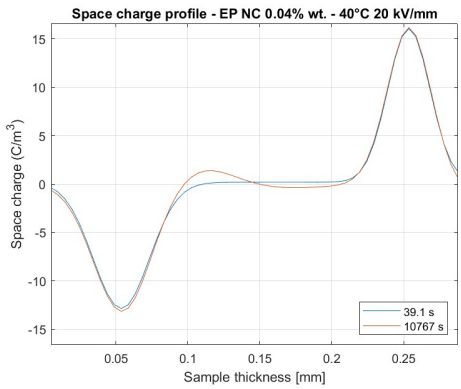

(c) PEA charge profile

Figure 4.21: PEA patterns for 0.04% nanocomposite at 40°C, 20 kV/mm

4.2.3.2.5 60°C 20 kV/mm

Under the testing conditions of 60°C and an electric field strength of 20 kV/mm, the space charge pattern in Fig. 4.23a and profile in Fig. 4.23c reveal the presence of heterocharge at both electrodes, with both regions experiencing a steady increase in charge accumulation over time. This accumulation does not reach equilibrium prior to the removal of the voltage, as shown in Fig. 4.23b, indicating that the charge continues to build up throughout the duration of the polarization phase. The observed trend from the previous case is reaffirmed, with the negative space charge exhibiting rapid dissipation once the voltage is turned off. Conversely, the positive space charge demonstrates a tendency to be retained, persisting even after the cessation of the applied electric field. Additionally, the electric field within the material is observed to intensify over time, reflecting the ongoing dynamics of charge accumulation during the polarization phase.

4.2.3.2.6 60°C 30 kV/mm

Under the conditions of 60°C and an electric field strength of 30 kV/mm, the space charge pattern in Fig. 4.24a and profile in Fig. 4.24c indicates the presence of heterocharge at both electrodes, with the intensities at the positive and negative electrodes being nearly equal. During the polarization phase, the accumulation of negative heterocharge initially shows a slight decrease over time but then stabilizes, maintaining a steady charge distribution. The positive heterocharge, meanwhile, remains

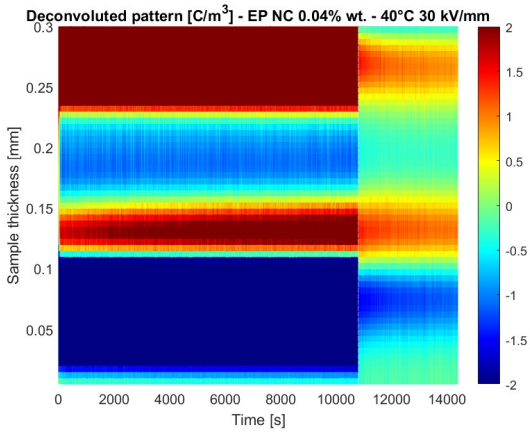

(a) PEA pattern

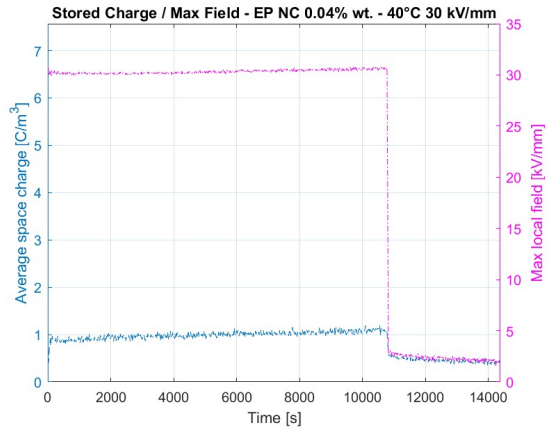

(b) Time evolution of space charge and field

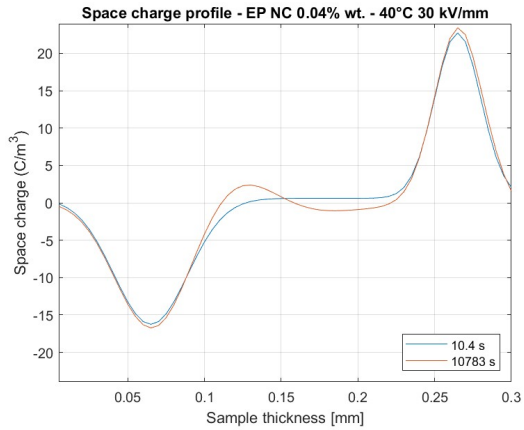

(c) PEA charge profile

Figure 4.22: PEA patterns for 0.04% nanocomposite at 40°C, 30 kV/mm

relatively constant throughout the polarization period.

The most notable observation occurs during the depolarization phase, where the time evolution of the space charge reveals a significant phenomenon: the space charge remains stored within the material, showing no substantial dissipation over time. This retention of charge leads to a persistent and non-negligible electric field, measured at approximately 5 kV/mm in Fig. 4.24b, which remains stable throughout the depolarization phase. The behavior of the material in this phase closely resembles that of an electret, with the space charge remaining unaltered and contributing to the sustained electric field within the polymeric structure.

4.2.3.3 0.1 % QDs filled nanocomposite

4.2.3.3.1 25°C 20 kV/mm

At 25°C and an electric field strength of 20 kV/mm, the average space charge in Fig. 4.25b shows a rapid increase, quickly reaching a stabilizing value of approximately 0.9 C/m^3 during the polarization phase. The space charge pattern in Fig. 4.25a and profile in Fig. 4.25b reveal that the penetration of negative space charge is distributed fairly evenly throughout the sample. However, in general, charge accumulation is higher near the positive electrode. Despite the relatively uniform distribution

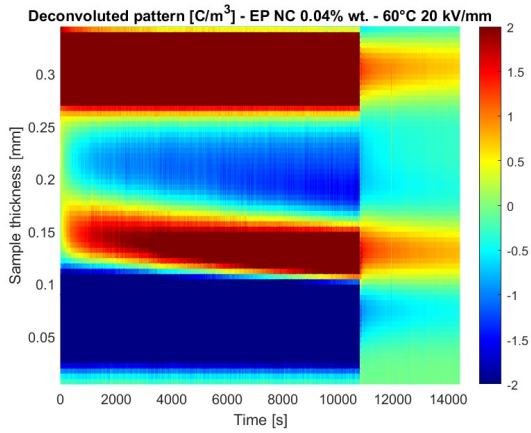

(a) PEA pattern

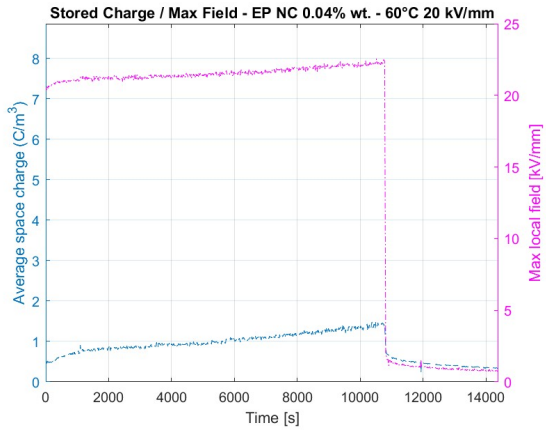

(b) Time evolution of space charge and field

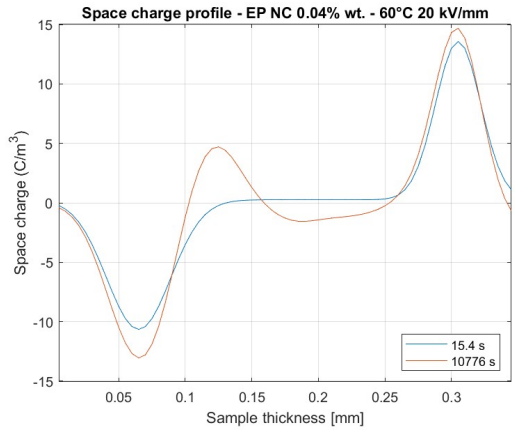

(c) PEA charge profile

Figure 4.23: PEA patterns for 0.04% nanocomposite at 60°C, 20 kV/mm

of the space charge, it persists within the material longer than observed in the neat epoxy sample. Nevertheless, during the depolarization phase, the space charge dissipates rapidly, showing a swift reduction in charge levels once the external electric field is removed. This is different from the behaviour of neat epoxy, which dissipated immediately, and the other nanocomposite, which retained space charge for almost an hour.

4.2.3.3.2 25°C 30 kV/mm

At 25°C and an electric field strength of 30 kV/mm, the space charge behavior during the polarization phase in Fig. 4.26a and Fig. 4.26c shows similarities to previous cases, with negative charge distributed across the entire sample. However, the time evolution of the space charge in Fig. 4.26b differs slightly. Initially, the average space charge begins at approximately 1.1 C/m^3, and it gradually decreases over time, reaching a value of around 0.8 C/m^3 just before the voltage is turned off, at which point a steady state is achieved. This reduction in the space charge appears to be driven by a decrease in the negative space charge near the negative electrode. During the depolarization phase, the space charge demonstrates persistence over time, indicating that it is not fully dissipated immediately after the voltage is removed. However, an asymmetric behavior becomes evident: a significant reduction in space charge is observed near the negative electrode, while a strong localized

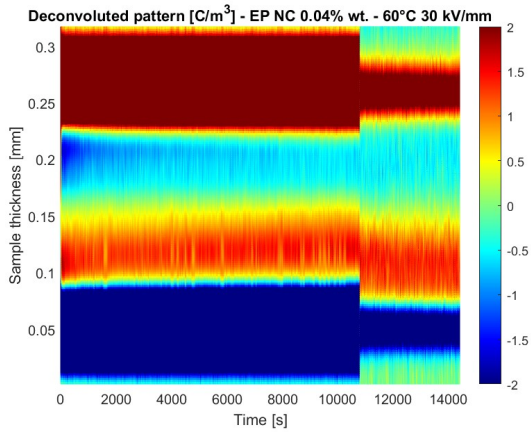

(a) PEA pattern

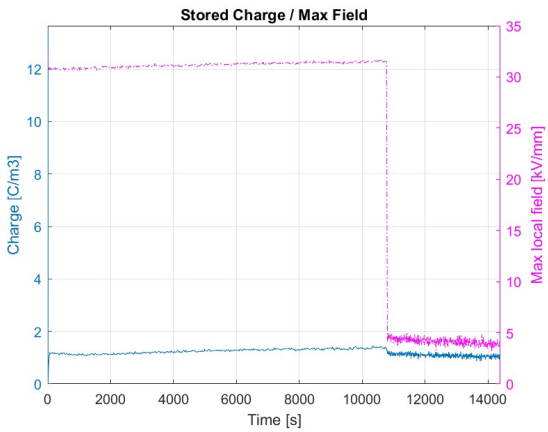

(b) Time evolution of space charge and field

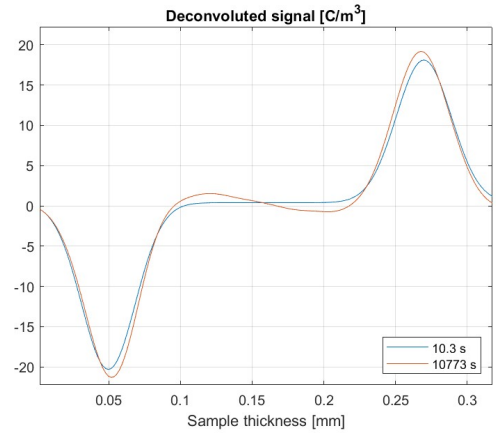

(c) PEA charge profile

Figure 4.24: PEA patterns for 0.04% nanocomposite at 60°C, 30 kV/mm

retention of space charge persists close to the positive electrode.

4.2.3.3.3 40°C 20 kV/mm

Under 40°C and 20 kV/mm conditions, heterocharge accumulation is primarily observed near the positive electrode in Fig. 4.27a, but its intensity is extremely lower than in previous cases. This accumulation gradually diffuses throughout the sample over time, as indicated by the space charge profile. The process of charge diffusion is continuous, with a linear time evolution that eventually stabilizes at an average space charge value of approximately 0.9 C/m^3. During the depolarization phase, the intensity of the accumulated charge decreases, though the space charge persists in a non-negligible manner. This residual charge contributes to the generation of a local maximum electric field of around 3 kV/mm in Fig. 4.27b during the depolarization phase. The space charge profile in Fig. 4.27c and the behavior of the electric field highlight the ongoing influence of the retained charge, even after the external voltage is removed.

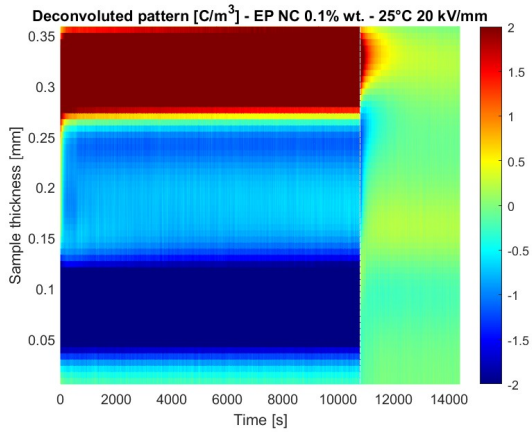

(a) PEA pattern

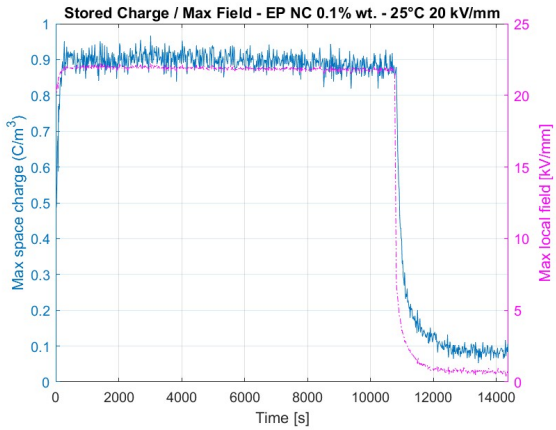

(b) Time evolution of space charge and field

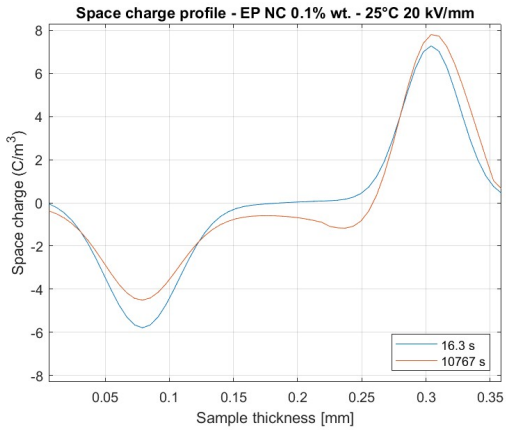

(c) PEA charge profile

Figure 4.25: PEA patterns for 0.1% nanocomposite at 25°C, 20 kV/mm

4.2.3.3.4 40°C 30 kV/mm

At 40°C and 30 kV/mm, the nanocomposite exhibits an extremely rapid and substantial increase in positive space charge accumulation, as shown in Fig. 4.28a. Within a few hundred seconds, the average space charge in the material reaches approximately 3.5 C/m^3, distributed widely across the entire sample. After this peak, a gradual decrease in the average space charge occurs, similar to other observed conditions for this nanocomposite. As also suggested by the space charge profile in Fig. 4.28c, the average charge decreases over time and stabilizes at around 2.8 C/m^3 before the voltage is turned off. During the polarization phase, the maximum local electric field in Fig. 4.28b deviates significantly from the applied field, reaching values as high as 35 kV/mm. In the depolarization phase, there is an initial period in which the positive space charge near the negative electrode is strongly retained. However, following this short retention phase, most of the accumulated space charge dissipates, resulting in an average space charge value of 0.5 C/m^3. Despite the dissipation, the residual charge continues to generate a localized electric field of around 3 kV/mm.

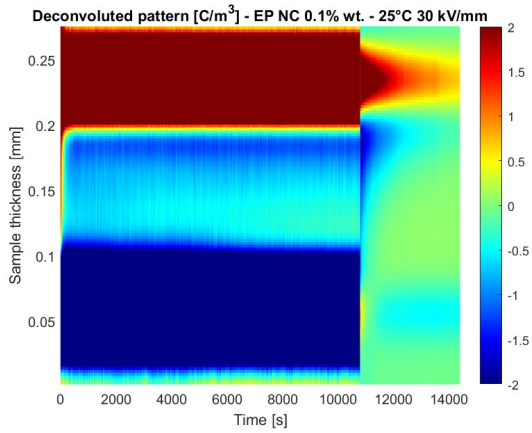

(a) PEA pattern

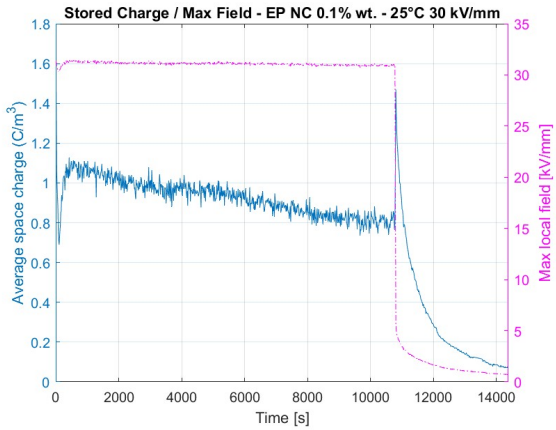

(b) Time evolution of space charge and field

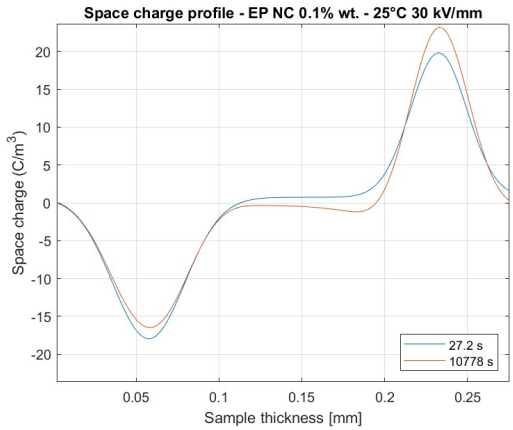

(c) PEA charge profile

Figure 4.26: PEA patterns for 0.1% nanocomposite at 25°C, 30 kV/mm

4.2.3.3.5 60°C 20 kV/mm

A strong heterocharge accumulation occurs almost immediately at the negative electrode as plotted in Fig. 4.29a, indicating a significant build-up of negative charge carriers. This accumulation is prominent from the very beginning and persists throughout the polarization process. In contrast, at the positive electrode, a small amount of heterocharge appears quite suddenly, but unlike the negative side, it gradually intensifies over time, leading to a continuous increase in the overall space charge density. The accumulation at the positive electrode grows more pronounced as polarization progresses. This results in an overall increase in the average space charge density in Fig. 4.29b, which stabilizes at a steady-state value of approximately 2.6 C/m^3. Notably, the spatial distribution of the positive charge, as shown in the profile in Fig. 4.29c, is much more extensive than that of the negative charge, suggesting a broader charge extension near the positive electrode. Over time, the negative space charge begins to decay, indicating that the trapped charges near the negative electrode are slowly dissipating. However, a small portion of the negative charge remains retained even after an hour, implying some degree of long-term charge trapping at this electrode. On the other hand, the positive space charge, although at a lower intensity compared to its peak during the polarization phase, remains relatively stable and fixed over time.

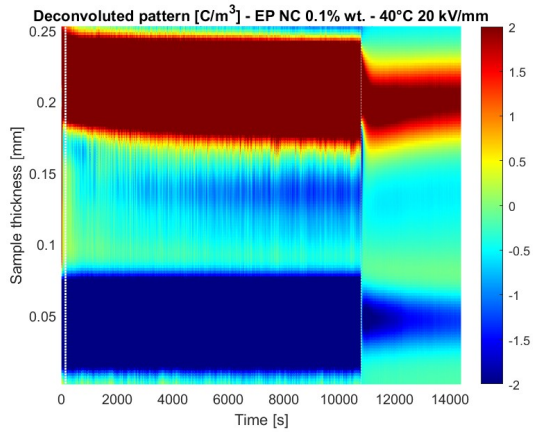

(a) PEA pattern

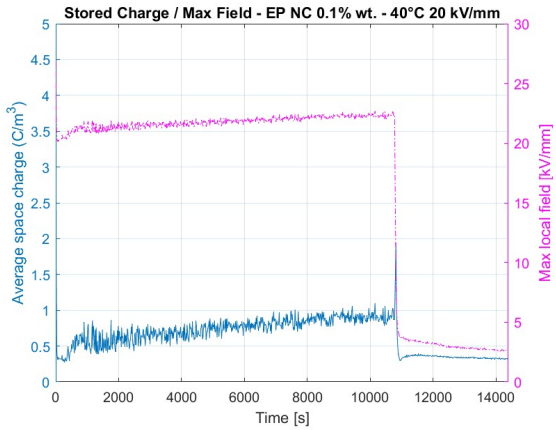

(b) Time evolution of space charge and field

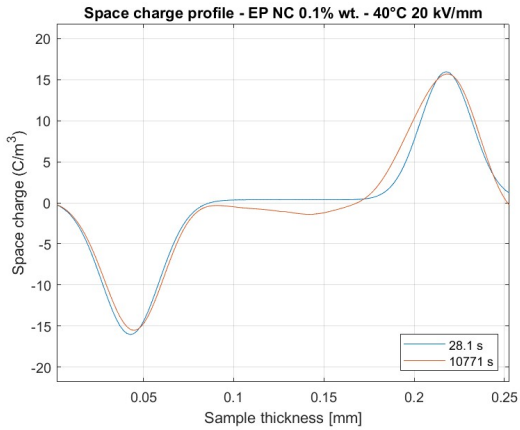

(c) PEA charge profile

Figure 4.27: PEA patterns for 0.1% nanocomposite at 40°C, 20 kV/mm

4.2.3.3.6 60°C 30 kV/mm

The material experienced flashover under these conditions. This occurrance impedes us to find any valuable information regarding space charge behaviour, and suggests this material is not apt for particularly intense operating conditions.

To summarize the obtained results for PEA measurements, the maximum average space charge and field are reported in Tables 4.7 and 4.8.

Conditions	Neat sample	0.04 % NC	0.1 % NC
25°C 20 kV/mm	0.2	1.2	0.9
25°C 30 kV/mm	0.6	1.45	1.1
40°C 20 kV/mm	0.2	0.6	1
40°C 30 kV/mm	0.4	1	3.5
60°C 20 kV/mm	0.5	1.5	2.6
60°C 30 kV/mm	0.8	1.7	-

Table 4.7: Recap table of max average space charge in C/m^3

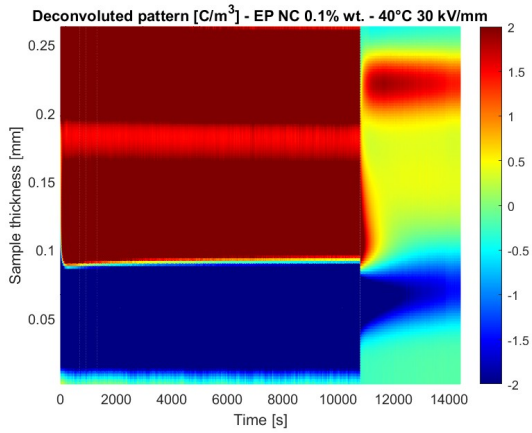

(a) PEA pattern

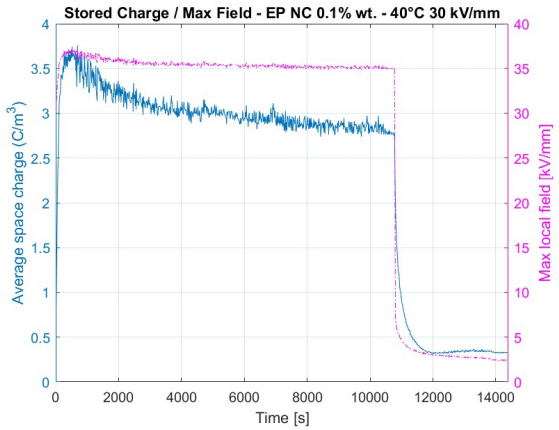

(b) Time evolution of space charge and field

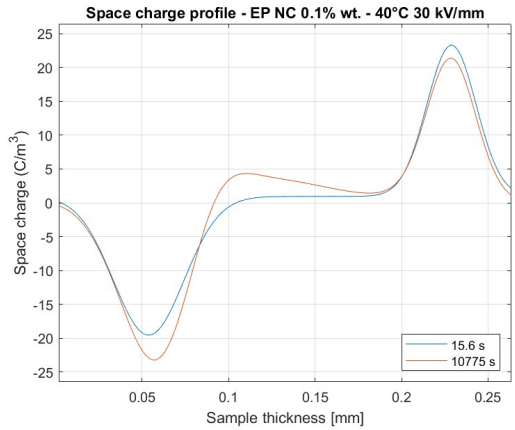

(c) PEA charge profile

Figure 4.28: PEA patterns for 0.1% nanocomposite at 40°C, 30 kV/mm

Conditions	Neat sample	0.04 % NC	0.1 % NC
25°C 20 kV/mm	20.6	20.7	22.0
25°C 30 kV/mm	30.6	30.7	31.0
40°C 20 kV/mm	20.7	20.8	22.6
40°C 30 kV/mm	31.0	30.6	36.8
60°C 20 kV/mm	21.5	22.3	24.5
60°C 30 kV/mm	32.5	31.4	-

Table 4.8: Recap table of max field in kV/mm

4.2.4 Dielectric spectroscopy

4.2.4.1 Complex permittivity

4.2.4.1.1 Neat sample

The neat sample exhibits consistent behavior in the real permittivity spectrum for temperatures below 70°C. In this range, the real permittivity curve in Fig. 4.30a remains largely unaffected, stabilizing at a value around 3.5, which aligns with values commonly reported in the literature.

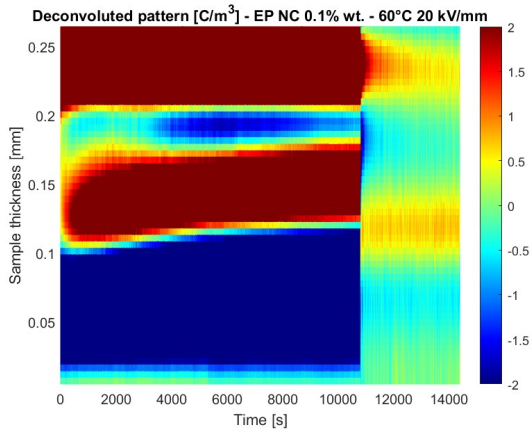

(a) PEA pattern

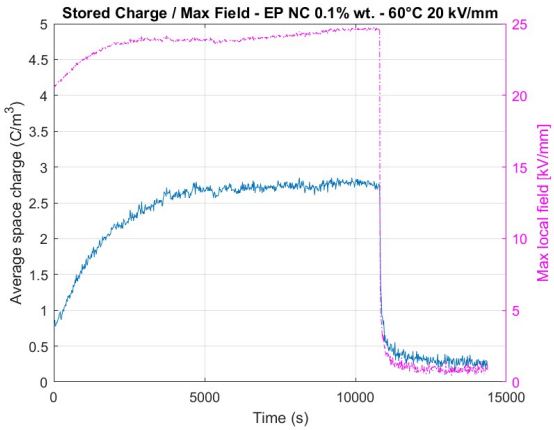

(b) Time evolution of space charge and field

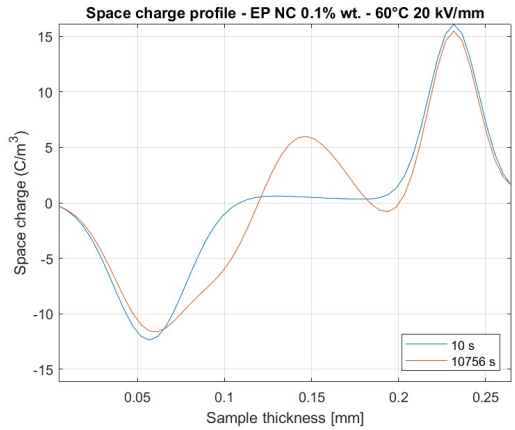

(c) PEA charge profile

Figure 4.29: PEA patterns for 0.1% nanocomposite at 60°C, 20 kV/mm

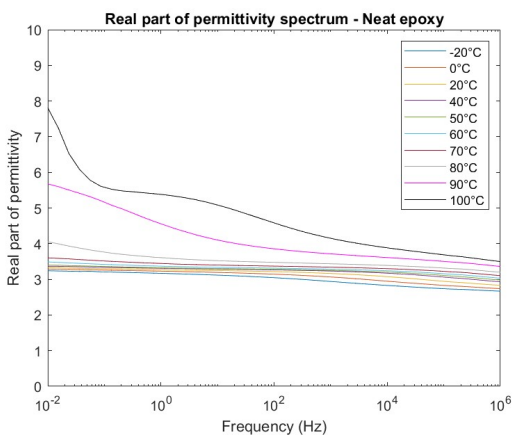

(a) Real permittivity of neat epoxy

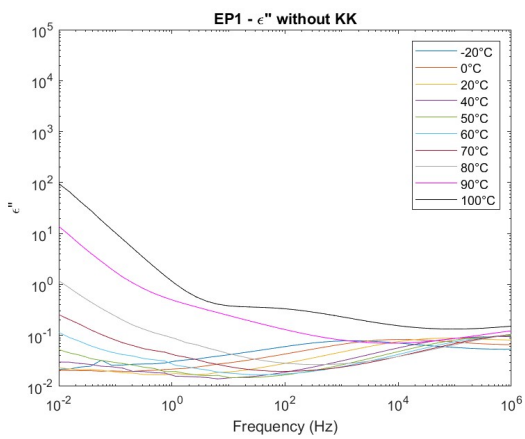

(b) Imaginary permittivity of neat epoxy

Figure 4.30: Complex permittivity of neat epoxy sample: real and imaginary parts

This stability indicates minimal temperature dependence on the dielectric properties of the sample up to this point. However, at 80°C, a slight deviation from this steady trend is observed at low frequencies. This deviation becomes more pronounced as the temperature increases, suggesting a temperature-related impact on the dielectric response at higher temperatures. In the imaginary

permittivity spectrum in Fig. 4.30b, the high-frequency region displays a relaxation process that shifts towards higher frequencies as the temperature increases, up to 50°C. This shift suggests a typical temperature-dependent relaxation mechanism. However, at 60°C, the low-frequency region shows a notable anomaly in the form of an oblique line. This feature is indicative of a significant distortion, widely known in literature as the Quasi-DC conductivity effect [97]. It is a typical low frequency phenomenon that is characterized by a slope quite close to -1 in the logarithmic plot of imaginary part of permittivity versus frequency.

4.2.4.1.2 0.04% nanocomposite

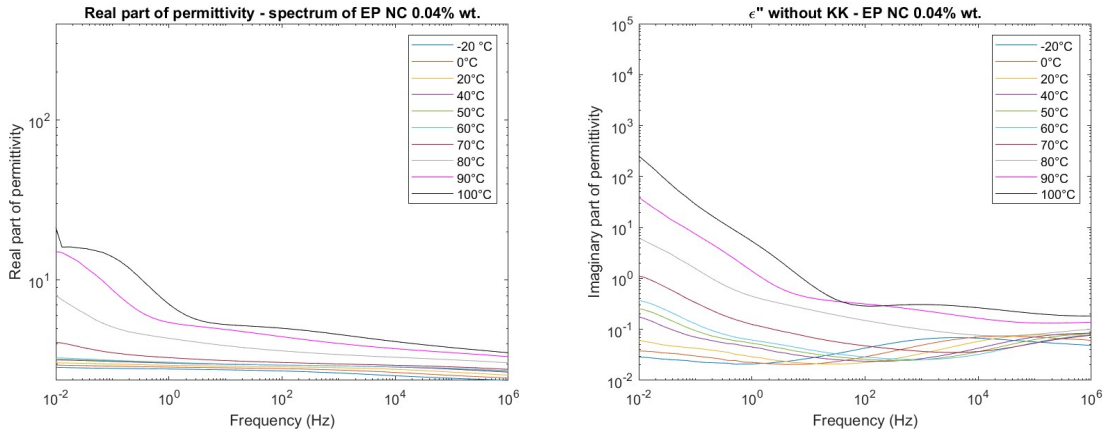

(a) Real permittivity of 0.04% nanocomposite

(b) Imaginary permittivity of 0.04% nanocomposite

Figure 4.31: Complex permittivity of 0.04% nanocomposite: real and imaginary parts

The nanocomposite exhibits real permittivity curves below 70°C in Fig. 4.31a that closely resemble those of the neat sample, maintaining a stable trend throughout this temperature range. However, at 70°C, a small deviation in the real permittivity is observed at low frequencies. This deviation becomes more pronounced at higher temperatures, even more so than in the neat sample, indicating a stronger temperature effect on the nanocomposite's dielectric properties as temperature rises. In the imaginary permittivity spectrum in Fig. 4.31b, the nanocomposite shows a high-frequency relaxation process very similar to that observed in the neat sample, shifting to higher frequencies with increasing temperature. However, at low frequencies, the conductivity-related issues seen in the neat sample are further intensified in the nanocomposite. This increased distortion in the low-frequency region suggests a greater influence of conductivity on the dielectric response of the nanocomposite, especially as the temperature rises.

4.2.4.1.3 0.1% nanocomposite

In the high-frequency region, the relaxation process observed in previous measurements is further confirmed in the nanocomposite sample in Fig. 4.32a. However, strong distortion effects start to emerge in the low-frequency region beginning at 40°C. These distortions indicate increasing strong deviation from true dielectric behaviour, likely due to conductivity effects, as the temperature rises. By 90°C, a second distortion appears in the real permittivity curve, suggesting additional complexities

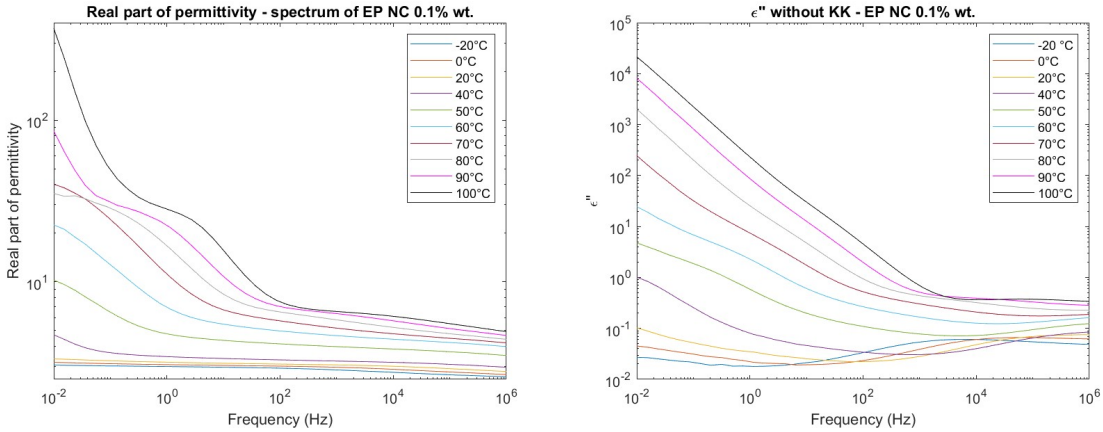

(a) Real permittivity of 0.1% nanocomposite

(b) Imaginary permittivity of 0.1% nanocomposite

Figure 4.32: Complex permittivity of 0.1% nanocomposite: real and imaginary parts

in the material's dielectric response at elevated temperatures. The imaginary permittivity spectrum in Fig. 4.32b is heavily influenced by conductivity effects, with significant distortions becoming evident as early as 50°C. These conductivity-related distortions intensify as the temperature continues to increase, leading to increasingly distorted values in the imaginary permittivity at higher temperatures.

4.2.4.2 Kramers Kronig analysis

In order to partially remove the effect of conductivity on imaginary permittivity and unveil hidden relaxation processes, Eq. 3.16 was applied, and the results plotted in Figs. 4.33, 4.34 and 4.35. They are in the whole characterised by low resolution under high frequency and low temperature conditions, however managing to convey important information regarding the regions in which distortion of imaginary permittivity is significant.

4.2.4.2.1 Neat sample

In Fig. 4.33, at 80°C, a relaxation process starts to appear, whose peak accurate position is not available; it then shifts towards higher frequencies at higher temperatures.

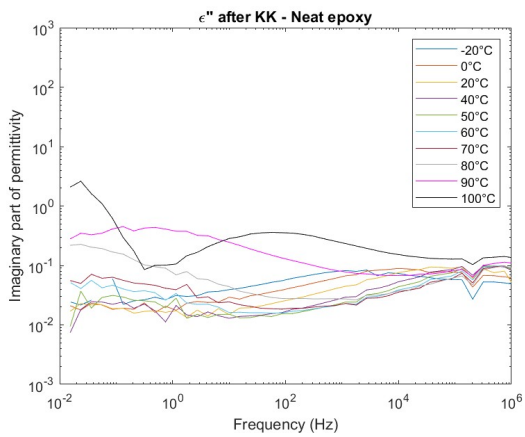

:

Figure 4.33: Imaginary permittivity spectrum of neat epoxy after Kramers Kronig

4.2.4.2.2 0.04% nanocomposite

As shown in Fig. 4.34, the employment of Kramers Kronig expression for imaginary permittivity has a twofold consequence:

- The maximum value of the imaginary permittivity is significantly reduced of at least two orders of magnitude for the highest temperature available
- a previously hidden relaxation process is unravelled which in the analysed range of frequency arises at 80, 90 and 100°C

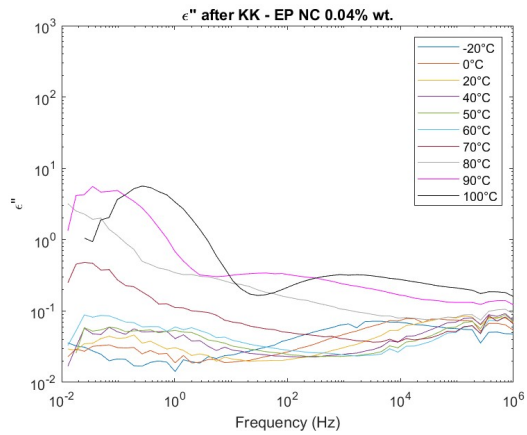

Figure 4.34: Imaginary permittivity spectrum of EP NC 0.04% after Kramers Kronig

4.2.4.2.3 0.1% nanocomposite

At temperatures higher than 40°C, another process exists at low frequencies, as shown in Fig. 4.35. Its shifting towards higher frequencies at higher temperatures is marked, even though at lower temperatures the accurate position of the peak cannot be detected. Furthermore, at 90°C the conduction mechanisms are so high that they start to intervene, disregarding the employment of KK expression, further distorting the plot.

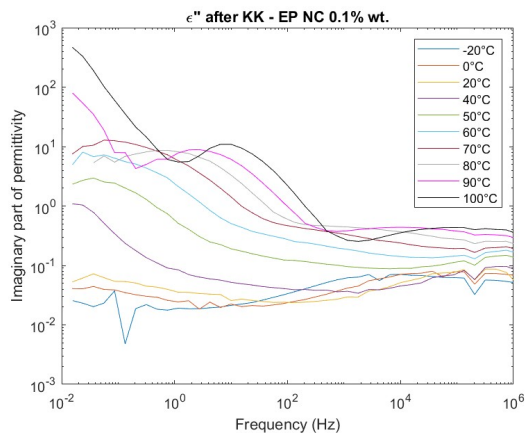

Figure 4.35: Imaginary permittivity spectrum of EP NC 0.1% after Kramers Kronig

4.2.4.3 AC conductivity

An increase in the imaginary permittivity suggests the presence of an additional physical phenomenon that conceals the true relaxation process, complicating its analysis. As this behavior is often attributed to conductivity effects, further analysis using the AC conductivity spectrum can help determine whether conductivity is indeed the primary source of the observed trend.

4.2.4.3.1 Neat sample

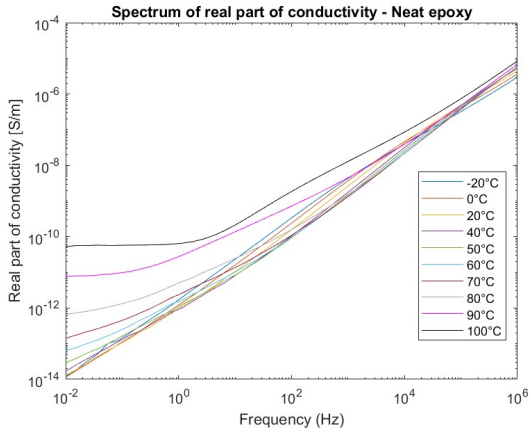

Figure 4.36: AC conductivity spectrum of neat epoxy

This sample, for temperatures lower than 70°C, is characterised by a plot of the real part of the conductivity in Fig.4.36 which unperturbedly increases with frequency. This trend is a good indicator, as it is connected to an insulating nature of the material. Nevertheless, at 80°C the curve starts to bend in a considerable way around 1 Hz, tending towards a Quasi-DC conductivity value which increases with temperature. The plateau values are used to compute the parameters of the QDC model, as in Table 4.9.

4.2.4.3.2 0.04% nanocomposite

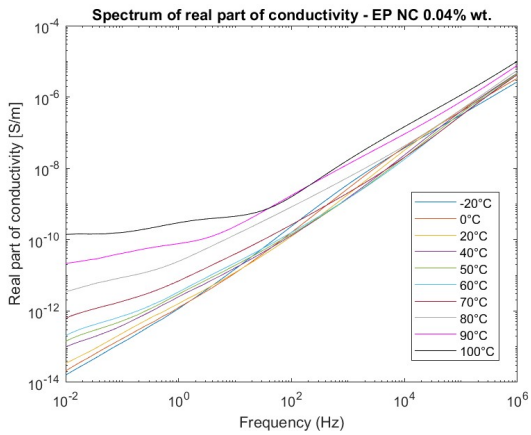

Figure 4.37: AC conductivity spectrum of EP NC 0.04%

The behaviour is similar the one of the neat sample, especially under 20°C. Furthermore, in Fig. 4.37 a not negligible bending of the conductivity already starts at 40°C, suggesting that also at those temperatures a Quasi DC conduction value is almost reached. Moreover, the bending occurs at a higher frequency than in the neat sample, especially at higher temperatures where the bending frequency reaches 10 Hz, and at temperatures higher than 80°C two bendings can be distinguished. The QDC values are higher, especially in correspondance of lower values of temperature. The corresponding parameters highlight a severe reduction in both the pre-exponential factor and in the activation energy.

4.2.4.3.3 0.1% nanocomposite

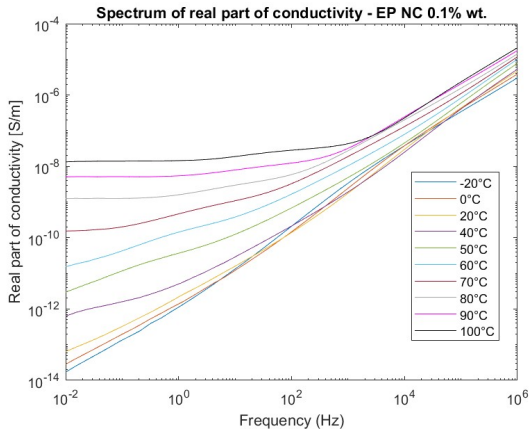

Figure 4.38: AC conductivity spectrum of EP NC 0.1%

In Fig. 4.38, the bending is considerably experienced already at 40°C. This results also at an almost reached stabilization of the AC conduction to the Quasi DC one also at 40°C, a phenomenon not present in other samples. The twofold bending found in the other nanocomposite is confirmed, and the bending occurs at significantly higher frequencies which even reach 1000 Hz at 100°C. This also implies significatly higher values of Quasi DC conductivity for all temperatures. Nevertheless, this higher availability of data lets a better fitting of the experimental parameters, which lead to the following result: a higher content of filler corresponds to a similar pre-exponential factor, but to a not-negligible decrease in the activation energy. A common feature to all materials is the value of conductivity at high frequencies, which is around 10^{-4} S/m.

a and b coefficients	σ_0	E_a (eV)
Neat sample	$2.4 \cdot 10^{19}$	2.19
EP004	$1.4 \cdot 10^{11}$	1.55
EP01	$1.1 \cdot 10^{11}$	1.42

Table 4.9: Quasi DC conduction - Arrhenius parameters

4.2.4.4 Electrical modulus

Analysis of the imaginary permittivity successfully identified a relaxation process, particularly with the aid of Kramers-Kronig analysis. However, a more detailed investigation of these peaks was limited, as they were observed only infrequently, emerging at very high temperatures in the low-frequency region. Therefore, a comprehensive analysis of the imaginary part of the electrical modulus was conducted, as peaks in its spectrum typically appear at higher frequencies compared to those in the imaginary permittivity spectrum, as exposed in Section 3.2.4.1

4.2.4.4.1 Neat sample

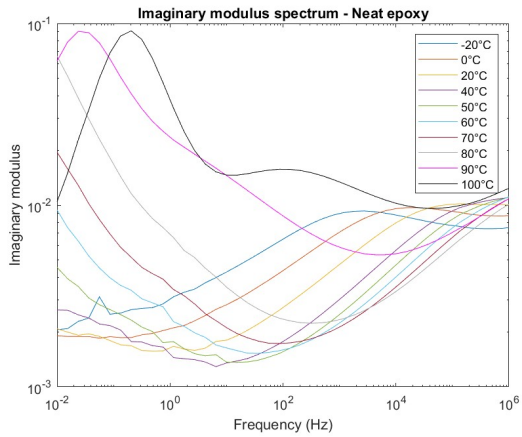

Figure 4.39: Imaginary modulus spectrum of neat epoxy

The electric modulus spectrum in Fig. 4.39 reveals a clear relaxation process at high frequencies. The peak frequencies corresponding to this process are utilized for determining the Arrhenius parameters, as outlined in Table 4.10. This high-frequency relaxation is consistent with observations from the permittivity spectrum and provides insight into the temperature-dependent dielectric behavior of the nanocomposite. At lower frequencies, a distinct relaxation process emerges at elevated temperatures, which was not evident in the complex permittivity spectrum. This observation confirms the effectiveness of the electric modulus approach in identifying relaxation phenomena that might be masked in other types of analysis. However, this lower-frequency relaxation process is only observed at two different temperatures, making it difficult to perform a comprehensive analysis of its associated Arrhenius parameters due to the limited data. Despite this, the identification of this additional relaxation process underscores the importance of electric modulus analysis for capturing subtle dielectric behaviors in the material.

4.2.4.4.2 0.04% nanocomposite

The electric modulus spectrum in Fig. 4.40 further confirms the high-frequency relaxation process, with peak positions similar to those observed in the neat sample. This consistency in the high-frequency region indicates comparable relaxation dynamics between the nanocomposite and neat epoxy. However, in the low-frequency region, the relaxation process in the nanocomposite shifts

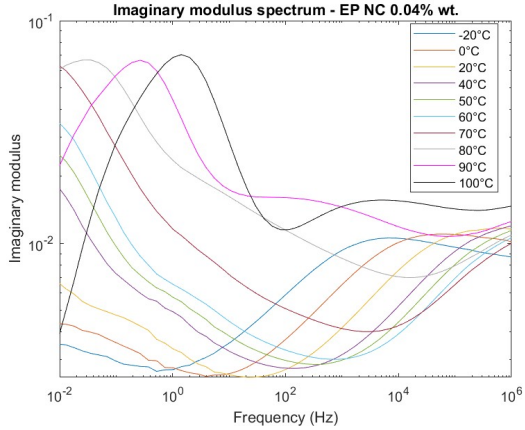

Figure 4.40: Imaginary modulus spectrum of EP NC 0.04%

towards higher frequencies compared to the neat sample. Additionally, a new peak appears at 80°C, allowing for an estimation of the activation energy, which is calculated to be approximately 1.9 eV. In the intermediate-frequency region, a shifting peak is observed at 90°C and 100°C. This feature is particularly noteworthy, as a similar peak was partly present in the 100°C spectrum of the neat epoxy, even though here it is shifted towards higher frequencies.

4.2.4.4.3 0.1% nanocomposite

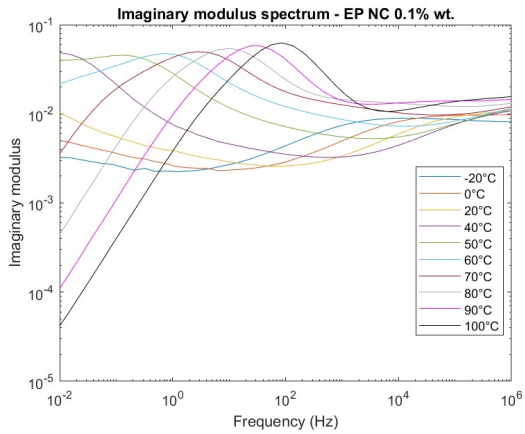

Figure 4.41: Imaginary modulus spectrum of EP NC 0.1%

The modulus spectrum of the 0.1% nanocomposite in Fig. 4.41 displays a rapidly shifting peak in the low-frequency region, which shifts to much higher frequencies compared to other materials. This distinct behavior is used for Arrhenius fitting, where both the pre-exponential factor and activation energy show a notable decrease compared to the other nanocomposites. This reduction indicates a different relaxation dynamic in the material.

At high temperatures, the low-frequency region is characterized by low modulus values, likely influenced by unaddressed conductivity effects that become more pronounced in this region. In the intermediate-frequency region, the shifting peak continues its movement towards higher frequencies, exceeding 10^4 Hz at 90°C.

Sample	$f_0(Hz)$	$E_a(eV)$
HF peak	$3.8 \cdot 10^{32}$	2.03
EP004 (LF)	$9.1 \cdot 10^{25}$	1.91
EP01 (LF)	$1.26 \cdot 10^{21}$	1.46

Table 4.10: Modulus Arrhenius behaviour - parameters

4.2.5 Bulk conductivity

4.2.5.1 Time evolution of DC currents

4.2.5.1.1 Neat epoxy

The behavior of neat epoxy under high electric fields and varying thermal conditions reveals distinct transient dynamics in DC conductivity. When subjected to an electric field of 10 kV/mm at 20°C, the current in Fig. 4.42a initially exhibits a rapid decline, followed by a single steady-state phase. As the temperature increases, the current evolution becomes more complex, displaying two distinct steady-state regions. In this case, the final steady-state current represents the effective long-term conductivity of the material. The time required to reach the first steady-state decreases with increasing temperature, a trend that also applies to the second steady-state for tests conducted at 40°C and 60°C.

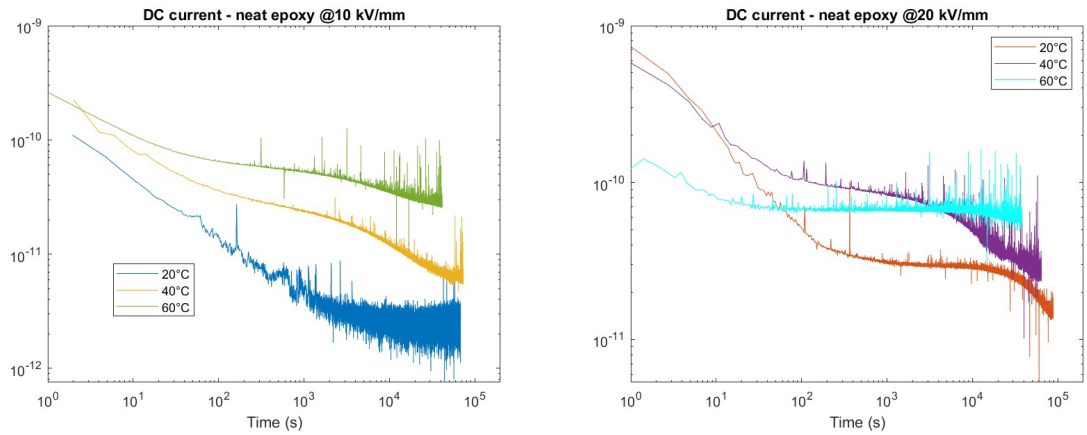

(a) Neat epoxy sample at 10 kV/mm

(b) Neat epoxy sample at 20 kV/mm

Figure 4.42: Transient DC currents for neat epoxy

Additionally, the magnitude of the steady-state current is observed to rise as the temperature increases, suggesting enhanced charge mobility or increased carrier generation under thermal excitation. When the electric field is increased to 20 kV/mm, the DC conductivity transients at 20°C and 40°C in Fig. 4.42b exhibit a two-stage steady-state process. The time required to reach both steady states decreases with increasing temperature, reflecting similar thermal dynamics. The 60°C test instead reveals an almost unaltered conduction current trend right after 100 seconds.

4.2.5.1.2 0.04% nanocomposite

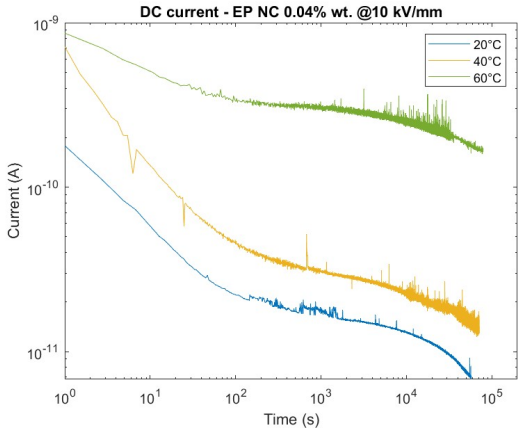

(a) 0.04% nanocomposite at 10 kV/mm

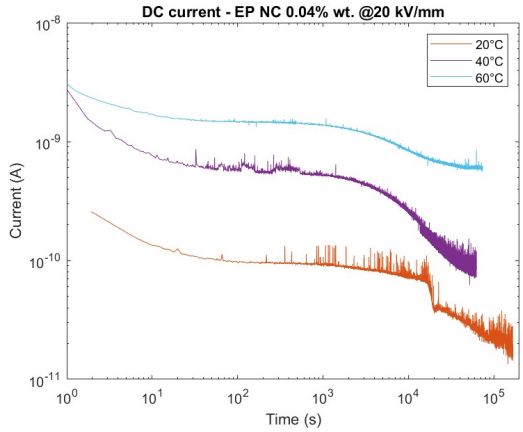

(b) 0.04% nanocomposite at 20 kV/mm

Figure 4.43: Transient DC currents for 0.04% nanocomposite

The DC conductivity transients of neat epoxy under an electric field of 10 kV/mm in Fig. 4.43a display a characteristic two-step steady-state process across all tested temperatures. At 20°C and 40°C, the shape of the transient curves is nearly identical, although the final steady-state current values differ significantly. In contrast, at 60°C, the increase in current is more pronounced, and the system reaches the first steady-state much faster—within 100 seconds, which is considerably quicker than at the lower temperatures. Under an electric field of 20 kV/mm, the 20°C test in Fig. 4.43b exhibits a distinct step-like transition between the two steady states, a feature not observed at other temperatures or at lower field strengths. The time required to reach the first steady-state is consistent across different temperatures and materials, but the time to achieve the final equilibrium decreases with increasing temperature. Moreover, the overall time to reach equilibrium is shorter at 20 kV/mm compared to the 10 kV/mm condition, highlighting the effect of higher field strength on speeding up the conductivity dynamics.

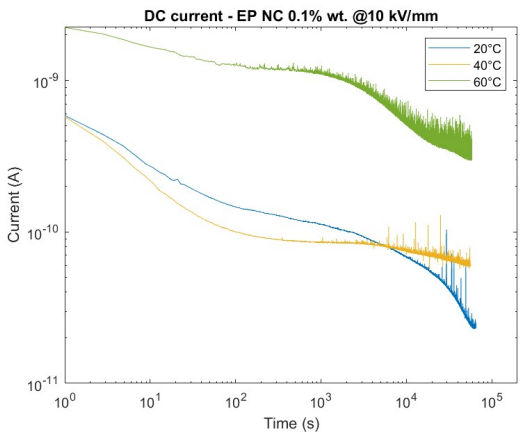

(a) 0.1% nanocomposite at 10 kV/mm

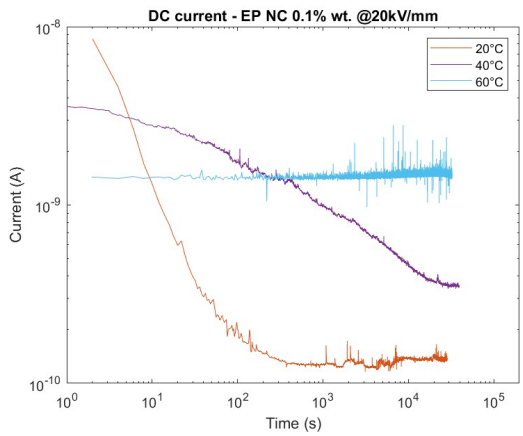

(b) 0.1% nanocomposite at 20 kV/mm

Figure 4.44: Transient DC currents for 0.1% nanocomposite

The DC conductivity transient of a 0.1% nanocomposite under an electric field of 10 kV/mm in Fig. 4.44a reveals a consistent two-step steady-state process at all tested temperatures. The first steady-state is reached in a similar time across different temperatures, while the time required to attain the second steady-state decreases as the temperature increases. At 20 kV/mm, the material exhibits an anomalous behavior, as shown in Fig. 4.44b. At 20°C, the nanocomposite reaches the steady-state almost immediately, skipping the typical twofold process seen at lower field strengths. No second steady-state phase is observed in this case, suggesting that at this temperature and field strength, the conductivity quickly stabilizes. At 40°C, the system behaves differently; the material appears to reach only a single steady-state after approximately 10,000 seconds. Finally, at 60°C, the nanocomposite again reaches a steady-state almost instantaneously.

4.2.5.2 Steady state conductivity values

Fig. 4.45 reports the steady-state values of DC conductivity for all the samples under all the conditions. The trend is clearly growing with nanofiller content. In general, higher temperatures and/or electric fields imply a higher value of the conductivity, as expected from a nonlinear typical behaviour of polymeric materials.

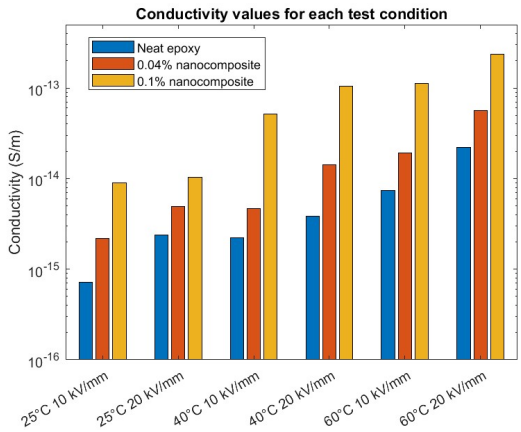

Figure 4.45: Steady-state conductivities

The table 4.11 contains the coefficients arising from the multilinear regression of steady-state conductivity values with respect to T and E. The pre-exponential factor has decreased from the neat sample to the 0.04% nanocomposite, and then increases with the 0.1% nanocomposite. The dependence upon electric field of the conductivity seems to follow a monotonous behaviour with filler content, whereas the a coefficient, while being lower for the neat sample, is significantly higher in the 0.04% nanocomposite as opposed to the 0.1% one. The fitting plots are represented in Figs. 4.46a- 4.46c.

4.2.5.3 Transient behaviour

The Q and α parameters arising in Curie-Von Schweidler theory exposed in Section 3.2.5.1.1 were also extracted from regression of the experimental values with equation 3.19, here reported:

Empirical coefficients	σ_0 (S/m)	a (1/K)	b (mm/kV)
Neat sample	$1.1 \cdot 10^{-16}$	0.056	0.072
EP004	$7.6 \cdot 10^{-17}$	0.093	0.079
EP01	$4.53 \cdot 10^{-16}$	0.073	0.098

Table 4.11: Coefficients coming from empirical fitting of conductivity

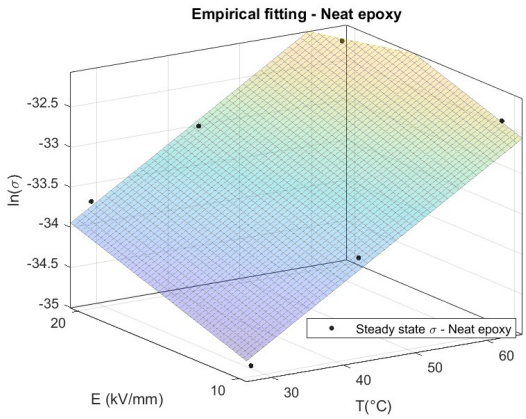

(a) Neat epoxy sample

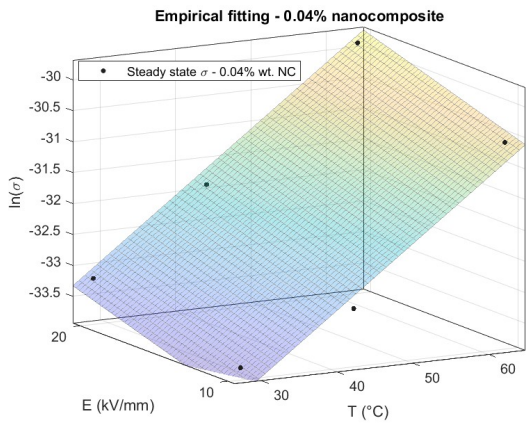

(b) Time evolution of space charge and field

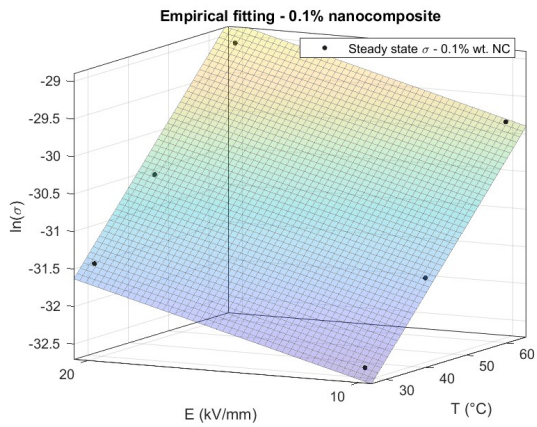

(c) PEA charge profile

Figure 4.46: 3D fittings of experimental data according to empirical model

$$I = \frac{VQ}{\Gamma(1+\alpha)} t^{-\alpha} + V/R_P \tag{4.1}$$

This analysis aims to determine whether the parameters Q and α, which are only partially explored in theoretical literature, can provide insights into the physical phenomena occurring in dielectrics by examining their trends with respect to temperature and applied electrical stress. If successful, this approach could demonstrate that valuable information can be derived from the initial moments (within a few seconds) of the polarization phase in conductivity measurements. Their trend with voltage is reported in Figs. 4.47a and 4.47b and is discussed in the following paragraphs.

For the neat epoxy sample, α shows a clear decrease with increasing electric field, which suggests that the material moves further away from ideal capacitive behavior as the electric field

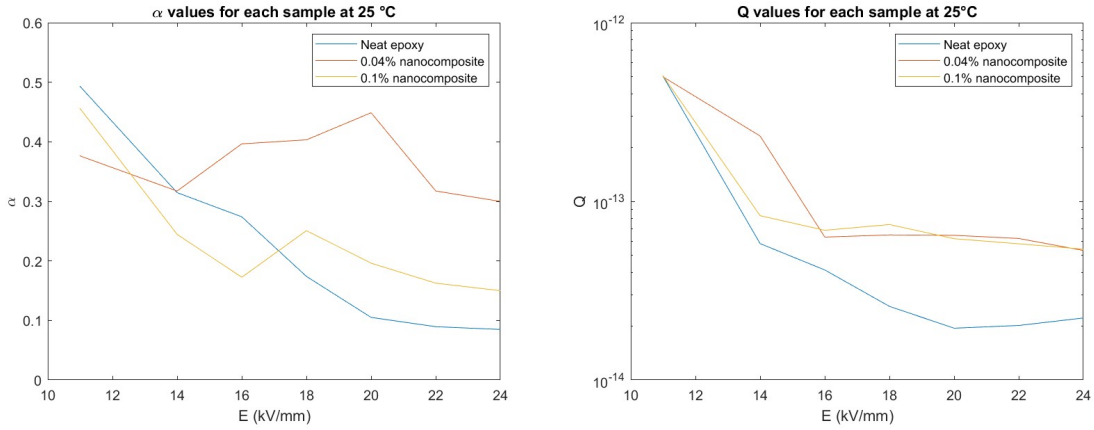

(a) α parameter

(b) Q parameter

Figure 4.47: α and Q parameters - Trends with voltage at 25°C

strengthens. Nevertheless, it seems to stabilize at a value of around 0.1 after 20 kV/mm. In the 0.04 % nanocomposite, the trend of α with electric field becomes less predictable, showing a more random behavior. Nevertheless, it is more stable than other materials, with a value that varies only between 0.3 and 0.42. For the 0.1 % nanocomposite, α stabilizes and saturates at a constant value as voltage increases after 16 kV/mm (apart from an apparent outlier at 18 kV/mm). The behavior of the numerical value of Q (from now on, reported as Q), interpreted as a generalized concept of capacitance, shows a more consistent trend across the various materials. As voltage increases, Q generally decreases up to a threshold, beyond which it saturates at an almost constant value. The electric field threshold value is around 20 kV/mm for neat sample, 16 for 0.04% nanocomposite and 14 for 0.1% nanocomposite. Moreover, two patterns can be distinguished: first of all, the value of Q for all materials seems to be quite constant (for all, at 11 kV/mm its logarithm was almost constant at -28.5).; secondly, the saturated value of Q is significantly lower for the neat material, while going to a higher value for nanocomposites which does not seem to be influenced by the content of nanofiller.

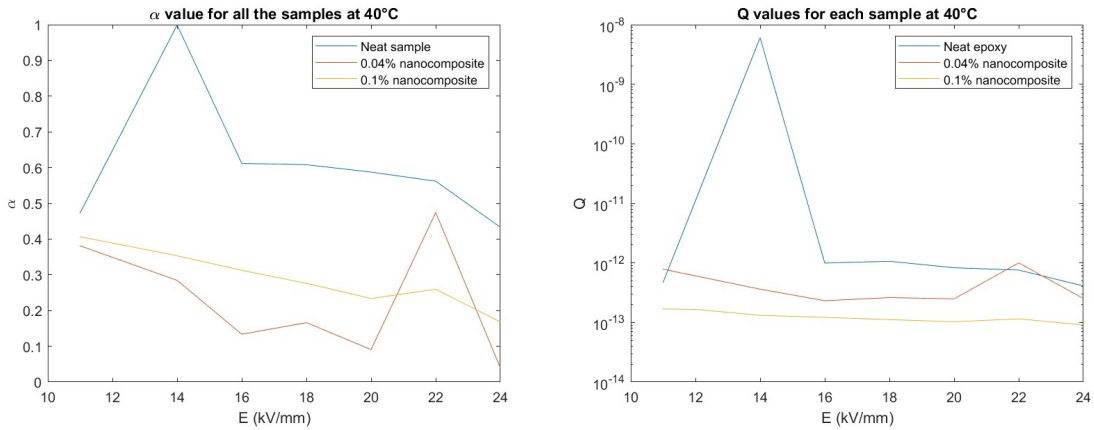

(a) α parameter

(b) Q parameter

Figure 4.48: α and Q parameters - Trends with voltage at 40°C

Additional tests were conducted at 40°C. The results shown in Fig. 4.48a-4.48b reveal a systematic

change in parameter behavior: the α value for the neat sample initially peaked at 14 kV/mm before decreasing, which corresponded to a drop in Q that subsequently stabilized around 16 kV/mm. An inversion in the order of magnitude was observed, with the neat sample achieving higher Q values at high voltage. Two notable trends emerged: Q increased with temperature across all samples, and the voltage level at which Q stabilization occurred slightly decreased—from 20 to 16 kV/mm for the neat sample, from 16 to 14 kV/mm for the 0.04% nanocomposite, while the 0.1% nanocomposite reached stabilization at 11 kV/mm. High field values of α and Q are reported in Tables 4.12 and 4.13.

Conditions	Neat sample	0.04 % NC	0.1 % NC
25°C	0.09	0.16	0.32
40°C	0.56	0.1	0.26

Table 4.12: High field α value

Conditions	Neat sample	0.04 % NC	0.1 % NC
25°C	$2 \cdot 10^{-14}$	$6.4 \cdot 10^{-14}$	$6.2 \cdot 10^{-14}$
40°C	$1 \cdot 10^{-12}$	$2.5 \cdot 10^{-13}$	$1 \cdot 10^{-13}$

Table 4.13: High field Q value

Chapter 5

Discussion

5.1 Effective incorporation of Quantum Dots

This chapter consolidates data collected from multiple tests to evaluate the incorporation efficacy of nanofillers in nanocomposite materials. By gathering results from electrical, thermal, and morphological analyses, the aim is to facilitate a comprehensive overview of the experimental evidence of occurred integration of Carbon Quantum Dots in nanocomposites.

Among these methods, Fourier Transform Infrared (FTIR) spectroscopy plays a crucial role in assessing chemical modifications associated with nanofiller incorporation [98]. In fact, FTIR analysis provides insights into the specific bonding interactions introduced by the integration of CQDs, allowing us to identify changes in the functional groups within the polymer matrix, and thus a thorough discussion on the origin of modification of spectral peaks linked to the neat sample and to the nanocomposites, also reported in table 5.1 is here exposed.

Peak	Wavenumber peak position (cm^{-1})
Hydroxyl	3600-3100
C-C stretching	3000-2800
C=O stretching	1737
C=C stretching	1667
diene with C=C	1607
O-H bending of carboxylic group	1416
amine group	1180
C-H bendings	950-700

Table 5.1: FTIR peaks and corresponding functional groups

The increase in intensity observed in the hydroxyl stretching region can be attributed to the presence of O–H bonds associated with carboxylic acid (–COOH) functional groups that arise from the functionalization of the carbon quantum dots.

The intensification of the C–C stretching vibrations in the nanocomposites could be a possible indicator of the successful incorporation of carbon quantum dots. The structural characteristics of

CQDs are predominantly defined by their sp^2 hybridization, which facilitates the formation of both single (C–C) and double (C=C) bonds between carbon atoms [99]. This hybridization is crucial for maintaining the integrity and stability of the quantum dots while contributing to their unique optical properties. The presence of peaks in the FTIR spectra around 1670 cm^{-1} and 1610 cm^{-1} is particularly significant, as these frequencies are characteristic of double bonds within carbon frameworks. The observed increase in intensity for these peaks with a higher concentration of carbon quantum dots indicates a direct correlation with the density of double bonds, underscoring the influence of CQDs on the nanocomposite's molecular architecture.

However, it is noteworthy that the increase in absorbance at 1670 cm^{-1} in the 0.1% nanocomposite raises questions that require further investigation. The precise mechanism leading to this pronounced peak enhancement remains unclear and may involve complex interactions between the quantum dots and the surrounding polymer matrix.

In addition to the C–C stretching vibrations, the peaks observed at 1737 cm^{-1} and 1416 cm^{-1} can also convey valuable information. The elevation of these peaks in the nanocomposite samples is attributed to C=O stretching and O–H bending vibrations, respectively. These vibrational modes are directly linked to the functionalization of the Carbon Quantum Dots.

Moreover, the intensity reduction of the peak at 1180 cm^{-1} with increasing nanofiller content suggests a potential suppression of secondary amine products formed during the curing process. This reduction may be a direct consequence of the higher concentration of quantum dots, which could inhibit the formation of certain cross-links within the polymer matrix.

The overall decline in absorbance observed across all peaks within the region of 950-700 cm^{-1} for the 0.1% nanocomposite raises implications regarding the physical structure of the material. As these peaks are usually linked to the C-H out-of-plane bending, this generalized drop in intensity may indicate a reduction in free space within the matrix, a phenomenon likely driven by the increased presence of nanofillers.

All these results, which highlight a significant modification of the chemical structure between the neat sample and the nanocomposite, is a strong evidence for occurred incorporation of nanofillers, but to further corroborate this structural modification, thermal analyses such as DSC and TGA are valuable in examining how these changes influence the material's thermal behavior.

In DSC, the main difference in the thermograms before glass transition temperature peak seems to be the slope of the linear temperature evolution of the heat flow. This suggests that nanocomposites, presenting a higher slope than the neat sample, are characterized by higher heat capacity. This could be explained by a strengthening of the inner structure due to the interaction between the matrix and the filler, which requires higher amount of energy to undergo the same change in thermal conditions. However, it is not clear the factor that could elucidate the 0.04% nanocomposite having a higher capacity than the other one, as suggested by the slopes.

A noteworthy aspect to consider is the graduality of the heat flow in reaching equilibrium after the T_g peak in nanocomposites only, a factor not present in neat sample DSC thermogram. This may be explained by a need for the network of epoxy polymer to reorganize its structure and/or undergo thermal relaxation mechanisms, which could arise due to the adjoint presence of nanoparticles in

the microscopic structure of the nanocomposites.

While the DSC analysis provides insights into the thermal transitions and heat capacity changes induced by nanofiller incorporation, the TGA analysis offers a different perspective on the effects of CQD addition, delving into the material's thermal stability and degradation behavior.

In particular, in the mass loss derivative spectrum obtained from TGA an additional peak emerges in the 150-250°C region in both nanocomposites, which does not appear in the neat epoxy sample. This distinct peak suggests that the incorporation of nanofillers introduces new thermal characteristics absent in the pure polymer matrix. The presence of this peak indicates a specific decomposition behavior associated with the nanofillers, which undergo thermal degradation around this temperature. This observation aligns with findings reported in the literature, particularly in [100], which highlights the influence of various nanofillers on the thermal stability of polymer composites.

The arising of the 200°C peak in the nanocomposites indicates that the interaction between the nanofillers and the epoxy matrix alters the overall thermal degradation process. This occurs as the Quantum Dots are organic nanometric entities, and thus they are subject to thermal degradation at a significantly lower temperature than the neat epoxy. It is important to remark that the 0.1% nanocomposite is characterised by a more prominent peak (higher intensity of mass loss derivative), suggesting that effectively the major percentage of nanoadditive leads to a higher mass loss in this region. Finally, the broadening of the peak in mass loss derivative and its shifting towards lower values of temperature might indicate the effect of a wider distribution of particle dimensions inside the material.

A confirmation of effective Carbon Quantum Dot incorporation in the epoxy matrix also derives from a generalized effect of increased current values found in all conduction-related measurements, namely DC conductivity and phases A and D of TSDC. This can be simply connected to the semiconductive nature of the nanofiller, which thus modifies the transport properties leading to an enhancement of the mobility of the charge carriers.

5.2 Molecular relaxations

The combination of results coming from different experimental methods conveys a complete overview of the relaxation mechanisms occurring in the analyzed samples, which will help understanding the impact of the incorporation of nanofillers on the molecular dynamics of the material.

5.2.1 Low temperature relaxations

Experimental results from TSDC analysis revealed several key insights. Notably, the neat sample and nanocomposite exhibited a similar relaxation spectrum, as indicated by the close alignment of the γ and β relaxation peaks. This observation suggests that the introduction of the nanoadditive does not significantly alter the structural dynamics of the matrix, which closely resembles that of the neat material. Supporting this finding, Dielectric Spectroscopy measurements show a peak shift toward higher frequencies at lower temperatures. Although further investigation is required, this peak, observed around -20°C in all samples, may correspond to the β relaxation process also

identified in TSDC analysis. However, it remains possible that this peak is a combination of γ and β relaxation processes, as TSDC and dielectric spectroscopy are based on different underlying principles, potentially leading to distinct spectral behaviors.

5.2.2 T_g related phenomena

Nanocomposites have been observed to exhibit a distinctly lower glass transition temperature compared to their neat counterparts. While the majority of studies have reported enhancements in T_g due to the incorporation of nanoadditives, this phenomenon of a drop in T_g has also been discussed in the existing literature [101], where it is attributed to the interaction between the polymer matrix and the nanofillers. Such a reduction in T_g can have negative implications for the thermal stability of the resultant materials. For instance, lower T_g values may compromise the operational temperature range of nanocomposite applications, particularly in environments requiring enhanced thermal resistance. Nevertheless, the overall drop in T_g due to nanocomposite formation can be more pronounced, reaching levels of around 66°C as opposed to the 20°C of the present work. Another remarkable factor is the similar nature of both the matrix (an epoxy resin in both cases) and the filler (Carbon Nanotubes in [101], Carbon Quantum Dots in this work). This commonality could help to explain the trend, which diverges from typical nanocomposite behaviour. Furthermore, it is noteworthy that the observed decrease in T_g appears to be independent of the content of the nanofiller, suggesting that it is dictated by the nature of the interaction between the matrix and the filler.

The singularity of Phase A of TSDC is mainly given by the different relaxation frequency found for the neat sample and the nanocomposite. Both exhibit extremely low values, suggesting this is the manifestation of a polarization mechanism involving an entity with extremely high inertia. As DSC reveals that 70°C is the glass transition temperature of the nanocomposite, a possible explanation in its lower relaxation frequency is that this material undergoes a profound cooperative transformation characteristic of T_g occurrance. This could involve higher portions of the material in the conduction mechanism and thus increase the inertia and lower the frequency. In the neat material instead, the same process has begun as its T_g is around 90°C, but has not fully developed, thus only partially involving the whole network.

In phase D of TSDC, a significant variation can be deduced in terms of the position of the α relaxation peak between the two. This is a negative consequence of the incorporation of Quantum Dots inside the material. In fact, α relaxation peak is associated with the glass transition behaviour, which means that the higher the temperature position of this peak, the higher the glass transition temperature. As it can be seen, the α peak temperature position of the neat sample is higher by almost 40°C than the nanocomposite. Even though this discrepancy in thermal parameters is significantly higher than the one found in DSC experiments (20°C), this is strictly connected to the findings in the DSC section, as it is the manifestation of the modification of electric properties due to change in glass transition temperature. Moreover, the similar value of activation energy found for both the neat sample and the nanocomposite further suggests that a strong modification of the epoxy network is taking place around these temperatures, as it is a common feature of the two materials, and that it is

driving the cooperative motions.

Moreover, the appearance of a modulus peak in the intermediate frequency region in almost all samples only at extremely high temperatures may be explained by a superposition of an α relaxation peak with the more intense MWS peak at lower frequencies. This hypothesis is made because α relaxation peak is usually connected to cooperative motions [102]. Another more complete explanation could be linked to the combined AC conductivity and TSDC results of the 0.1% nanocomposite. In fact, it seems that up to 70°C, the plot of the real part of conductivity continues its descent towards lower frequencies, but towards a stabilization of the conducitivity value. This might be explained by considering it a manifestation of only a partial release of free charges due to higher mobility in the polymeric chain starting at around 40°C. A similar increase was indeed detected by TSDC in Phase D current, suggesting a generalized variation in transport properties of the material at this temperature. AC conductivity tends to a plateau until reaching it at 70°C, which is not surprisingly equal to the T_g, thus suggesting that the real part of conductivity may be able to detect the gradual process of glass transition using the variation in the thermal dynamics of its spectrum bending and low frequency conductivity stabilization.

This might also partly shed light on the space charge pattern anomalous behaviour for nanocomposites at 40°C and 20 kV/mm. In fact, the lower space charge accumulation could be linked to an enhancement in transport properties due to the beginning of glass transition process, which may not be able to balance a more intense space charge injection at higher electric fields.

5.3 Interface Presence and Trap Formation in Nanocomposites

The analytical interpretation of the data coming from the performed tests may give validation to the hypothesis of effective introduction of traps in nanocomposites. This confirms the Quantum Confinement Effect exposed in Section 2.2.2, concerning the tendency of Quantum Dots to locally reduce the mobility of charge carriers, thus potentially acting as local energetic levels, can be experimentally assessed. Starting from TSDC analysis, the most significant result in Phase D is given by the ρ peak. The fact that it appears only in nanocomposites suggests that interfaces are responsible for this experimental finding, confirming MWS phenomena take place. These interfaces of course can be reconduced to the ones near the surface of conjunction between the filler nanoparticles and the surrounding matrix. This is in strong accordance with Dielectric Spectroscopy findings.In fact it is clear from Fig. 5.1 that the variation of f_{max} with 1/T is exponential, thus resembling more an Arrhenius process, than a VFT one.

While the latter is usually ascribed to glass transition temperature phenomena, and thus to α relaxation processes, the former is confirmed by literature to be the trend followed by MWS peaks both in epoxy nanocomposites [103]-[104], and in case of other matrices [105]. The distinction from other relaxation mechanisms such as γ or β is suggested by the low frequency at which it takes place even at high temperatures. This in general corroborates what was found by TSDC mesurements, e.g. the presence of an interface in the material. Moreover, literature [106] suggests that this peak is linked to space charge relaxation. Thus, these interfaces may act as localised energy levels, whose trapped charges are released during the last step of TSDC. This is also corroborated by the

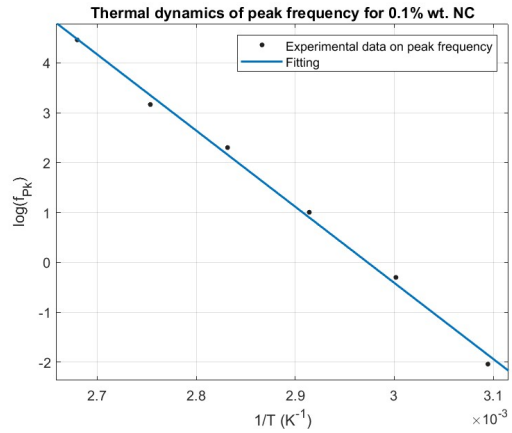

Figure 5.1: Low frequency peak evolution with temperature

depolarization phase of PEA of both nanocomposites, which underlines the presence of traps under all test conditions due to the persistence of space charge for a long period.

Tian model described in Section 3.2.1.3 was used to find the trap distribution connected to the ρ peak of the nanocomposite, reported in Fig. 5.2.

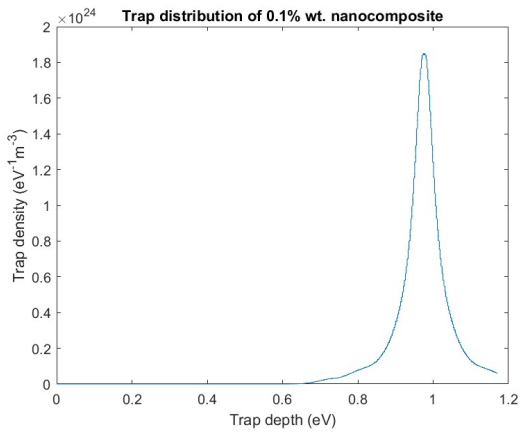

Figure 5.2: Trap distribution corresponding to ρ peak

Although trap density values obtained from TSDC (Thermally Stimulated Depolarization Current) measurements for various insulating materials are typically reported in the literature to fall within the range of 10^{20} - $10^{21} eV^{-1}m^{-3}$, which is notably lower than those determined in the present study, it is important to acknowledge that these results still lie within a broader interval of $10^{14} - 10^{26} eV^{-1}m^{-3}$, as noted in [107] for polymer typical trap density values. Furthermore, it has been reported in literature that fillers tend to act as traps, substantially increasing the trap density inside the material [108]. This effect may significantly be exacerbated by the high surface-to-volume ratio of nanofillers. This structural feature inherently might amplify the interaction intensity with the epoxy matrix, thereby potentially enhancing the formation of traps within the material.

5.4 Preliminary Evaluation of an Experimental Method to Assess Space Charge Injection Threshold

The Curie-Von Schweidler generalized model for DC conductivity analysis exposed in Section 3.2.5.1.1 has been used to evaluate the effect of electrical and thermal stress on the transient behaviour. This has been carried out outlining the trend of the two parameters, namely α and Q, with electric field and temperature in Figs. 4.47a-4.48b. A general consideration can be extracted from α parameter, which in general is always lower than 0.5, indicating a strong deviation from capacitive behaviour. In general, the incorporation of Carbon Quantum Dots seems to increase it, but no further clear trend could be distinguished. The trend of Q with the voltage, instead, could convey interesting information. As saturation occurs at high fields, this trend may be an indicator of the overcoming of space charge injection threshold. A possible explanation is that, once the applied voltage reaches a certain threshold, charge carriers are injected into the material, and further increases in voltage do not significantly affect the material's ability to store additional charge, leading to the observed saturation of Q. Another important factor to be discussed is the similarity between the Q saturated values for both nanocomposites, which suggest a similar impact of the Carbon Quantum Dots on the charge storage capability for higher voltages, independently on the content. The main effect of nanofiller content seems to be on the voltage threshold of Q saturation, which interestingly is reduced with growing content. Even though this theory is not corroborated by further literature, the space charge behaviour coming from PEA seems to support it. As a matter of fact, the neat sample at 25°C and 20 kV/mm (limiting field for Q saturation) is characterised by low space charge injection, whereas at 30 kV/mm a linear time evolution of average space charge was found. Furthermore, the two nanocomposites at 20 kV/mm and 30 kV/mm were characterised by strong space charge injection. Even though higher temperature trend of Q seems to diverge from PEA measurement finding, as the accumulated space charge is always lower at 40°C and 20 kV/mm, the possibility that this occurs due to enhanced transport phenomena in the material cannot be excluded, thus not invalidating the hypothesis of space charge injection effectively taking place. The finding that space charge injection electric field threshold decreases with temperature, as was found in experimental results for Q-saturation electric field value E_{Sat} for all the samples and reported in table 5.2, has already been widely documented in related literature.

Sample	E_{Sat} at 25°C	E_{Sat} at 40°C
Neat sample	20	16
0.04% nanocomposite	16	14
0.1% nanocomposite	14	11 (or lower)

Table 5.2: Q saturation electric field under different testing conditions

As it seems from this preliminary campaign that PEA measurements tend to confirm the trend of transient analysis parameters, this method is worth further examination in other experimental testings to assess the persistence of its validity under other operating conditions, such as higher

temperatures and electric fields or different analyzed materials. Moreover, it can be done in concomitance with steady-state DC conductivity measurements, requiring extremely lower operational times (some seconds to some tens of seconds) at the cost of a lower amount of information than PEA can provide.

5.5 Dependence of conductivity from electrical and thermal stresses

The study shows that both a and b coefficients are higher in both nanocomposites when compared to the neat epoxy sample. This indicates that the nanocomposites are more sensitive to electric field variations than the neat material. This observation correlates with the findings from PEA measurements, which demonstrated that high electric fields have a strong space charge injection effect on the dielectric properties of the nanocomposites, suggesting both conductivity and extraction mechanisms from the electrodes are facilitated as electric field increases. Furthermore, a crucial finding was that the dependence upon electric field is significantly stronger in 0.1% nanocomposite than in the other two analyzed samples. The increase of the a coefficient from 0.056 to 0.073 K^{-1} in the 0.1% nanocomposite compared to the neat sample is not negligible, but remains within a range that is still compatible with acceptable behavior. This moderate rise indicates a slight worsening in the material's temperature dependence of conductivity, which, while noteworthy, does not immediately raise concerns for typical insulating applications, as shown in Fig. 5.3. Attention should be paid to the significant increase observed in the b coefficient. As highlighted in Fig. 5.4, this value exceeds that of other commonly used insulating materials. At first glance, this may appear to be a disadvantage, as a global enhancement in conductivity can lead to higher leakage currents, posing a potential risk to the long-term performance of the insulation system. As a consequence, it is highly unlikely that these materials could be employed in a traditional electrical system, such as, e.g., cable inner insulation.

Table 3.2 Values of Parameter a That Expresses the Dependence of Resistivity upon Temperature of Various Solid Dielectrics at Selected Values of Electric Field (Stress)[a]

Sample Details		Stress (kV/mm)	Temperature Coefficient a (1/°C)
Paper	*1*	10	0.074
PPL	*1*	20	0.086
		30	0.093
Thermoset	*2*	—	0.084
	3	—	0.072
	4	5	0.101
Thermoplastic	*5*	60	0.115
	6	20	0.104
	6	30	0.114

[a]The figures in italics refer to the descriptions in the key of Table 3.1.

Figure 5.3: Typical a values - taken from [109]

Nevertheless, it is important to consider the specific requirements of field grading materials, as exposed in Section 1.3.3 particularly in applications with profoundly asymmetric electric field distributions. In such scenarios, a material whose conductivity exhibits a strong, non-linear dependence on the electric field can actually be advantageous.

For this reason, the substantial increase in the b coefficient, while potentially problematic in conventional insulating materials, may instead be an advantage for field grading purposes. The experimentally determined values of both empirical fitting parameters (a and b) strongly suggest that the 0.1% nanocomposite is a promising candidate for this type of application. Its unique combination of a moderate temperature dependence and a pronounced field dependence aligns well with the demands of field grading, making it a material worthy of further exploration.

Table 3.3 Values of Parameter *b* That Expresses the Dependence of Resistivity upon Electric Field (Stress) of Various Solid Dielectrics at Selected Temperatures[a]

		Stress Coefficient *b* (mm/kV)		
		20°C	60°C	80°C
Paper	*1*	0.028	0.018	0.029
PPL	*1*	0.0238	0.0296	0.0416
Thermoset	*2*	—	—	0.0645
Thermoplastic	*6*	0.0128	0.06	0.034

[a]The figures in italics refer to the descriptions in the key of Table 3.1.

Figure 5.4: Typical b values - taken from [109]

Chapter 6

Conclusions

This work deals with the analysis of insulating material samples. Space charge impact on insulating materials tried to be studied in the case of nanoadditivation of innovative materials called Carbon Quantum Dots. The main theoretical justification for this attempt is given by the Quantum Confinement effect, a physical phenomenon occurring due to the presence of Quantum Dots, which tend to impede the release of charge carriers from them, thus potentially acting as traps.

First of all, chemical characterization methods shed light on the effective dispersion of the nanofiller inside the nanocomposite, due to a modification of the spectrum in the FTIR spectrum and in TGA and DSC thermograms.

Following that, electrical characterization techniques employment followed the fabrication of both neat and filled samples. The main finding is given by TSDC measurements. From the analysis of these results, it can be surmised that in the nanocomposite the incorporation of Quantum Dots gives rise to space charge trapping effects due to the presence of interface between the hosting matrix and the nanofillers. This could lead to a valid viable alternative to achieve tailoring of space charge, and thus of electric field distribution. This seems to be confirmed by the PEA measurement results. Even though this results in a higher whole average space charge across the sample, the introduction of Quantum Dots leads to a persistence of the space charges in the material also in the depolarization phase, thus suggesting that trapping phenomena effectively take place. This aim was obtained by employing a relatively scarce amount of nanoadditive (up to 0.1% in weight). The negative aspects of high space charge accumulation could be overcome by correctly implementing the Quantum Dots in specific positions of the material (e.g., near one of the elctrodes to avoid space charge injection), or with a gradient of content along the material, which could both be important aspects worth of future development. The space charge behaviour of both nanocomposites seems to suggest that Carbon Quantum Dots effectively act as trapping sites, as the theoretical principle of Quantum Confinement Effect seemed to suggest. According to the space charge tailoring that must be achieved, an optimum level of trapping can be reached by tuning the content of nanofiller, which seems to create deeper traps in case of the 0.04% nanocomposite.

PEA measurements partly confirmed the TSDC findings. As a matter of fact, nanocomposites exhibited a different space charge behaviour from the neat sample, as they were characterized by higher persistance of previously stored space charge during the depolarization phase. Their

behaviour was dependent upon electrical and thermal operating conditions, with higher fields leading to more intense space charge accumulation, suggesting that inner transport and interface injection mechanisms were strongly influenced by the incorporation of nanofiller in the matrix.

A simple study of the real and imaginary permittivity suggests these materials are not suitable for HVAC applications. Nevertheless, a thorough characterization of the materials could be carried out by means of other interpretation techniques (electrical modulus, AC conductivity) for Dielectric Spectroscopy measurements, highlighting a variation in the spectra of complex permittivity likely due to the effects of nanoadditivation. The dielectric characterization of the nanocomposites reveals several important findings regarding their behavior under thermal and electrical stresses. The role of nanoadditives in modifying the activation energy for conduction and altering the relaxation dynamics of the matrix is particularly noteworthy. These findings highlight the complex ineraction between the matrix structure and the nanoadditives, which ultimately dictates the material's dielectric performance.

The DC conductivity behavior of the studied nanocomposites reveals a complex interplay between nanofiller content, electric field, and temperature. The incorporation of CQDs significantly enhances the steady-state conductivity of the material, reflecting the semiconductive nature of the fillers. The dependence of conductivity on the electric field, as characterized by the b-coefficient, highlights the role of space charge effects and the deteriorating impact of high electric fields on the material's dielectric properties. The trends in α and Q parameters offer important insights into the charge transport in the nanocomposites. The decreasing Q with increasing voltage, followed by its saturation, suggests that space charge injection is a key factor influencing the dielectric behavior of the materials. These findings underscore the significant impact of CQD content on the dielectric and capacitive properties of the nanocomposites, particularly in relation to how the materials respond to increasing electric fields. Moreover, the temperature dependence of conductivity, as described by the a-coefficient, confirms the heightened sensitivity of the nanocomposites to thermal stress. These findings are consistent with previous observations from dielectric spectroscopy, reinforcing the conclusion that the introduction of CQDs significantly modifies the material's electrical and thermal response. The concurrent decrease in a coefficient and increase in b coefficient with filler content in the nanocomposites leads to the following conclusion: the 0.1% nanocomposite is a good candidate for field grading applications, as the dependence of its conductivity upon electric field has a substantial more profound impact than its variability with temperature.

This work is not exempt from some criticalities: the glass transition temperature decrease in filled samples could act as a deteriorating factor in environments characterized by strong thermal stresses. Furthermore, the 0.1% nanocomposite, even though acting as a potential innovative material for field grading, was subject to flashover at high electrical and thermal stresses, from which it may be surmised that severely harsh operating conditions may lead to unsatisfactory performances or even to faults.

Future work may involve a more thorough investigation of space charge and conductive properties variation with filler content. In particular, α and Q parameters evolution and empirical temperature and field dependance coefficients could be found experimentally for a wider set of nanocomposites.

Moreover, it could also be possible to implement in a practical way the trap-filled nanocomposite layer between an electrode and an insulating material, to verify whether this configuration leads to a reduced local electric stress in the dielectric or not. A suggestion for future research is the investigation of the effect of Carbon Quantum Dots on materials typically positioned between the electrode and the insulating layer in cables, given the similar semiconductive properties of these materials. This could provide insight into whether their incorporation results in improved space charge distribution.

Bibliography

[1] T. Halder. Comparative study of hvdc and hvac for a bulk power transmission. In *2013 International Conference on Power, Energy and Control (ICPEC)*, pages 139–144. IEEE, 2013.

[2] Giovanni Mazzanti. *Extruded cable for high voltage direct current transmission : advances in research and development*. IEEE Press power engineering series. IEEE Press ; Wiley, Hoboken, N.J., 2013.

[3] Oluwafemi Emmanuel Oni, Kamati I. Mbangula, and Innocent E. Davidson. A review of lcc-hvdc and vsc-hvdc technologies and applications. *Transactions on environment and electrical engineering*, 1(3):68–76, 2016.

[4] Huangqing Xiao, Kaiqi Sun, Jiuping Pan, Yujun Li, and Yilu Liu. Review of hybrid HVDC systems combining line communicated converter and voltage source converter. *International Journal of Electrical Power & Energy Systems*, 129:106713, 2021.

[5] CIGRE Working Group B4.47. Technical brochure no. 553. Technical report, CIGRE, Paris, France, 2013. Study Committee B4: DC Systems and Power Electronics.

[6] CIGRE Working Group B4.68. Technical brochure no. 811. Technical report, CIGRE, Paris, France, 2020. Study Committee B4: DC Systems and Power Electronics.

[7] Alina Viişoreanu-Răchitţeanu and Alexandru Marius Viişoreanu. Surge arrester for protection against overvoltage of high voltage networks. *EMERG - Energy. Environment. Efficiency. Resources. Globalization*, 6(3):24–32, 2020.

[8] CIGRE WG B1.32. Technical brochure 496: Insulated cables. Technical report, 2012. Study Committee B1: Insulated Cables.

[9] Pierre Argaut, editor. *Accessories for HV and EHV Extruded Cables: Volume 1: Components*. CIGRE Green Books. Springer International Publishing, Cham, 2021.

[10] Pierre Argaut, editor. *Accessories for HV and EHV Extruded Cables: Volume 2: Land and Submarine AC/DC Applications*. CIGRE Green Books. Springer International Publishing, Cham, 2023.

[11] DC: BS IEC 62067. Power cables with extruded insulation and their accessories for rated voltages above 150 kV (Um = 170 kV) up to 500 kV (Um = 550 kV). Test methods and requirements, 2020.

[12] DC: BS EN IEC 60840 AMD1. Power cables with extruded insulation and their accessories for rated voltages above 30 kV (Um= 36 kV) up to 150 kV (Um = 170 kV). Test methods and requirements, 2021.

[13] Birgitta Kallstrand, Daniel Borg, Lars Walfridsson, Kenneth Johansson, Charles Doiron, Fredrik Falth, and Markus Saltzer. DC field distribution around an HVDC cable termination. In *2015 IEEE Conference on Electrical Insulation and Dielectric Phenomena (CEIDP)*, pages 35–38. IEEE, 2015.

[14] Uwe Riechert and Markus Saltzer. Dielectric Testing of Cable Connection Assembly for Gas-insulated HVDC Systems. In *2020 IEEE International Conference on High Voltage Engineering and Application (ICHVE)*, pages 1–4. IEEE, 2020.

[15] Hiroyuki Hama and Shigemitsu Okabe. Cross-sectional Study between SF_6 and Eco-friendly Gases on Dielectric Coated Electrodes for Real-size Gas Insulated Switchgear. *IEEE Transactions on Dielectrics and Electrical Insulation*, 19:253–262, 02 2012.

[16] Qian Wang, Xidong Liang, Ke Chen, Chao Wu, and Shan Liu. Surface charge properties of epoxy composites under DC voltage affected by surface and bulk conductivity. *Energies (Basel)*, 14(2):370, 2021.

[17] Nabila Zebouchi and Manu. A. Haddad. A Review on Real-Size Epoxy Cast Resin Insulators for Compact High Voltage Direct Current Gas Insulated Switchgears (GIS) and Gas Insulated Transmission Lines (GIL)—Current Achievements and Envisaged Research and Development. *Energies*, 13(23):6416, December 2020.

[18] Hermann J. Koch. Advanced technologies. In *Gas Insulated Substations*, chapter 9, pages 671–674. Wiley, 1 edition, December 2021.

[19] Zuodong Liang, Chuanjie Lin, Fangwei Liang, Weijian Zhuang, Yujia Xu, Lingling Tang, Yulin Zeng, Jun Hu, Bo Zhang, Chuanyang Li, and Jinliang He. Designing HVDC GIS/GIL spacer to suppress charge accumulation. *High Voltage*, 7, 06 2022.

[20] S. Zhang, M. M. Morcos, and K. D. Srivastava. On the management of metallic particle contamination in gas insulated switchgear. *IEEE Transactions on Dielectrics and Electrical Insulation*, 24(5):2746–2754, 2017.

[21] Shifeng Shi, Huidong Tian, Gengsheng Xie, Qingyu Wang, Tao Xie, Xi Pang, Guangzhong Yang, Peng Liu, and Zongren Peng. Insulation degradation of epoxy resin impregnated paper bushing under discharge arc ablation. *IEEE Transactions on Dielectrics and Electrical Insulation*, 31(5):2776–2784, 2024.

[22] International Electrotechnical Commission and IEEE Standards Association. IEC/IEEE 65700-19-03: Bushings for DC Applications – General Requirements and Testing, 2014. Accessed: 2024-10-25.

[23] Shiling Zhang, Zongren Peng, Peng Liu, and Naiyi Li. Design and dielectric characteristics of the ±1100 kV UHVDC wall bushing in china. *IEEE Transactions on Dielectrics and Electrical Insulation*, 22(1):409–419, February 2015.

[24] W. Lick. Experiences in testing of AC and DC bushings. In *2013 IEEE Electrical Insulation Conference (EIC)*, pages 304–307, 2013.

[25] Zhang En-Yue, Wen Zheng, Li Wei, Zhang Yi-Feng, and Chen Chong-Nan. Development and its Application of D.C. bushings of valve hall side of converter transformer. In *2014 International Conference on Power System Technology*, pages 2196–2201, 2014.

[26] Qingyu Wang, Gengsheng Xie, Huidong Tian, Zongren Peng, and Xi Yang. Impact of Temperature on the Transient DC Field Distribution of ±1100 kV UHVDC Wall Bushing. *IEEE Transactions on Power Delivery*, 36(3):1449–1457, 2021.

[27] Peter Morshuis, Andrea Cavallini, Davide Fabiani, Gian Carlo Montanari, and Carlos Azcarraga. Stress conditions in HVDC equipment and routes to in service failure. *IEEE Transactions on Dielectrics and Electrical Insulation*, 22(1):81–91, 2015.

[28] Meng Tian, B.X. Du, J. G. Su, Jin Li, L.W. Zhu, and Y. Yu. Electrical Tree in Epoxy Resin under Combined DC-harmonic Voltage. In *2018 Condition Monitoring and Diagnosis (CMD)*, pages 1–4. IEEE, 2018.

[29] A. Sendil Kumar, D. Ashwini, S. Devnath, and K. Elanseralathan. Effect of filler concentration on breakdown of isotactic polypropylene nano-composites. In *2019 IEEE 4th International Conference on Condition Assessment Techniques in Electrical Systems (CATCON)*, pages 1–4, 2019.

[30] M. Meunier, N. Quirke, and A. Aslanides. Characterisation of charge carrier traps in polymeric insulators. In *2000 Annual Report Conference on Electrical Insulation and Dielectric Phenomena (Cat. No.00CH37132)*, volume 1, pages 21–24 vol.1. IEEE, 2000.

[31] Zhihui Shao, Kai Wu, Xi Chen, and Jielin Guo. Effects of nanoparticles on trap depth in epoxy resin under different temperature. In *2016 IEEE Conference on Electrical Insulation and Dielectric Phenomena (CEIDP)*, pages 526–529. IEEE, 2016.

[32] Haruto Suzuki, Yugo Kubo, Yoitsu Sekiguchi, Masaki Kobayashi, Akiko Kumada, and Masahiro Sato. Direct measurement of charge trap depth in polymer nanocomposites. *Journal of physics. D, Applied physics*, 56(32):325301, 2023.

[33] M.J.P. Jeroense and P.H.F. Morshuis. Electric fields in HVDC paper-insulated cables. *IEEE transactions on dielectrics and electrical insulation*, 5(2):225–236, 1998.

[34] Peng Liu, Zongliang Xie, Xi Pang, Tianlei Xu, Siyu Zhang, Peter H. F. Morshuis, He Li, and Zongren Peng. Space charge behavior in epoxy-based dielectrics: Progress and perspective. *Advanced Electronic Materials*, 8(10):2200259, 2022.

[35] CIGRÉ Working Group A2.43. Transformer bushing reliability. Technical report, Paris, France, 2019. CIGRÉ Technical Brochure No. 755.

[36] A. Can-Ortiz, L. Laudebat, Z. Valdez-Nava, and S. Diaham. Nonlinear electrical conduction in polymer composites for field grading in high-voltage applications: A review. *Polymers*, 13(9):1370, 2021.

[37] Rachmawati, Hiroki Kojima, Katsumi Kato, Nabila Zebouchi, and Naoki Hayakawa. Electric Field Grading and Discharge Inception Voltage Improvement on HVDC GIS/GIL Spacer With Permittivity and Conductivity Graded Materials (ϵ/σ -FGM). *IEEE Transactions on Dielectrics and Electrical Insulation*, 29(5):1811–1817, October 2022.

[38] Yongsen Han, Feng Yang, and Chenguang Zhao. Effect of aged nonlinear resistive field grading material on electric field distribution of dc cone spacer. *Energies (Basel)*, 15(22):8361, 2022.

[39] J. Keith Nelson. Fundamentals of Dielectric Properties in Polymer Nanocomposites. In J. Keith Nelson, editor, *Dielectric Polymer Nanocomposites*, chapter 2, pages 31–64. Springer, New York, 2010. Chapter in edited volume.

[40] Yoshitsugu Kojima, Arimitsu Usuki, Masaya Kawasumi, Akane Okada, Toshio Kurauchi, and Osami Kamigaito. Synthesis of nylon 6–clay hybrid by montmorillonite intercalated with ϵ-caprolactam. *Journal of Polymer Science Part A: Polymer Chemistry*, 31(4):983–986, 1993.

[41] Amanda Dantas de Oliveira and Cesar Augusto Gonçalves Beatrice. Polymer nanocomposites with different types of nanofiller. In Subbarayan Sivasankaran, editor, *Nanocomposites*, chapter 6. IntechOpen, Rijeka, 2018.

[42] Ajay Vasudeo Rane, Krishnan Kanny, V.K. Abitha, and Sabu Thomas. Chapter 5 - methods for synthesis of nanoparticles and fabrication of nanocomposites. In Sneha Mohan Bhagyaraj, Oluwatobi Samuel Oluwafemi, Nandakumar Kalarikkal, and Sabu Thomas, editors, *Synthesis of Inorganic Nanomaterials*, Micro and Nano Technologies, pages 121–139. Woodhead Publishing, 2018.

[43] Derrick S. Dlamini, Jianxin Li, and Bhekie B. Mamba. Critical review of montmorillonite/polymer mixed-matrix filtration membranes: Possibilities and challenges. *Applied Clay Science*, 168:21–30, 2019.

[44] Danielle Veigel, Kabir Rishi, Ugochukwu Okoli, Gregory Beaucage, Jeffrey A. Galloway, Hannah Campanelli, Jan Ilavsky, Ivan Kuzmenko, and Melodie Fickenscher. Comparison of nanocomposite dispersion and distribution for several melt mixers. *Polymer*, 269(C):125735, 2023.

[45] B Demuth, Z K Nagy, A Balogh, T Vigh, G Marosi, G Verreck, I Van Assche, and M E Brewster. Downstream processing of polymer-based amorphous solid dispersions to generate tablet formulations. 486(1-2):268–286, 2015.

[46] Sumio Sakka. Sol–gel process and applications. In *Handbook of Advanced Ceramics*, chapter 11.1.2, pages 883–910. Elsevier Inc, second edition, 2013.

[47] Qi Guo, Jieyin Ma, Tianjun Yin, Haichuan Jin, Jiaxiang Zheng, and Hui Gao. Superhydrophobic non-metallic surfaces with multiscale nano/micro-structure: Fabrication and application. *Molecules (Basel, Switzerland)*, 29(9):2098, 2024.

[48] C. Zilg, D. Kaempfer, R. Thomann, R. Muelhaupt, and G.C. Montanari. Electrical properties of polymer nanocomposites based upon organophilic layered silicates. In *2003 Annual Report Conference on Electrical Insulation and Dielectric Phenomena*, pages 546–550, 2003.

[49] T. Tanaka, Y. Ohki, T. Shimizu, and S. Okabe. Superiority in partial discharge resistance of several polymer nanocomposites. December 2006. 41st International Conference on Large High Voltage Electric Systems 2006, CIGRE 2006 ; Conference date: 27-08-2006 Through 01-09-2006.

[50] Mihir Roy, J. Keith Nelson, R. K. MacCrone, and L. S. Schadler. Candidate mechanisms controlling the electrical characteristics of silica/xlpe nanodielectrics. *Journal of Materials Science*, 42(11):3789–3799, 2007.

[51] Thomas Andritsch, Roman Kochetov, Barry Lennon, Peter Morshuis, and J. Smit. Space charge behavior of magnesium oxide filled epoxy nanocomposites at different temperatures and electric field strengths. pages 136–140, 06 2011.

[52] P. O. Henk, T. W. Kortsen, and T. Kvarts. Increasing the electrical discharge endurance of acid anhydride cured DGEBA epoxy resin by dispersion of nanoparticle silica. *High performance polymers*, 11(3):281–296, 1999.

[53] Qian Xie. Enhanced dielectric properties of titanium dioxide/epoxy nanocomposites with different nanofiller shape. *Materials letters*, 367, 2024.

[54] Deesy Pinto, Luís Bernardo, Ana Amaro, and Sérgio Lopes. Mechanical properties of epoxy nanocomposites using titanium dioxide as reinforcement – a review. *Construction and building materials*, 95:506–524, 2015.

[55] Laura M. McGrath, Richard S. Parnas, Saskia H. King, John L. Schroeder, Daniel A. Fischer, and Joseph L. Lenhart. Investigation of the thermal, mechanical, and fracture properties of alumina–epoxy composites. *Polymer*, 49(4):999–1014, February 2008.

[56] Zhengdong Wang, Yonghong Cheng, Hongkang Wang, Mengmeng Yang, Yingyu Shao, Xin Chen, and Toshikatsu Tanaka. Sandwiched epoxy–alumina composites with synergistically enhanced thermal conductivity and breakdown strength. *Journal of Materials Science*, 52(8):4299–4308, April 2017.

[57] Muhammad Zeeshan Khan, Muhammad Shahzad Nazir, Muhammad Shoaib Bhutta, and Feipeng Wang. Fluorination Treatment and Nano-Alumina Concentration on the Direct Current Breakdown Performance & Trap Levels of Epoxy/Alumina Nanocomposite for a Sustainable Power System. *Sustainability*, 15(7):5826, 2023.

[58] Zhang Huiqiu, Masaru Ichinose, Hideaki Takahashi, Shingo Tamesue, Tetsu Mitsumata, Masayuki Yagi, Norio Tsubokawa, and Takeshi Yamauchi. Photoelectric properties of C60-poly(ethylene glycol) and poly(3,4-ethylenedioxythiophene) composite gel prepared via a low-temperature organic-solvent process. *Polymer Journal*, 48, 11 2015.

[59] Fei Deng, Masaei Ito, Toru Noguchi, Lifeng Wang, Hiroyuki Ueki, Ken-ichi Niihara, Yoong Ahm Kim, Morinobu Endo, and Quan-Shui Zheng. Elucidation of the reinforcing mechanism in carbon nanotube/rubber nanocomposites. *ACS Nano*, 5(5):3858–3866, 2011. PMID: 21476510.

[60] W. Wang and A. H. Jayatissa. Comparison study of graphene based conductive nanocomposites using poly(methyl methacrylate) and polypyrrole as matrix materials. *Journal of Materials Science: Materials in Electronics*, 26:7780–7783, 2015.

[61] Sedigheh Borandeh, Vahid Alimardani, Samira Sadat Abolmaali, and Jukka Seppala. Graphene family nanomaterials in ocular applications: Physicochemical properties and toxicity. *Chemical research in toxicology*, 34(6):1386–1402, 2021.

[62] Bjorn Erik Fristrup Ekbrant, Anne Ladegaard Skov, and Anders E Daugaard. Epoxy-rich systems with preference for etherification over amine-epoxy reactions for tertiary amine accelerators. *Macromolecules*, 54(9):4280–4287, 2021.

[63] Keith Linehan and Hugh Doyle. Efficient one-pot synthesis of highly monodisperse carbon quantum dots. *RSC Advances*, 4:18–21, 01 2014.

[64] Toshikatsu Tanaka. Dielectric quantum dot traps in polymer nanocomposites. In *2019 IEEE Conference on Electrical Insulation and Dielectric Phenomena (CEIDP)*, pages 340–343, 2019.

[65] He-Yu Wang, Zhong-Lei Li, Bo-Xue Du, and Key Laboratory of the Ministry of Education on Smart Power Grids, School of Electrical and Information Engineering, Tianjin University, Tianjin 300072, China. Effect of interfacial electronic structure on conductivity and space charge characteristics of core-shell quantum dots/polyethylene nanocomposite insulation. *Acta Physica Sinica*, 73(12):127702, 2024.

[66] G. Teyssedre, S. T. Li, K. Makasheva, N. Zhao, L. Milliere, and C. Laurent. Interface tailoring for charge injection control in polyethylene. *IEEE Transactions on Dielectrics and Electrical Insulation*, 24(3):1319–1330, 2017.

[67] Gopal Ramalingam, Poopathy Kathirgamanathan, Ganesan Ravi, Thangavel Elangovan, Bojarajan Arjun kumar, Nadarajah Manivannan, and Kaviyarasu Kasinathan. Quantum Confinement Effect of 2D Nanomaterials. In Faten Divsar, editor, *Quantum Dots*, chapter 2. IntechOpen, Rijeka, 2020.

[68] Istebreq A. Saeedi, Alun S. Vaughan, Thomas Andritsch, and Suvi Virtanen. The effect of curing conditions on the electrical properties of an epoxy resin. In *2016 IEEE Conference on Electrical Insulation and Dielectric Phenomena (CEIDP)*, pages 461–464. IEEE, 2016.

[69] Hosup Song, Grigori A. Medvedev, and James M. Caruthers. Effect of anisotropic deformation on the differential scanning calorimetry response of polymer glasses. *Journal of polymer science (2020)*, 62(3):508–516, 2024.

[70] Md Sumon Reza, Shafi Noor Islam, Shammya Afroze, Muhammad S. Abu Bakar, Juntakan Taweekun, and Abul K. Azad. Data on FTIR, TGA–DTG, DSC of invasive pennisetum purpureum grass. *Data in Brief*, 30:105536, 2020.

[71] Xiaomei Cai, Tingping Lei, Daoheng Sun, and Liwei Lin. A critical analysis of the α, β and γ phases in poly(vinylidene fluoride) using ftir. *RSC advances*, 7(25):15382–15389, 2017.

[72] ASTM International. Standard Test Methods for DC Resistance or Conductance of Insulating Materials. ASTM D257-14, 2014. DOI: 10.1520/D0257-14, www.astm.org.

[73] Daniele Mariani, Simone Vincenzo Suraci, Fabrizio Palmieri, and Davide Fabiani. Space charge characteristics of epoxy resin/carbon quantum dots nanocomposites. In *2024 IEEE 5th International Conference on Dielectrics (ICD)*, pages 1–4. IEEE, 2024.

[74] Jean Pierre Ibar. *Dual-Phase Depolarization Analysis: Interactive Coupling in the Amorphous State of Polymers*. De Gruyter, May 2022.

[75] Teruyoshi Mizutani, Toshimichi Tsukahara, and Masayuki Ieda. Thermally-stimulated currents in oxidized low-density polyethylene. *Japanese Journal of Applied Physics*, 19(11):2095–2098, 1980.

[76] Fuqiang Tian, Wenbin Bu, Linshuang Shi, Chun Yang, Yi Wang, and Qingquan Lei. Theory of modified thermally stimulated current and direct determination of trap level distribution. *Journal of Electrostatics*, 69(1):7–10, 2011.

[77] Daniele Mariani, Simone Vincenzo Suraci, and Davide Fabiani. Impact of additives and fillers on space charge behavior of polyethylene insulation: investigation and modeling. In *2022 IEEE 4th International Conference on Dielectrics (ICD)*, pages 62–65. IEEE, 2022.

[78] Cesare Bucci, Roberto Fieschi, and Germano Guidi. Ionic thermocurrents in dielectrics. *Phys. Rev.*, 148:816–823, Aug 1966.

[79] IEEE Recommended Practice for Space Charge Measurements on High-Voltage Direct-Current Extruded Cables for Rated Voltages up to 550 kV. ISBN: 9781504439176.

[80] T. T. N. Vu, G. Teyssedre, S. Le Roy, and C. Laurent. Space charge criteria in the assessment of insulation materials for HVDC. *IEEE Transactions on Dielectrics and Electrical Insulation*, 24(3):1405–1415, 2017.

[81] Xiue Bao, Ilja Ocket, Juncheng Bao, Jordi Doijen, Ju Zheng, Dries Kil, Zhuangzhuang Liu, Bob Puers, Dominique Schreurs, and Bart Nauwelaers. Broadband dielectric spectroscopy of cell cultures. 66(12):5750–5759, 2018.

[82] Stuart O. Nelson. Agricultural applications of dielectric spectroscopy. *Journal of Microwave Power and Electromagnetic Energy*, 39(2):75–85, 2004.

[83] Vadim F. Lvovich. *Impedance spectroscopy applications to electrochemical and dielectric phenomena*. Wiley, Hoboken, N.J., 1st ed.. edition, 2012.

[84] Laurence A. Middlemiss, Anthony J.R. Rennie, Ruth Sayers, and Anthony R. West. Characterisation of batteries by electrochemical impedance spectroscopy. *Energy Reports*, 6:232–241, 2020. 4th Annual CDT Conference in Energy Storage and Its Applications.

[85] Miran Gaberšček. Impedance spectroscopy of battery cells: Theory versus experiment. *Current Opinion in Electrochemistry*, 32:100917, 2022.

[86] Kenneth S. Cole and Robert H. Cole. Dispersion and absorption in dielectrics i. alternating current characteristics. *The Journal of chemical physics*, 9(4):341–351, 1941.

[87] D. W. Davidson and R. H. Cole. Dielectric relaxation in glycerine. *The Journal of chemical physics*, 18(10):1417–1417, 1950.

[88] S. Havriliak and S. Negami. A complex plane representation of dielectric and mechanical relaxation processes in some polymers. *Polymer*, 8:161–210, 1967.

[89] Molecular dynamics in polymer model systems. In Friedrich Kremer and Andreas Schönhals, editors, *Broadband Dielectric Spectroscopy*, Springer Book Archive. Springer-Verlag Berlin Heidelberg, Berlin, Heidelberg, 1 edition, 2003.

[90] Y.J. Wong, J. Hassan, and M. Hashim. Dielectric properties, impedance analysis and modulus behavior of catio3 ceramic prepared by solid state reaction. 571:138–144, 2013.

[91] Fuqiang Tian and Yoshimichi Ohki. Electric modulus powerful tool for analyzing dielectric behavior. *Dielectrics and Electrical Insulation, IEEE Transactions on*, 21:929–931, 06 2014.

[92] Sunny Chaudhary, Orestis Vryonis, Alun Vaughan, and Thomas Andritsch. Molecular dynamics of epoxy nanocomposites filled with core–shell and hollow nanosilica architectures. *Journal of Materials Science*, 57, 11 2022.

[93] Jacques Curie. Recherches sur le pouvoir inducteur spécifique et sur la conductibilité des corps cristallisés. *Annales de Chimie et de Physique*, 17:384–434, 1889.

[94] E. v. Schweidler. Studien über die anomalien im verhalten der dielektrika. *Annalen der Physik*, 329:711–770.

[95] E. Hernández-Balaguera and J.L. Polo. On the potential-step hold time when the transient-current response exhibits a Mittag-Leffler decay. *Journal of electroanalytical chemistry (Lausanne, Switzerland)*, 856:113631, 2020.

[96] C. D. Child. Discharge From Hot CaO. *Physical review*, 32(5):492–511, 1911.

[97] H. Nefzi and F. Sediri. Vanadium oxide nanourchins: Hydrothermal synthesis, characterization, frequency dependent electrical properties. *Ceramics international*, 41(1):1391–1399, 2015.

[98] Xingui Zhang, Sowrirajalu Bhuvana, and Leslie S. Loo. Characterization of layered silicate dispersion in polymer nanocomposites using fourier transform infrared spectroscopy. *Journal of applied polymer science*, 125(S1):E175–E180, 2012.

[99] Ajith Manayil Parambil, Shijin Rajan, Po-Chin Huang, Uday Shashikumar, Pei-Chien Tsai, Paulraj Rajamani, Yuan-Chung Lin, and Vinoth Kumar Ponnusamy. Carbon and graphene quantum dots based architectonics for efficient aqueous decontamination by adsorption chromatography technique - current state and prospects. *Environmental research*, 251(Pt 1):118541, 2024.

[100] Feng Hu, Hailin Lu, Guangshen Xu, Leifeng Lv, Lu Chen, and Zhonglei Shao. Carbon quantum dots improve the mechanical behavior of polyvinyl alcohol/polyethylene glycol hydrogel. *Journal of Applied Polymer Science*, 139(34):e52805, 2022.

[101] Ketan S. Khare and Rajesh Khare. Effect of carbon nanotube dispersion on glass transition in cross-linked epoxy–carbon nanotube nanocomposites: Role of interfacial interactions. *The Journal of Physical Chemistry B*, 117(24):7444–7454, 2013. PMID: 23691970.

[102] A. Alegria, E. Guerrica-Echevarria, L. Goitiandia, I. Telleria, and J. Colmenero. α-relaxation in the glass transition range of amorphous polymers. 1. temperature behavior across the glass transition. *Macromolecules*, 28(5):1516–1527, 1995.

[103] G. Kortaberria, P. Arruti, I. Mondragon, L. Vescovo, and M. Sangermano. Dynamics of in situ synthetized silver-epoxy nanocomposites as studied by dielectric relaxation spectroscopy. *Journal of Applied Polymer Science*, 120(4):2361–2367, 2011.

[104] H. Hammami, M. Arous, M. Lagache, and A. Kallel. Study of the interfacial MWS relaxation by dielectric spectroscopy in unidirectional PZT fibres/epoxy resin composites. *Journal of Alloys and Compounds*, 430(1):1–8, 2007.

[105] E. Nikaj, I. Stevenson-Royaud, G. Seytre, L. David, and E. Espuche. Dielectric properties of polyamide 6-montmorillonite nanocomposites. *Journal of Non-Crystalline Solids*, 356(11):589–596, 2010. Broadband Dielectric Spectroscopy and its Applications.

[106] J. van Turnhout. Thermally stimulated discharge of polymer electrets: A study on nonisothermal dielectric relaxation phenomena. 1974.

[107] Martin Pope, Charles E. Swenberg, and Martin Pope. *Electronic processes in organic crystals and polymers / Martin Pope, Charles E. Swenberg*. Monographs on the physics and chemistry of materials ; 56. Oxford University Press, New York, second edition. edition, 1999.

[108] Simone Vincenzo Suraci, Daniele Mariani, and Davide Fabiani. Impact of antioxidants on DC and AC electrical properties of XLPE-based insulation systems. *IEEE access*, 11:71232–71241, 2023.

[109] R.N. Hampton. Feature article - some of the considerations for materials operating under high voltage, direct current stresses. *IEEE Electrical Insulation Magazine*, 24(1):5–13, 2008.